

Unveiling Stimulation Secrets of Electrical Excitation of Neural Tissue Using a Circuit Probability Theory

Hao Wang^{*1,3,5}, Jiahui Wang^{1,2,3,5}, Xin Yuan Thow², Sanghoon Lee^{1,2,3,5}, Wendy Yen Xian Peh², Kian Ann Ng², Tianyiyi He^{1,3,5}, Nitish V. Thakor², Chengkuo Lee^{*1,2,3,4,5}

¹Department of Electrical and Computer Engineering, National University of Singapore, Singapore 117583

²Singapore Institute for Neurotechnology (SINAPSE), National University of Singapore, Singapore 117456

³Center For Intelligent Sensor and MEMS, National University of Singapore, Singapore 117581

⁴NUS Graduate School for Integrative Sciences and Engineering, National University of Singapore,
Singapore 117456

⁵Hybrid Integrated Flexible Electronic Systems, National University of Singapore, Singapore 117583

Abstract

A new theory, named the Circuit-Probability theory, is proposed to unveil the “secret” of electrical nerve stimulation, essentially explain the nonlinear and resonant phenomena observed when neural and non-neural tissues are electrically stimulated. For the explanation of frequency dependent response, an inductor is involved in the neural circuit model. Furthermore, predicted response to varied stimulation strength is calculated stochastically. Based on this theory, many empirical models, such as strength-duration relationship and LNP model, can be theoretically explained, derived, and amended. This theory can explain the complex nonlinear interactions in electrical stimulation and fit *in vivo* experiment data on stimulation-responses of many experiments. As such, the C-P theory should be able to guide novel experiments and more importantly, offer an in-depth physical understanding of the neural tissue. As a promising neural model, we can even further explore the more accurate circuit configuration and probability equation to better describe the electrical stimulation of neural tissues in the future.

Introduction

Neuromodulation by electrical stimulation has proven itself as an effective treatment for medical conditions in many therapeutic situations such as deep brain stimulation (e.g. Parkinson's disease) ^[1], spinal cord stimulation (e.g. chronic pain) and peripheral nerves stimulation (neuroprosthetics) ^[2-3]. However, fine details of the mechanism by which electrical stimulation modulates neural response is not well understood ^[4-5]. Hence a more complete theoretical tissue response model to varying electrical stimulation parameters is still an ongoing pursuit ^[6-7], especially to uncover precise stimulation parameters to achieve control of nerve function. The classical approach is to study stimulation of individual neurons based on the Hodgkin–Huxley model (HH model) along with simulated electric field distribution ^[8-11]. However, there is a gap in our knowledge describing the microscopic axon structure leading up to the stimulation and response in complex neural (nerve and cortex) and non-neural (muscle) tissues ^[12]. To address this issue, empirical models and rules have been developed (e.g., Linear-Nonlinear-Poisson cascade model (LNP model) ^[13], strength-duration curves ^[14-15], and stimulation waveforms efficiency difference ^[16-21]). However, some important phenomena, such as the frequency dependent response of nerve fibers ^[22-26] and the stochastically distributed gating pattern of the ion channels ^[27-30], still remain unaccounted for.

Here, we propose a new theory, named the Circuit-Probability theory (C-P theory), to offer an in-depth understanding of neural and non-neural tissue response to electrical stimulation. In this theory, an inductor is involved in the neural circuit model to explain the frequency dependent response. Furthermore, predicted response to varied stimulation strength is calculated stochastically, which is incompatible with the HH model but compatible with the observed stochastic gating pattern of the ion channels ^[30]. Meanwhile, most of the empirical models and rules can be explained, derived, and amended using our theory. This theory can explain the complex nonlinear interactions in electrical nerve stimulation, fit experiment data, guide novel experiments, and more importantly, offer an in-depth understanding of the neural tissue in a physical level.

C-P theory: A case demonstration of sinusoid current pulse stimulation

Action potentials result from rapid changes in membrane potential, caused by ion flows between the extracellular environment and the intracellular cytoplasm across a semi-permeable membrane. The ion transport is regulated by ion channels and is initiated when voltage differences across axon membrane rises to a depolarizing threshold. This initiates a cascade of further depolarization in a feed-forward loop due to the opening of voltage-gated sodium channels. To understand the depolarization and excitation of neural and non-neural tissues, we constructed a circuit model to describe the tissue response to an external applied current. Ideally, a distributed parameter circuit would be the most accurate, but it is not feasible for most of the cases because of the great difficulty in assigning precise circuit component to every fine structure in the tissue. However, a lumped parameter model, such as the simplified version shown in Figure 1(a), can still be used to approximate the neural and non-neural tissue. Figure 1(a) shows a parallel RLC circuit with three branches. The circuit parameters are explained as follows, from left to right:

I_s is the input current injected from a pair of electrodes. The electrical response within the tissue is modeled with distributed parameters to account for varying compositions of the biological environment and tissue electrode interface. In this simplified lumped parameter model, the bottom branch contains R_1 , a leakage resistor, which represents possible current pathways between two electrodes ($I_{1_Leakage}$) that do not pass through the target tissue. In the middle branch, $I_{2_Membrane}$ is the current that directly affects $C_{Membrane}$, which is the combined capacitance of all membranes in the region. R_2 is a resistor connected in series with $C_{Membrane}$. It represents a lumped resistance associated with this branch. In the top branch, L and I_{3_L} are proposed additions representing an inductor within the biological tissue and the current that leaks into it. U is the total voltage on the RLC circuit, which is the voltage on the neural tissue being stimulated. By solving this circuit, the voltage across the cell membrane, V , can be calculated. A detailed circuit analysis method is explained in the **Supplement S1.1**.

With such a circuit, an output voltage over time, ($V(t)$, the blue curve in Figure 1(b)), can be calculated with an input current I_s (red curve in Figure 1(b)). It is this inductor L that causes the oscillation of $V(t)$ with a certain damping even after the input current ceases.

With $V(t)$, the probability of generating an action potential can be calculated, as shown in Figure 1(b). The governing equation is:

$$P = 1 - e^{-\alpha \int e^{-\frac{\beta}{|V(t)-V_{Threshold}|}} dt}$$

P is the probability of a single axon generating an action potential in response to a stimulation of a fixed duration. The probability calculation (named as ‘probability calculus’ in this study) only applies when $V(t)$ is more negative than $V_{Threshold}$. $V_{Threshold}$ is an arbitrary minimum threshold for an externally applied voltage that causes the depolarization of axon membrane. Here α and β are positive parameters. This equation is derived based on three electrophysiological considerations which will be explained in the later section of probability calculus. Hence, an estimation of the number of nerve fibers that are activated during electrical stimulation is the product of probability, P , and the total number of nerve fibers. This calculated probability can be directly used to represent the effective strength of electrical stimulation.

As the neural tissue is modeled as a parallel RLC circuit, it is predicted to have a resonance frequency, which is determined by the circuit parameters. We validated this by applying a single-frequency input (sinusoid wave) to the Common Peroneal (CP) nerve. Sine wave currents were applied upon the CP nerve to activate the Tibialis Anterior (TA) muscle and the resulting force was recorded. The force measured with respect to frequency will form a curve, here named as ‘force mapping curve’ in this study. Similarly, a probability curve with respect to frequency calculated by modeling is defined as a probability mapping curve. The detailed experiment procedure and testing setup can be found in the **Supplement S2.1**.

The force mapping results (force generated by TA muscle) against the pulse width of single pulses (in Hz) of four different current amplitudes curves are shown in Figure 1(c). The same data plotted with error bar can be found in the **Supplement S3.1**.

The shapes of these four curves are quite different, showing a complicated changing trend with increasing current amplitude. For the curves of 20 μA and 40 μA , a clear resonance effect can be observed. However,

80 μA curve shows an initial decline, before increasing to a resonance frequency. The curve of 200 μA shows a monotonically decreasing trend without the resonance effect.

Despite these variations, C-P theory can still reproduce the general shapes of the curves via probability mapping (Figure 1(d). Figure 1(e) shows a more detailed probability mapping). The parameters for the circuit and probability calculus can be found in Table 1-1(d&e). It clearly shows how the force-frequency curve changes from one shape to another shape with increasing current amplitude over a variety of pulse frequencies and accurately predicts the trend, particularly the existence of local minima and maxima.

This experiment confirms the presence of a resonance frequency in the neural tissue. The probability mapping from the C-P theory also reproduces the complex changing trends of the testing results, validating the parallel RLC circuit, probability calculus, and most importantly, the existence of an inductor.

The C-P theory consists of two parts: circuit and voltage-based probability calculus. In the subsequent sections, we will first introduce and explain these two parts separately, and next their combined application to explain phenomena observed in the experimental data.

Equivalent Circuit for general tissue modeling

Earlier, we used an individual RLC circuit to model the stimulated tissue and fit the force mapping curves. Ideally the whole tissue, including the neural and non-neural part, can be modeled as a distributed parameter circuit network as shown in Figure 2(a). Electrodes interface to this network to either introduce current (stimulating, shown in red) or measure voltage (recording, shown in blue). In this circuit network, a region of tissue is lumped as a block with certain impedance, which can be modeled as either a parallel RLC circuit or a serial RLC circuit as shown in Figure 2(b).

It is not feasible to get the accurate parameters and circuit structures of every block. Hence, simplification of the distributed parameter circuit into a lumped parameter circuit is necessary. Simplification causes distortion of circuit characteristic, resulting in distortions that can only be examined by comparing the experiment results to the predicted values.

In general, each block in the circuit network can be simplified, as shown in Figure 2(b). The impedance of the targeted neural tissue block is Z_{target} , which is connected to a serial impedance, Z_{serial} , and a parallel impedance, $Z_{parallel}$ ^[31]. Because the current source is used in this study, Z_{serial} can be neglected due to Kirchhoff's circuit law, while $Z_{parallel}$ is simplified as a resistor, R_1 . As shown earlier to explain the force mapping (Figure 1), the neural tissue, Z_{target} , responds similarly as a parallel RLC circuit. Several circuit parameters are proposed in Figure 2(c-i to iii). In Figure 2(c-i), only the five necessary parameters, R_1 , R_2 , R_3 , L and C , are presented. Figure 2(c-ii) adds further details by connecting a resistor, R_4 , in series with the L and C branches, which produces a unique damping effect upon the resulting voltage curve in the probability calculus. Two additional resistors, R_5 and R_6 , can be connected in parallel with L and C to further improve the precision of the circuit model (Figure 2(c-iii)). These two resistors can tune the voltage amplitude, damping and resonance frequency of the resulting probability curves. With these considerations, we recognize that while every additional circuit component significantly increases the complexity of fitting the circuit parameters, it also adds precision to represent the complexity and variability in tissue. Currently, the most simplified circuit (Figure 2(c-i)) is sufficiently accurate in reproducing the general trend of the testing results. In the future, circuits including more components, such as Figure 2(c-ii and c-iii), can be used for a better data fitting.

The neural tissue is modeled as a circuit shown in Figure 2(a), and the resulting voltage response, which is normally considered as a stimulus artifact, can be measured from the recording electrodes. The profile of the voltage response recorded can be accounted for with the choice of the correct circuit, where it represents a fraction of the voltage delivered from the stimulator. Here we will use the most simplified parallel RLC circuit as shown in Figure 2(c-i) for modeling and use the voltage upon C to represent the voltage response of the tissue.

Experiments used positive monophasic square waveforms, negative monophasic square waveforms and positive-first biphasic square waveforms as commonly used in neural stimulations, to generate a voltage response. The voltage responses were measured in two additional kinds of tissue models, in pelvic nerve

stimulation/recording and cortical tissue stimulation/sciatic nerve recording. The detailed testing procedure, setup and current amplitude can be found in the **Supplement S2.2** and **S2.3**.

All pulse widths refer to the single phase pulse width (SPPW) in both the monophasic and biphasic waveforms. Figure 3(a)-(f) shows the stimulus artifact recorded for each type of applied square waveform. For each current waveform, graphs show multiple overlapping curves corresponding to increasing pulse width but constant amplitude (starting range: 10-20 μ s; maximum range of 500 μ s or 1100 μ s; range depends on the condition of the subject and the depth of anesthesia) to clearly show how the waveform changes (all (i) in Figure 3). Corresponding modeling results are shown in (ii) figures. All the modeling parameters can be found in Table 1-3(a-f).

As shown in Figure 3, the modeling from the circuit of Figure 2(c-i) can generally reproduce the shapes of the voltage response. However, in Figure 3(c), 3(d) and 3(e), the voltage waveforms show some mismatch with the testing results. All curves appear similar to an RC discharging curve overlapped with a parallel RLC circuit response. The voltage curve gradually drops at the position (indicated by black arrows), whereas the voltage is predicted to keep constant in the modeling. This indicates that an additional RC discharge effect should be considered to improve the precision of the circuit. Detailed data of stimulus artifact in other experiments can be found in **Supplement S3.2**. In summary, these data further validates the existence of a parallel RLC circuit response, and shows that the circuit simplification used in our C-P theory reproduces experimental results with sufficient accuracy.

Voltage based probability calculus

Here, we describe the probability section of the C-P theory.

In the electrical stimulation of a neuron, we assume that electron transition causes the opening of sodium ion channel, which then generates the action potential (AP). Electron transition is a quantum phenomenon, which is random. Hence, the generation of APs can be described with a probability distribution, which is an exponential distribution as a Quantum event:

$$f(\lambda, t) = \begin{cases} 1 - e^{-\lambda t}, & t \geq 0 \\ 0, & t < 0 \end{cases} \quad \lambda > 0$$

Here $f(\lambda, t)$ represents the probability of AP to be generated within a time duration of t . $\frac{1}{\lambda}$ is the expected time until AP is generated. Since electron transitions need to overcome the energy barrier, which is affected by the applied voltage, a higher voltage should have a higher probability, and thus shorter expected time, of generating AP. Therefore, we can consider that the expected time, $\frac{1}{\lambda}$, to be a function of voltage:

$$\frac{1}{\lambda} = g(V)$$

We have three electrophysiological considerations when modeling $g(V)$:

Consideration 1: $\frac{1}{\lambda}$ to be infinitely large when the voltage, V , is more positive than the threshold voltage, $V_{Threshold}$. In this condition, the AP cannot be generated.

Consideration 2: $\frac{1}{\lambda}$ to be inversely proportional with the amplitude of $|V - V_{Threshold}|$, when V is more negative than $V_{Threshold}$.

Consideration 3: $\frac{1}{\lambda}$ to approach a minimal level when $|V - V_{Threshold}|$ goes to infinite. So $\frac{1}{\lambda}$ should get saturated at a certain value.

With these three considerations, one possible form of $g(V)$ can be expressed as:

$$\frac{1}{\lambda} = g(V) = \frac{1}{\alpha} \times (e^{\frac{\beta}{|V - V_{Threshold}|^n}} - c)$$

The equation can be re-written as:

$$\lambda = \frac{1}{g(V)} = \alpha \times \frac{1}{e^{\frac{\beta}{|V - V_{Threshold}|^n}} - c}$$

Here, α , β , n and c are adjustment parameters, where $\alpha > 0$, $\beta > 0$, $n > 1$ and $0 \leq c \leq 1$.

To simplify the modeling, here we assume that $\mathbf{n} = \mathbf{1}$ and $\mathbf{c} = \mathbf{0}$.

Then the complete expression of λ is:

$$\lambda = \begin{cases} \alpha \times e^{-\frac{\beta}{|V-V_{Threshold}|}}, & V < V_{Threshold} \\ 0, & V \geq V_{Threshold} \end{cases}$$

Considering that voltage is a function of time, $V(t)$, then at time point t_1 , within an infinitely small duration, Δt , if $V < V_{Threshold}$, the possibility of not generating AP is:

$$P'(V(t_1), \Delta t) = 1 - f(\lambda(V(t_1)), \Delta t) = 1 - (1 - e^{-\lambda(V(t_1)) \times \Delta t}) = e^{-\lambda(V(t_1)) \times \Delta t}$$

Here $V(t_1)$ is considered as a constant value within this Δt duration.

For a duration of T , it can be divided into N parts equally when each part is Δt as shown in Figure 4 (a).

Thus, the total probability of not generating AP within the duration of T is:

$$P'(V(t), T) = \prod_{n=1}^{n=N} P'(V(t_n), \Delta t) = \prod_{n=1}^{n=N} e^{-\lambda(V(t_n)) \times \Delta t} = e^{\sum_{n=1}^{n=N} -\lambda(V(t_n)) \times \Delta t}$$

The total probability of generating AP within the duration of T is:

$$P(V(t), T) = 1 - P'(V(t), T) = 1 - e^{\sum_{n=1}^{n=N} -\lambda(V(t_n)) \times \Delta t} = 1 - e^{\sum_{n=1}^{n=N} -\alpha \times e^{-\frac{\beta}{|V(t_n)-V_{Threshold}|} \times \Delta t}}$$

Then replacing Δt with dt , the above equation can be re-written as the continuous integral function:

$$P = 1 - e^{-\alpha \int e^{-\frac{\beta}{|V(t)-V_{Threshold}|}} dt}, \quad V(t) < V_{Threshold}$$

There are three parameters in the equation, α , β and $V_{Threshold}$. Figure 4(a-c) shows how these three parameters affect the stimulation results.

As shown in Figure 4(a), the probability of stimulation with a specific voltage waveform is affected by the part below the $V_{Threshold}$, which is the red area and called voltage area (S_V). When the amplitude of $V_{Threshold}$ becomes more negative, this S_V decreases, lowering the stimulation strength.

β is the parameter that determines how fast the expected time $\frac{1}{\lambda}$ decreases to the minimum value with increasing V . As shown in Figure 4(b), a lower β value will increase the slope of the curve of $\frac{1}{\lambda}$ versus V .

One extreme example is that when this β is very small, the $\frac{1}{\lambda}$ will be a constant value, which is α^{-1} .

$$\frac{1}{\lambda} = \alpha^{-1} \times e^{\frac{\beta}{|V-V_{Threshold}|}} \approx \alpha^{-1} \times e^0 = \alpha^{-1}$$

Then the stimulation result is only affected by the duration when $V(t) < V_{Threshold}$.

$$P = 1 - e^{-\alpha \int e^{\frac{\beta}{|V(t)-V_{Threshold}|}} dt} \approx 1 - e^{-\alpha t}, \quad V(t) < V_{Threshold}$$

α is the parameter determines the minimum value of the $\frac{1}{\lambda}$ as shown in Figure 4(c). A higher α value can induce a higher probability of AP generation.

We can roughly estimate how P will change with S_V . This is important in finding the correct circuit parameters for fitting the experiment data. For most of the situations, we need to estimate how S_V changes with current pulse width based on the force mapping results.

However, since the probability calculus equation is nonlinear, a larger S_V does not necessarily generate a higher P . Especially when two voltage curves are of different shapes and amplitudes, the sizes of S_V cannot be used to accurately determine which one can achieve a higher P .

Thus, to make the relation between S_V and P clearer, we can convert the V curve to a λ curve. An illustrative case is shown in Figure 4(d) and (e). For a biphasic square wave current (red line shown in Figure 4(d)), a voltage waveform can be calculated (blue line shown in Figure 4(d)). Then, there are three

parts of S_V , where the voltage waveform is below $V_{Threshold}$. Since λ is a function of $V(t)$, the corresponding λ curve plotted with time is shown in Figure 4(e) and the area of λ curve is denoted as S_λ .

Here the probability calculus equation can be re-written as:

$$P = 1 - e^{-\alpha \int e^{-\frac{\beta}{|V(t)-V_{Threshold}|}} dt} = 1 - e^{-\int \lambda(t) dt} = 1 - e^{-S_\lambda}$$

In this simplified equation, P changes with S_λ monotonically. Every V curve can be converted to a λ curve.

By observing the change of S_λ , we can reliably estimate and explain the change of P .

Usage of the complete C-P theory to validate three predictions

In general, all experiment results serve the purpose of validating three predictions derived from the C-P theory:

- 1) Firstly, the C-P theory can model the pattern generated by force mapping curves, recorded with the same current waveform when varying the amplitude and duration.
- 2) Secondly, since the voltage waveform is directly determined by the current waveform, the C-P theory can model the force mapping curves recorded when using different current waveforms and durations, but with the same input current amplitude
- 3) Lastly, and most importantly, is the existence of resonance frequency in different neural tissues. This resonance frequency can be measured from the force mapping curves only when the current is of some specific waveforms and amplitudes.

Because the C-P theory exhibits nonlinearity, the solution can only be obtained numerically. Hence, two figures are presented to facilitate the understanding of the experimental and modeling results. A very simple case of force mapping is shown in Figure 5. This figure shows how changing the voltage waveform determines the shape of the force mapping curve, and moreover, facilitating the understanding of the other figures in supplements (S3.1, S3.3, S3.4 and S3.5). Next, Figure 6 compares probability mapping patterns

with different circuit parameters, which shows how different force mapping patterns of other experimental data in supplementary are generated. Discussion of this application is below.

A case study demonstration and an illustration of force mapping patterns using different parameters

In this section, the C-P theory is used to explain the force mapping results from Tibialis Anterior (TA) muscle stimulation. TA muscles were stimulated with positive-first biphasic waves by varying amplitudes and SPPW (single phase pulse width) using our electrode. The resultant force was recorded and compared to the modeling results of the C-P theory (Figure 5(a) to (b)). The detailed testing setup and configuration of the electrode used can be found in **Supplement S2.4**.

In Figure 5(a), the nonlinear shape of the force mapping curve changes with current amplitude (similar to Figure 1(c)). The 0.3 mA curve shows force saturation above 300 μ s SPPW. The 0.6 mA curve shows no force increase until 400 μ s. However, the 1.2 mA curve shows a pulse width dependent response between 150 μ m and 800 μ m (Region A+B). This pulse width dependent response gradually fades away with increasing current amplitude (2.4 mA, 3 mA and 4 mA curves).

From the curves in Figure 5(a), a set of parameters for both the circuit and the probability calculus were iteratively determined to generate a probability mapping (Figure 5(b)). The details of these parameters can be found in Table 1-5(b). These parameters were found by retroactively matching the resultant probability mapping of different input amplitudes to the measured force curves with different current amplitudes (0.3-4 mA). The probability mapping estimated from the C-P theory fits well with the force mapping, predicting a pulse width dependent response in Region A+B.

However, for the curves with low current (0.3 mA and 0.6 mA in Figure 5(a)), the probability mapping curves (the lowest three curves in Figure 5(b)) do not correlate well with the force mapping curve. This suggests that muscle fiber groups stimulated at low and high current amplitudes may not be the same, requiring different sets of circuit parameters for modeling. A combined probability mapping and parameter determination of these two groups of muscle fibers can also be found in **Supplement S3.3.1**. Nevertheless,

in this work we mainly focus on the force curves when the current is higher than 1.2 mA to explain how the pulse width dependent response occurs and disappears by increasing the current amplitude.

Assuming a fixed set of parameters in the C-P theory, it is estimated that distinct voltage response waveforms will be formed at a specific SPPW. In Figure 5(c), we show three voltage waveforms (V , blue solid lines) synchronized with their input current (dashed red line). Based on the circuit parameters detailed in Table 1-5(b), we estimate the voltage across the membrane capacitor ($C_{Membrane}$) to reproduce these curves. These parameters predict three distinct voltage responses (Figure 5(c(i)-(iii))) at three different pulse widths. When the pulse width is 100 μs (Figure 5(c-i)), there is only one region of V , which is lower than the threshold voltage ($V_{Threshold}$), indicated as region A. By increasing the SPPW to 500 μs , the waveform of V will change as shown in Figure 5(c-ii). Firstly, the area of region A becomes larger. Furthermore, the RLC circuit of the C-P theory predicts that a second region exceeding $V_{Threshold}$ will occur, which is indicated as region B. This region B occurs after the input current waveform ceases due to the voltage oscillations, which is a result of the inductance in the C-P theory. For the SPPW of 1200 μs , region B will disappear as shown in Figure 5(c-iii). However, within the duration of the stimulating current waveform, a new region exceeding $V_{Threshold}$ will appear, indicated as Region C. It has to be emphasized here that region A and region C are not connected in this case.

Figure 5(d) shows the corresponding modeled voltage response curves as shown in Figure 5(c), but with smaller pulse width steps to better show the distinct changing trends in the activating regions A, B and C. These three regions have their own different trends (Figure 5(d-i) to Figure 5(d-iii)). Region A increases to saturation with increasing SPPW from 100 μs to 200 μs . Region B exists only within the pulse width range of 300 μs to 700 μs , as shown in Figure 5(d-ii). Its area first increases and then decreases, in a pulse dependent manner. Thus, the corresponding probability curve also shows a pulse width dependent response from 300 μs to 700 μs . The region C only appears when the pulse width is higher than 800 μs , as shown in Figure 5(d-iii). This region will continue to increase with increasing pulse width. As explained in Figure 4(d&e), a voltage waveform can be replotted as a λ figure. So, here for a better illustration, the

corresponding λ figures are also added below the voltage figures. The changing trend of each region is shown more clearly.

With a fixed $V_{Threshold}$, not every mapping curve produces all three regions with increasing pulse width. In the force mapping data, all three regions can only be observed in the curve of 1.2 mA in Figure 5(a). The corresponding probability mapping curve (Figure 5(b)) is represented by the multi-colored curve, with blue denoting region A, green denoting region A+B and orange denoting region C. This curve represents a predicted stimulation amplitude that would have a pulse width dependent response, resulting in the three different regions shown in Figure 5(b). For the blue section, only region A contributes to the stimulation, so the probability has a monotonically increasing trend (Figure 5(d-i)). For the range from 300 μ s to 700 μ s, regions A and B contribute to the stimulation. Region A is almost constant while region B shows a pulse width dependent response trend (Figure 5(d-ii)). Hence the probability mapping curve also shows a significant pulse width dependent change, which is the green section. When the pulse width is greater than 700 μ s, region B is almost zero, but region C begins to take effect (Figure 5(d-iii)). So the probability mapping curve can further increase after 700 μ s, which is the orange section. This colored curve shows the individual effects induced by region B and region C because these two regions do not appear simultaneously. The sections of A+B and A+C are not overlapped. However, with an increasing current amplitude, the range of pulse width affected by region B and region C both broaden and partially overlap with each other. Therefore, the pulse width dependent response induced by region B will gradually fade away and the whole curve only shows a monotonically increasing trend at the high current amplitude.

It can be clearly seen in C-P theory that the major factor determining the probability mapping result is the shape of the voltage waveform. The mapping pattern shown in Figure 5(a) and (b) is just one relatively simple pattern. There is a distinctive mapping curve (1.2 mA), which helps to derive the voltage waveform and determine the modeling parameters. However, in cases with more complicated or ambiguous patterns in the results, the modeling parameters can only be determined by iteration. It is also very difficult to explain force mapping curves by analyzing the voltage waveform as the case in Figure 5. It is thus necessary to

demonstrate the variety of probability mapping curves that can be generated when modifying circuit parameters to better fit models to these cases, shown in the following comparison below and in Figure 6.

Various probability mapping pattern by biphasic square current waveform

As biphasic square wave is the most commonly used current waveform in neural tissue stimulations, it will be used in this illustration.

Firstly, we modify the circuit by changing parameters R_1 and R_3 from the lumped parameter circuit (Figure 1(c)) for comparison (Figure 6(a-c)). The probability mapping pattern tends to show a more distinctive resonance effect by increasing R_1 (Figure 6 (a-i) to 6(c-i)). Meanwhile, at the high SPPW range, the probability mapping curves tend to have an increasing trend with a higher R_3 , and keep constant with a lower R_3 (from Figure 6 (i) to (ii)).

Before explaining the details of the illustration in Figure 6, two key index parameters need to be introduced first.

The first one is the damping factor of a parallel RLC circuit:

$$\zeta \approx \frac{1}{2R_1} \sqrt{\frac{L}{C}}$$

This is an approximation form of ζ when R_2 and R_3 are negligible. The effect of ζ on the voltage upon the capacitor C is shown in Figure 6(d). When ζ is low, the voltage amplitude and oscillation are both higher, and vice versa. Meanwhile, the quality factor of the parallel RLC circuit is

$$Q \approx R_1 \sqrt{\frac{C}{L}} = \frac{1}{2\zeta}$$

This Q will determine the resonance effect in the probability mapping. When ζ is low, which means Q is high, the resonance effect will be more distinctive, and vice versa.

In these equations, L and C are mainly determined by the resonance frequency, which typically can be roughly estimated from the force mapping data. Thus, ζ can be directly tuned by changing R_1 in the model to fit the force mapping curve. However, when R_2 and R_3 cannot be neglected, both Q and ζ cannot be written as analytical formulae. But these two approximation equations still can be used to estimate the scale of R_1 .

Another index parameter is the DC voltage, V_{DC} :

$$V_{DC} = I_A \times (R_3 \parallel R_1) = I_A \times \frac{R_3 \times R_1}{R_3 + R_1}$$

I_A is the amplitude of the square wave current. Typically, $R_3 \ll R_1$, so this equation can be simplified as:

$$V_{DC} \approx I_A \times R_3$$

This is the voltage upon the capacitor when a DC current is applied. In Figure 6(f), all three voltage curves will finally approach this V_{DC} . This V_{DC} is small in Figure 6(d) because R_3 is low. Since ζ is mainly determined by R_1 , here V_{DC} is mainly determined by R_3 .

Assuming L and C are already obtained from the estimated resonance frequency observed in the force mapping results, then these two index parameters, ζ and V_{DC} , are mainly determined by R_1 and R_3 . In this comparison as shown in Figure 6 (a)-(c), only R_1 and R_3 are changed, the rest circuit parameters and probability calculus parameters are all kept constant. The detailed modeling parameters of each case can be found in Table 1-6(a-c).

The probability mapping patterns of different ζ are compared first (from Figure 6(a-i) to 6(c-i)), assuming $R_3=200 \Omega$. The resonance effect becomes more significant with the decreasing ζ . This is because a lower ζ can induce a higher Q , resulting in stronger resonance of the voltage waveform. Also, in Figure 6 (c-i), there are two resonance peaks, at the SPPW set as $SPPW_{P_1}$ and $SPPW_{P_2}$, calculated as:

$$SPPW_{P_1} \approx \frac{1}{2} \times \frac{1}{f}$$

$$SPPW_{P_2} \approx \frac{3}{2} \times \frac{1}{f}$$

f is the resonance frequency set in the modeling. In this comparison, f is set as 1600Hz, so $SPPW_{P_1} \approx 312.5 \mu\text{m}$ and $SPPW_{P_2} \approx 937.5 \mu\text{m}$ (Figure6 (c-i)). If the SPPW is long enough or f is high enough, there can be more resonance peaks. A general equation for the n th resonance peak is:

$$SPPW_{P_n} \approx \frac{2 \times n - 1}{2} \times \frac{1}{f}$$

When the force mapping curve has multiple resonance peaks, the above equation can better estimate the resonance frequency. This multiple resonance peak effect can be seen in the cortical stimulation in **Supplementary S3.5.1**. In that case, three resonance peaks can be observed, indicating a small ζ , which means a large R_1 and a higher f .

Next, R_3 is changed from 200 Ω to 2000 Ω , causing the pattern changes as seen from (i) to (ii) in Figure 6(a-c).

There are two major differences between (i) and (ii). Firstly, the resonance effect is less distinctive when R_3 is higher because of a higher ζ . In fact, ζ is affected by every resistor in the RLC circuit. It increases with any increase in the value of parallel resistors, which are R_2 and R_3 , and decreases with any increase in the value of the serial resistor, which is R_1 .

Secondly, a higher R_3 results in a higher V_{DC} (Figure 6(d) and (e)), lowering the current amplitude required to make V_{DC} exceed $V_{Threshold}$. Once V_{DC} exceeds $V_{Threshold}$, the effective voltage area can increase with SPPW, resulting in a monotonically increasing trend with SPPW in probability mapping curves. In the comparison between (i) and (ii), at high SPPW range, the curves tend to keep constant in (i) but tend to further increase in (ii).

The probability mapping curves of the same current in Figure 6(a-c) are plotted in Figure 6(f) and (g) for a more detailed comparison. In both Figure 6(f) and (g), a lower damping, which means a higher R_1 , not only

induces a more distinctive resonance effect, but also leads to a higher probability of action potential firing. For example, in sciatic nerve stimulation, where the neural probe is wrapped around the nerve, some current will flow through the outer surface of the nerve. When the nerve surface is wet due to saline solution or tissue fluid, R_1 will decrease, resulting in an immediate drop in evoked activity for the same current.

It is easy to calculate the probability mapping with a specific set of parameters. But the inverse process, deriving a specific set of parameters from the mapping curves, cannot be easily realized. In real modeling, we need to derive both the circuit and the probability calculus parameters just from the force mapping curves. For the curves shown in Figure 6(c-i), there are distinctive resonance peaks and clear curve shapes that change with low current to high current stimulation; this observation provides clues to capturing the modeling parameters. Fitting the circuit model is challenging for the cases of Figure 6(a) and (b). Furthermore, when very high or low stimulus currents are applied, the force mapping curves generated are quite similar. Only specific currents can generate curves that can provide information about the resonance frequency, damping factor and DC voltage. When such curves are missing from testing, which frequently happens in our measurement experiments, then we can only apply exhaustive method to find the correct modeling parameters.

Up to this point, both the circuit theory and probability calculus are fully explained. The C-P theory can be applied to different neural tissues, at different states, and estimate their circuit response. Each parameter involved in this C-P theory, influenced by the external environment or tissue composition, can introduce a significant but nonlinear effect upon the final stimulation results. As it is impossible to summarize all experimental results in a statistical manner, all results reported have been analyzed and fitted by modeling their case-by-case situation. In this study, we investigated responses of four types of non-neural and neural tissues using a rat model: the skeletal muscles (**Supplement S3.3**), the sciatic nerve (**Supplement S3.4**), the cortex (**Supplement S3.5**) and the pelvic nerve (**Supplement S3.6**).

Discussion

This C-P theory should be considered as a basic physical theory rather than merely a computational model. The difference between the C-P theory and previous models is illustrated in Figure 7.

There are two major directions to build the model for electrical nerve stimulation. One is based on HH model combines with the modeling of the electric field distribution (HH+field). Since H-H model is a deterministic model with no inductance involved, and it is fundamentally incompatible with C-P theory. At this stage, it is too early to say whether HH+field model is not the correct model to use for nerve stimulation modeling. However, there is a fatal defect for the modeling of the electric field distribution: it can only reveal the strength distribution at a single time instance. As explained by the C-P theory, the voltage, which is equivalent to the electric field, is a time varying parameter. And it is the shape of the voltage waveform, which is equivalent to how the electric field changes with time, determines the stimulation responses. Without considering the effect of time, phenomena to be observed in this study, such as the resonance frequency and complex force mapping curves, cannot be explained by the previous model frameworks.

Another direction previous pursued is developing empirical models based on the experiment data. For these empirical models, their target is just to build a mathematical relation between the electrical input and the stimulation output. This electric input can be either charge, current, voltage, energy or other electrical parameters. The output can be either the force, EMG or ENG. Normally empirical models can be a set of equations without the detailed description of the physical procedure of generating the nerve stimulation by the electric input.

However, with the help of the C-P theory, we aim to extract the exact physical procedure of how the nerve is stimulated by the electric signal. The basic logical chain of development as explained below:

1. The action potential is generated by the opening of the ion channel.
2. Ion channel is gated by voltage across the cell membrane.
3. To calculate the voltage generated by an electric input, we need to construct an equivalent circuit.

4. Cell membrane, excluded the ion channels, can be considered as a capacitor which is just a part of the circuit.

5. The charging and discharging of a capacitor, which is represented by the voltage waveform across the capacitor, are not instantaneous processes, thus the input current and output voltage on a capacitor will be of different waveforms. This charging and discharging processes are not only determined by the capacitor itself, but also affected by its peripheral circuits. So a correct circuit configuration is critical for the acquisition of the correct voltage waveform across the cell membrane.

6. In a sine wave test, the force mapping curve shows a distinctive parallel RLC circuit characteristic, so there should be an inductor connected in parallel with the capacitor. That is why we use a parallel RLC circuit for modeling.

7. With the voltage waveform calculated from the circuit, there should be a relationship between the voltage and numbers of action potential generated. This relation should be continuous and should be analytically described. However, an individual ion channel does not display a continuous state change in response to applied stimulus voltage. It acts like a digital bit, which only has two states: close and open. So, we need to invoke probabilistic modeling to incorporate ion channel properties.

8. Total number of the nerve fibers times the probability is the number of action potential generated, which is the stimulation output.

Each step of this logical chain is very solid and the C-P theory is just a direct reasoning result from the logical derivation. Although either the simple RLC circuit adopted in this study or the equation used for probability calculus may not be totally accurate, the basic model framework, with both circuit and probability, should be correct. The logical chain mentioned above is a simplified version. A further thought experiment is provided in **Supplement S5** for a more in-depth comprehension.

This theory also explains why the nerve electrical stimulation cannot be accurately described by any empirical models. The circuit and probability blocks shown in Figure 7 cannot be adequately represented

by a set of analytical equations, especially when the relationship between the electrical input and the voltage waveform output cannot be directly expressed by an analytical equation. In **Supplement S1**, the actual voltage waveform is calculated with a step by step method. No analytic solution is derived; only the numerical solution of the voltage waveform is obtained.

Since the C-P theory is completely different from the previous theories and models in many aspects, many questions about the theory and experimental details will arise. A detailed discussion of several questions along with major concerns is prepared in **Supplement S4**. Here a list of these questions is provided.

Supplement S4.1: How to justify the exponential distribution implemented for probability calculus? What is the correct equation of the probability calculus? How to derive the LNP model from the C-P theory?

Supplement S4.2: What is the physical entity or the biological structure of the inductor involved in the circuit?

Supplement S4.3: How is this C-P theory compatible with the previous empirical models: strength-duration curves and stimulation waveforms efficiency difference?

Supplement S4.4: How to determine the polarity of the voltage upon the capacitor since it will affect the final results?

Supplement S4.5: Why is the sinewave only applied for Common Peroneal (CP) nerve test since it is the most effective method for the measurement of the resonance frequency?

Conclusion

In this study, we propose a new theory, named the Circuit-Probability theory, to unveil the “secret” of electrical nerve stimulation, essentially explain the nonlinear and resonant phenomena observed when nerves are electrically stimulated. In this theory, an inductor is involved in the neural circuit model for the explanation of frequency dependent response. Furthermore, predicted response to varied stimulation strength is calculated stochastically. Meanwhile, many empirical models such as strength-duration

relationship and LNP model can be theoretically derived from C-P theory. This theory is shown to explain the complex nonlinear interactions in electrical nerve stimulation and fit *in vivo* experiment data on stimulation-responses of many nerve experiments. As such, the C-P theory should be able to guide novel experiments and more importantly, offer an in-depth physical understanding of the neural tissue. As a promising neural model, we can even further explore the more accurate circuit configuration and probability equation to better describe the electrical stimulation of neural tissues in the future.

Acknowledgement

We would like to thank for the experiment setup support from Han Wu, Shih Chiang Liu, Astrid, Shuhao Lu, Li Jing Ong and Dian Sheng Wong. We also would like to thank for the animal experiment support from Gammad Gil Gerald Lasam. We have our special acknowledgement to James T. Fulton for his pioneer research of neuroscience published on the Internet.

This work was supported by grants from the National Research Foundation Competitive research programme (NRF-CRP) 'Peripheral Nerve Prostheses: A Paradigm Shift in Restoring Dexterous Limb Function' (NRF-CRP10-2012-01), National Research Foundation Competitive research programme (NRF-CRP) 'Energy Harvesting Solutions for Biosensors' (R-263-000-A27-281), National Research Foundation Competitive research programme (NRF-CRP) 'Piezoelectric Photonics Using CMOS Compatible AlN Technology for Enabling The Next Generation Photonics ICs and Nanosensors' (R-263-000-C24-281), Faculty Research Committee (FRC) 'Thermoelectric Power Generator (TEG) Based Self-Powered ECG Plaster - System Integration (Part 3)' (R-263-000-B56-112) and HIFES Seed Funding 'Hybrid Integration of Flexible Power Source and Pressure Sensors' (R-263-501-012-133).

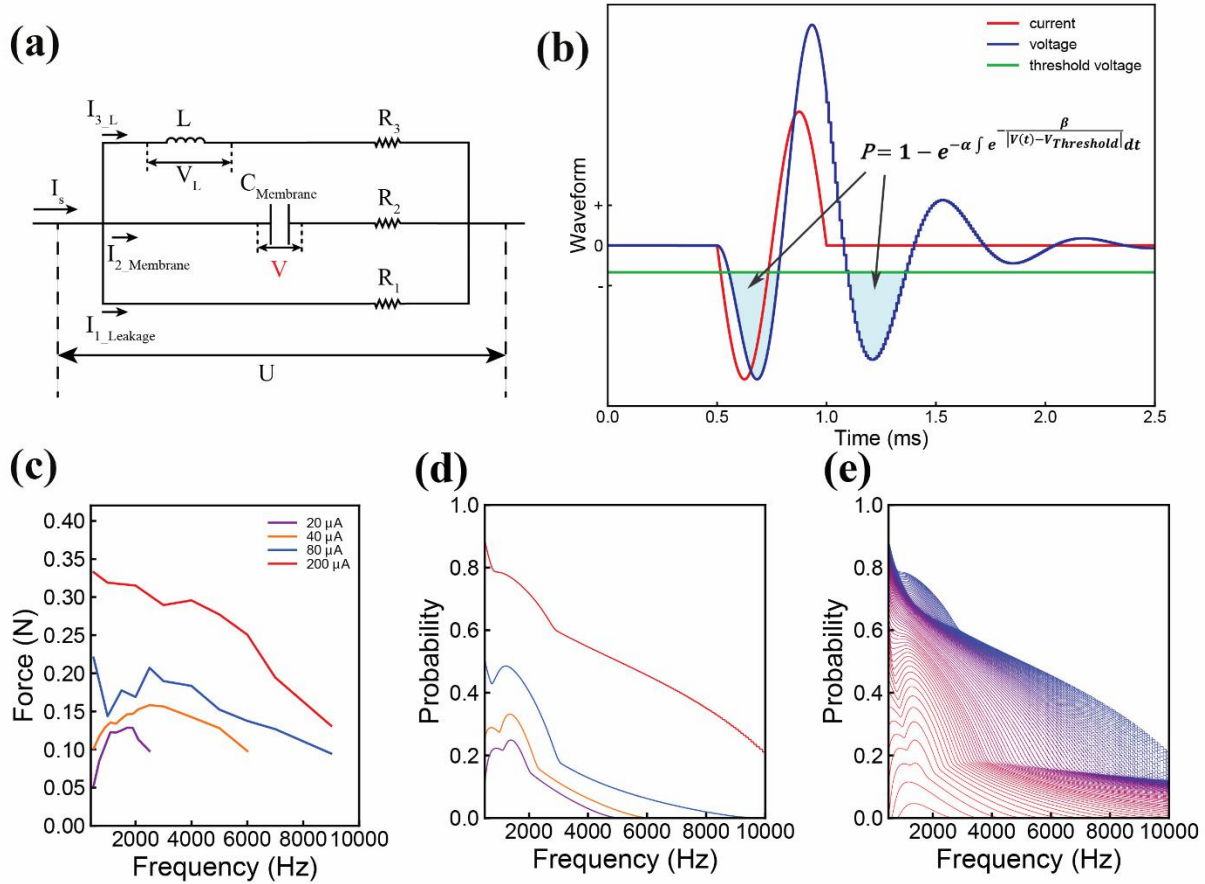


Figure 1. Illustration of the Circuit-Probability (C-P) theory with experiment and modeling results from the Common Peroneal (CP) nerve stimulation with sine-wave current. (a) The equivalent parallel RLC circuit of the neural tissue; (b) A graph of the applied current (red line) and resulting voltage (blue line) waveforms produced across the capacitor of the circuit as shown in (a); This response is derived from the probability calculus in equation: $P = 1 - e^{-\alpha \int e^{-\frac{\beta}{|V(t)-V_{Threshold}|}} dt}$; (c) the force mapping result recorded from the TA muscle by nerve stimulation. Four different current amplitudes were used at different frequencies, spanning from 500 Hz to 9000 Hz; (d) the corresponding modeling results showing the local minima and maxima predicted by the C-P theory; (e) a detailed probability mapping showing how the shape of the probability curve changes from low current, which exhibits the resonance effect, to high current, which has monotonically decreasing trend.

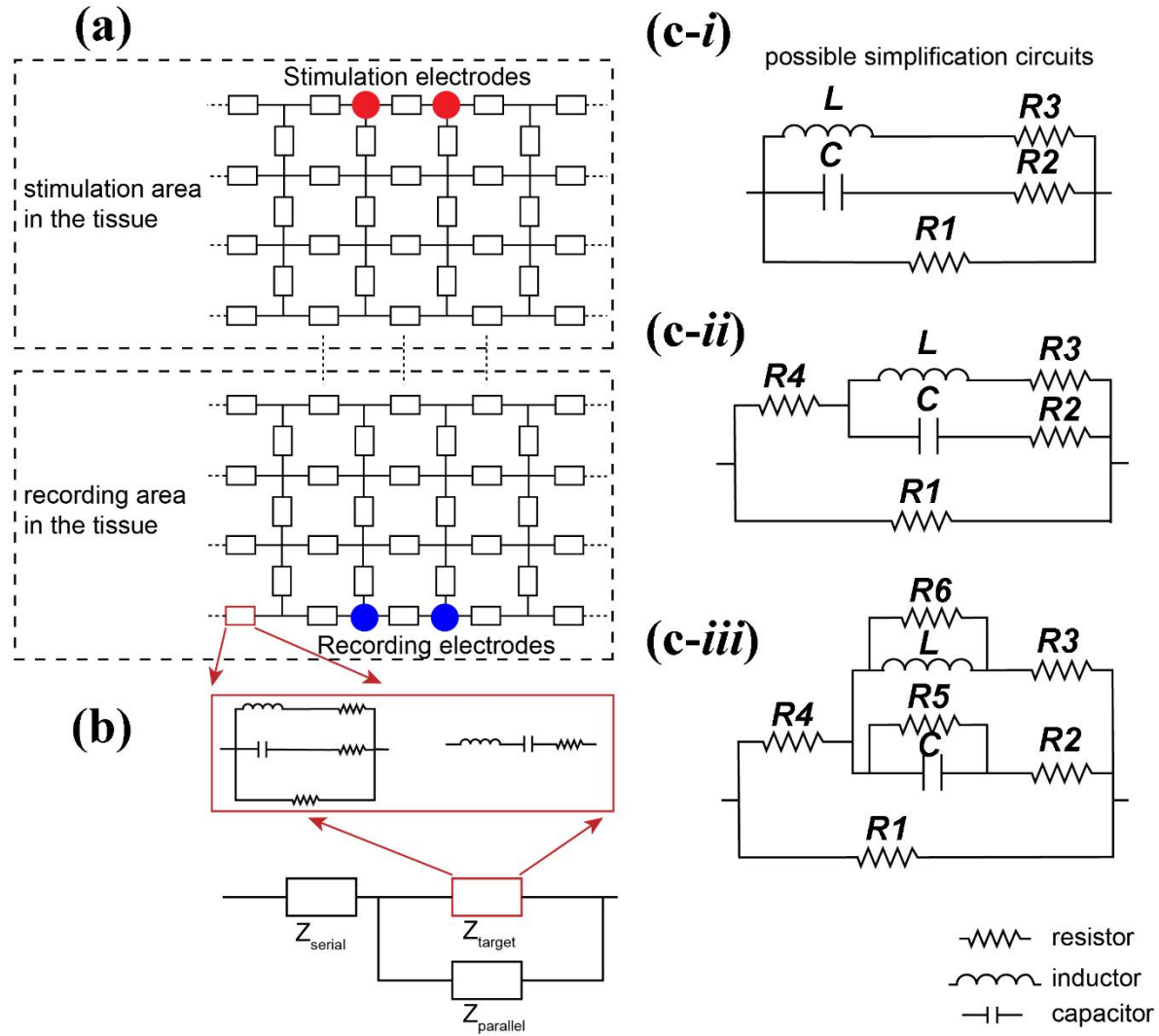


Figure 2. Circuit model of neural tissue: (a) An illustrative distributed parameter circuit to model the whole neural tissue with stimulating and recording electrode pairs which can be implanted at different locations (the two red dots represent one such stimulation pair and the blue dots represent one such recording pair), so the stimulus artifact recorded by the recording electrodes is only one part of the voltage delivered from the stimulating electrodes; (b) The external circuit, excluding the target block, can be simplified as a serial and a parallel impedance, while the impedance of the target block can be modeled as either a serial or a parallel RLC circuit; (c) Different configurations based on the basic parallel RLC circuit can be used to approximate the circuit in (b).

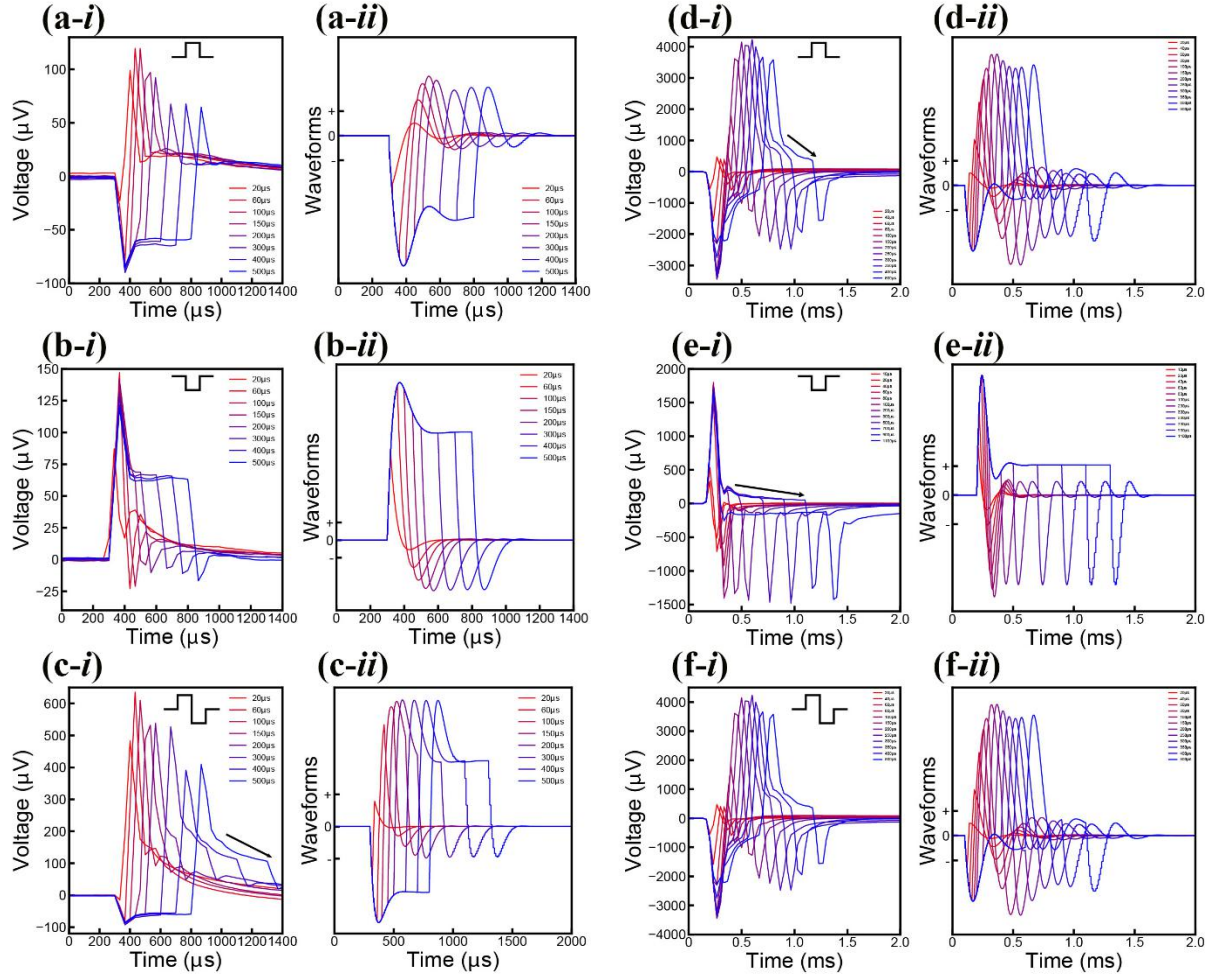


Figure 3. Experimental measurement and modeling (notation *-i* and *-ii*, respectively) of the stimulus artifact of pelvic nerve (a to c) and cortical stimulation (d to f) with different current waveforms and SPPW. (a-c) Pelvic nerve stimulation and modeling results: (a) positive monophasic square wave, (b) negative monophasic square wave and (c) positive-first biphasic square wave; (d-f) Cortical stimulation and modeling results: (d) positive monophasic square wave, (e) negative monophasic square wave and (f) positive-first biphasic square wave; (i) left figures refer to the measured data, (ii) right figures refer to the modeling results. The modeling results match well with the measurement data, validating the parallel RLC circuit used in this study.

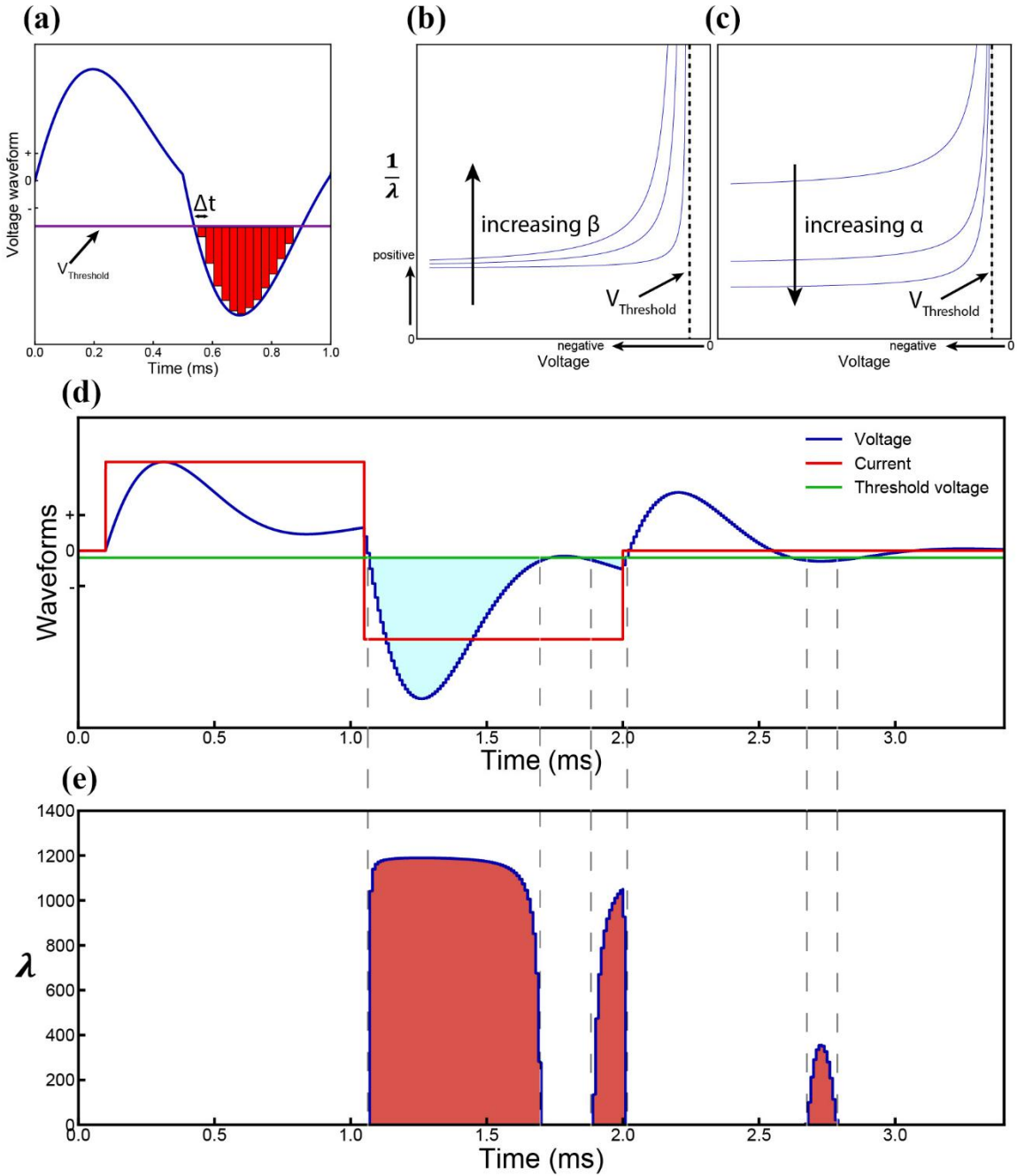


Figure 4. Parameter illustration of the probability calculus. (a) Derivation of the probability calculus with an effective voltage area; (b) The effect of β upon the expectation $\frac{1}{\lambda}$, a lower β will result in a higher slope; (c) The effect of α upon the expectation $\frac{1}{\lambda}$, a higher α will result in a lower saturation level; (d) An illustrative case with multiple effective voltage areas. Red line represents the input current (biphasic in this case), blue line represents the resultant voltage across the cell membrane, and the green line represents the

threshold voltage for action potential generation. **(e)** Corresponding λ curve converted from the voltage curve in **(d)**. The probability, \mathbf{P} , will change monotonically with the area of the λ curve, \mathbf{S}_λ .

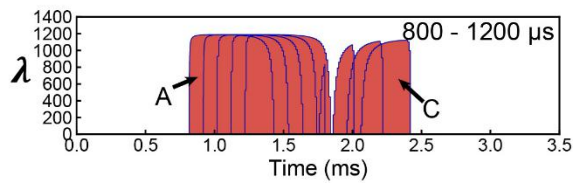
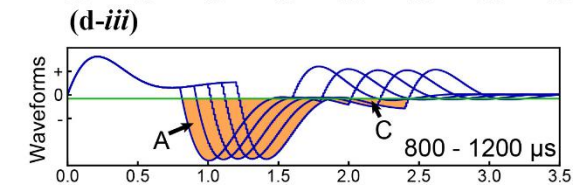
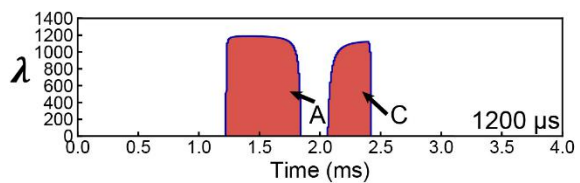
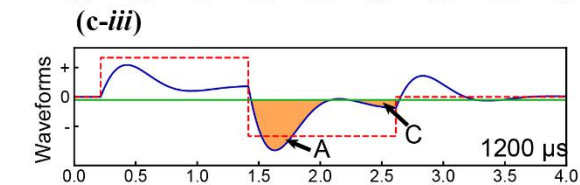
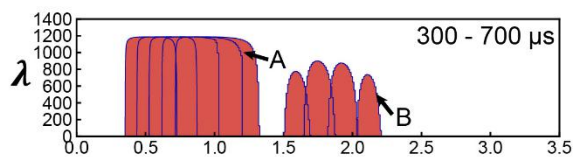
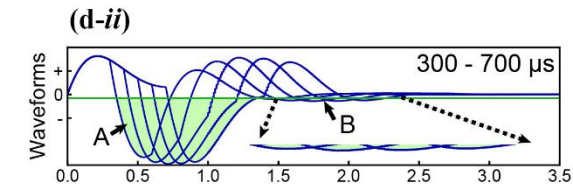
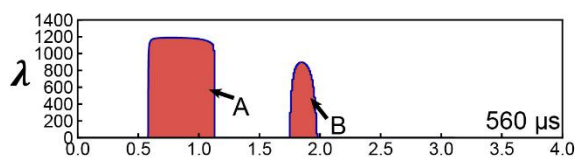
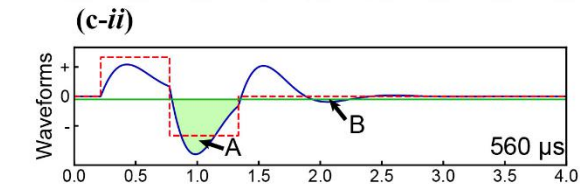
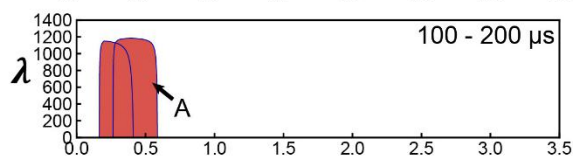
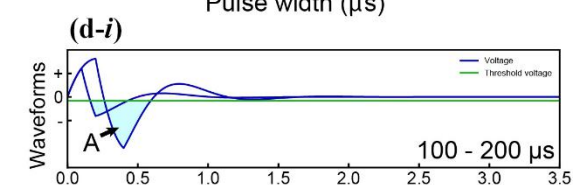
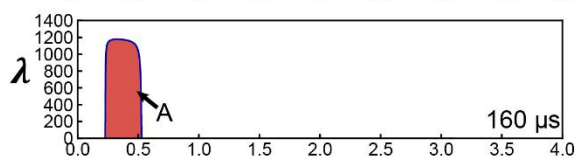
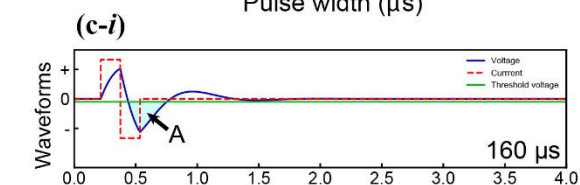
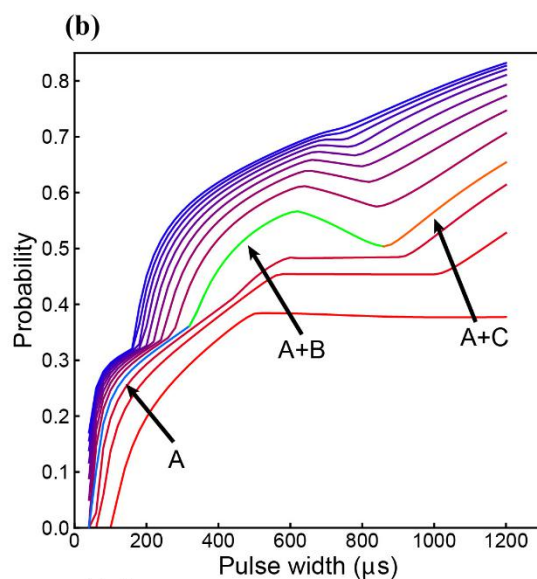
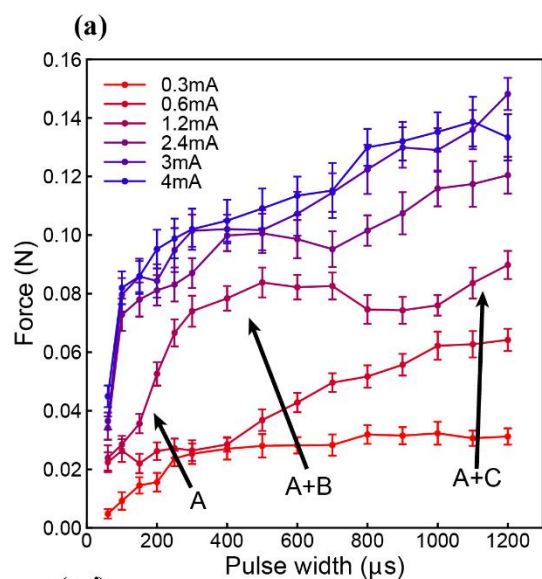


Figure 5. Measurement and modeling results of the tibialis anterior (TA) muscle stimulation by positive-first biphasic square waveform current. TA muscle contraction force was measured by attaching a rat hindlimb to a force dynamometer. (a) Measured force of the TA muscle stimulation against pulse width, with different stimulating current amplitudes (force mapping). The pulse width refers to the SPPW; **(b)** Probability calculation across pulse width when using different current amplitudes (probability mapping); the colored curve, showing distinctive frequency dependent effect, is divided into three regions: region A, region A+B and region A+C; **(c-i)** to **(c-iii)** Compares the change in the resultant voltage waveform shape and λ curve with increasing pulse duration. When a constant-current positive-first biphasic square waveform of different pulse widths was applied (red dashed line), the resultant Voltage waveform, V (blue solid line), is the tissue/circuit response to the current. Pulse duration periods result in different voltage response shapes within an RLC circuit; **(d-i)** to **(d-iii)** shows the changing trend of V and corresponding λ at different pulse width.

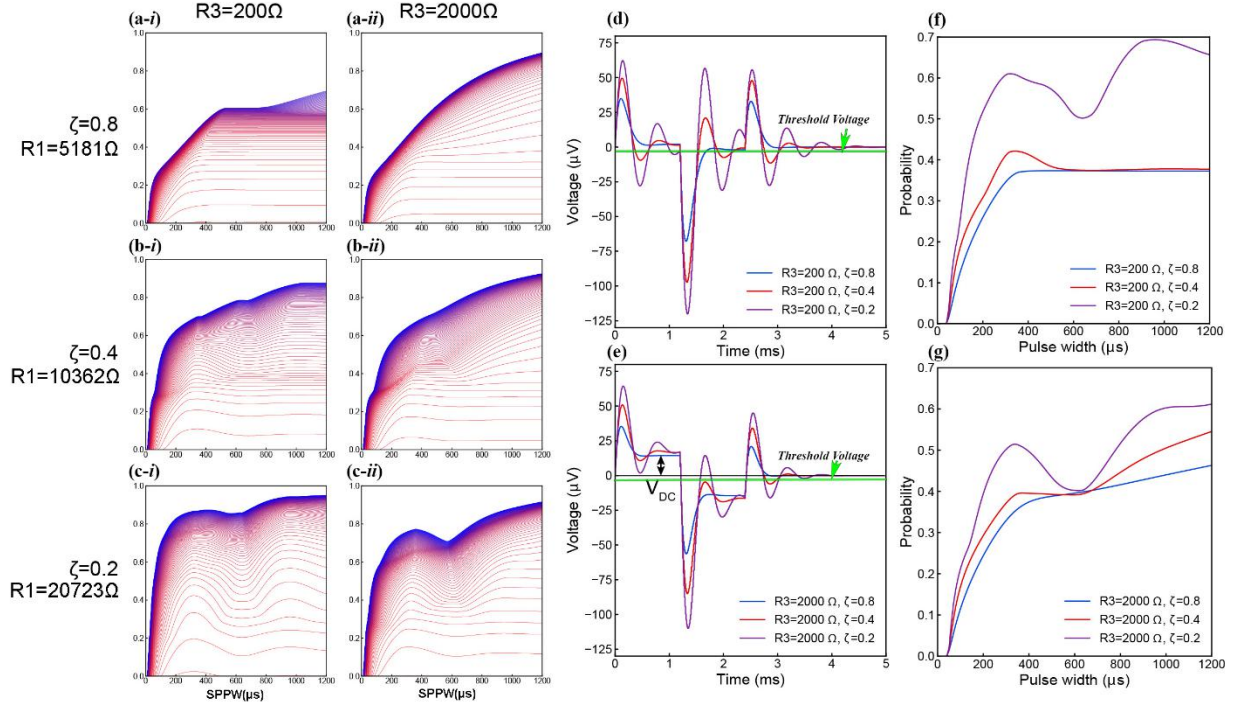


Figure 6. A general illustration of the probability mapping of positive-first biphasic square waveform current stimulation generated by different circuit parameters. (a) to (c) show the probability mapping when varying the damping factor ζ from 0.8 to 0.2, showing a stronger resonance effect with a lower ζ , with (i) the left figures modeled when $R_3 = 200 \Omega$, and (ii) the right figures modeled when $R_3 = 2000 \Omega$; (d&e) Illustrative voltage waveforms comparison of SPPW=1200 μs when the damping factor ζ from 0.8 to 0.2. (d) shows three voltage waveforms when $R_3 = 200 \Omega$; (e) shows three voltage waveforms when $R_3 = 2000 \Omega$. A lower ζ results in a higher voltage amplitude with a stronger oscillation. A higher R_3 results in a higher V_{DC} ; (f&g) Illustrative probability curves with the same current selected from (a) to (c). A lower ζ will result in a higher probability curve with stronger resonance effect. A higher R_3 will result in an increasing trend at high SPPW range.

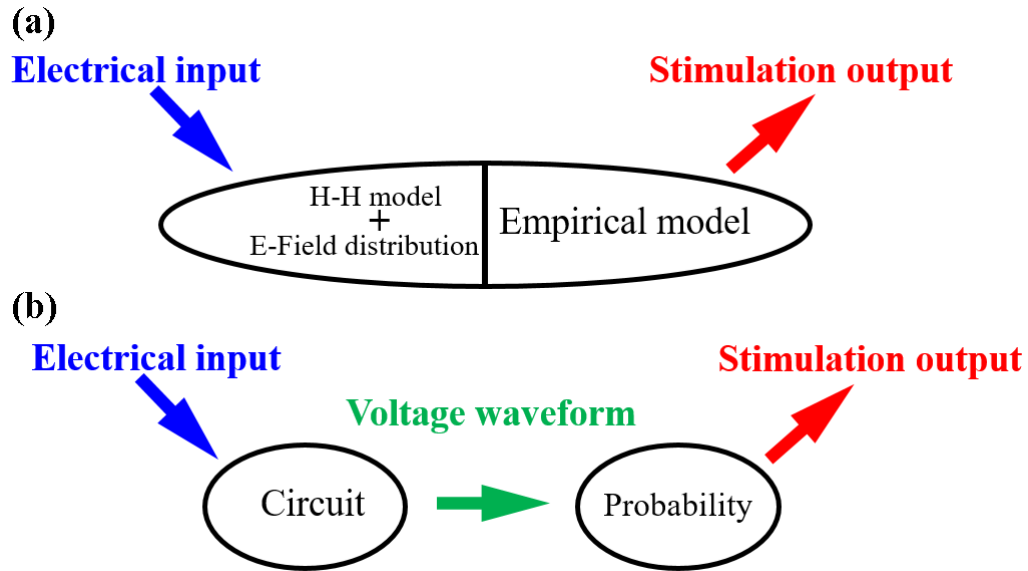


Figure 7. Conceptual difference between the C-P theory and previous models. (a) Conventional model frameworks: 1. Analytical method by combining HH model and electric field distribution; 2. Empirical model: Building simple mathematical relationship between the electrical input and stimulation output; (b) Model framework of C-P theory: Two independent blocks: circuit and probability. The electrical input will be converted to a voltage waveform across the cell membrane first. Then this voltage waveform will be used to calculate the probability of stimulating a single axon.

Table 1. Modeling parameters

No	$R_1(\Omega)$	$R_2(\Omega)$	$R_3(\Omega)$	$C(F)$	$L(H)$	α	β	$V_{Threshold}(V)$
1 (d&e)	345000	5000	10000	9n	1.9545	2000	0.1	-0.6
3(a)	80000	300	1700	18n	0.1086	NA	NA	NA
3(b)	2656	1800	800	18n	0.0813	NA	NA	NA
3(c)	2656	1800	800	18n	0.0813	NA	NA	NA
3(d)	2000	1350	500	10n	0.1464	NA	NA	NA
3(e)	3701	350	500	10n	0.1464	NA	NA	NA
3(f)	9000	1350	500	10n	0.2326	NA	NA	NA
5(b)	16579	100	3000	12n	2.1109	1200	0.01	-0.08
6(a-i)	5181	100	200	12n	0.1938	2000	0.1	-0.1
6(a-ii)	5181	100	2000	12n	0.1938	2000	0.1	-0.1
6(b-i)	10362	100	200	12n	0.1938	2000	0.1	-0.1
6(b-ii)	10362	100	2000	12n	0.1938	2000	0.1	-0.1
6(c-i)	20723	100	200	12n	0.1938	2000	0.1	-0.1
6(c-ii)	20723	100	2000	12n	0.1938	2000	0.1	-0.1
S3.3.2(b)	60286	1800	2000	4n	5.2335	600	0.8	-0.7
S3.4.1(b)	12384	1200	18000	10n	4.9687	13000	0.5	-0.35
S3.4.2(b)	5000	30	200	C1=400n; C2=5000n	0.0702	2000	0.015	-0.009
S3.5.1(b)	90000	100	600	12n	0.1629	17000	0.58	-0.22
S4.3.2.1 (b,c)	16579	100	3000	12n	2.1109	NA	NA	from -0.09 to - 0.17
S3.3.1(a)	11052	100	3000	12n	0.5277	2000	0.04	-0.048
S3.3.3.1(b)	72343	4600	14400	4n	5.2335	1500	0.06	-9.69
S3.3.3.2(b)	100	100	300	100n	0.1621	45000	0.0075	-0.006

References

- [1] Shah, V.V., Goyal, S. and Palanthandalam-Madapusi, H.J., 2017. A Possible Explanation of How High-Frequency Deep Brain Stimulation Suppresses Low-Frequency Tremors in Parkinson's Disease. *IEEE Transactions on Neural Systems and Rehabilitation Engineering*, 25(12), pp.2498-2508.
- [2] Berger, T.W., Hampson, R.E., Song, D., Goonawardena, A., Marmarelis, V.Z. and Deadwyler, S.A., 2011. A cortical neural prosthesis for restoring and enhancing memory. *Journal of Neural Engineering*, 8(4), p.046017.
- [3] Gilja, V., Nuyujukian, P., Chestek, C.A., Cunningham, J.P., Byron, M.Y., Fan, J.M., Churchland, M.M., Kaufman, M.T., Kao, J.C., Ryu, S.I. and Shenoy, K.V., 2012. A high-performance neural prosthesis enabled by control algorithm design. *Nature Neuroscience*, 15(12), p.1752.
- [4] Pelot, N. A., Behrend, C. E., & Grill, W. M. (2017). Modeling the response of small myelinated axons in a compound nerve to kilohertz frequency signals. *Journal of Neural Engineering*, 14(4), p.046022.
- [5] Howell, B., Medina, L. E., & Grill, W. M. (2015). Effects of frequency-dependent membrane capacitance on neural excitability. *Journal of Neural Engineering*, 12(5), p.056015.
- [6] Brocker, D.T. and Grill, W.M., 2013. Principles of electrical stimulation of neural tissue. In *Handbook of Clinical Neurology* (Vol. 116, pp. 3-18). Elsevier.
- [7] Fertonani, A., & Miniussi, C. (2017). Transcranial Electrical Stimulation : What we know and do not know about mechanisms. *The Neuroscientist*, 23(2), 109–123.
- [8] Hodgkin, A.L. and Huxley, A.F., 1952. A quantitative description of membrane current and its application to conduction and excitation in nerve. *Journal of Physiology*, 117(4), pp.500-544.

- [9] Capogrosso, M., Wenger, N., Raspopovic, S., Musienko, P., Beauparlant, J., Luciani, L.B., Courtine, G. and Micera, S. (2013). A computational model for epidural electrical stimulation of spinal sensorimotor circuits. *Journal of Neuroscience*, 33(49), pp.19326-19340.
- [10] Raspopovic, S., Capogrosso, M. and Micera, S. (2011). A computational model for the stimulation of rat sciatic nerve using a transverse intrafascicular multichannel electrode. *IEEE Transactions on Neural Systems and Rehabilitation Engineering*, 19(4), pp.333-344.
- [11] Pelot, N.A., Behrend, C.E. and Grill, W.M. (2017). Modeling the response of small myelinated axons in a compound nerve to kilohertz frequency signals. *Journal of neural engineering*, 14(4), p.046022.
- [12] Morse, R. P., Allingham, D., & Stocks, N. G. (2015). A phenomenological model of myelinated nerve with a dynamic threshold. *Journal of Theoretical Biology*, 382, 386–396.
- [13] Schwartz O., Pillow J. W., Rust N. C., and Simoncelli E. P. (2006). Spike-triggered neural characterization. *Journal of Vision* 6:484–507
- [14] Weiss, G. (1990). Sur la possibilite de rendre comparables entre eux les appareils servant a l'excitation electrique. *Archives Italiennes de Biologie*, 35(1), pp.413-445.
- [15] Lapicque, L., 1909. Definition experimentale de l'excitabilite. *Soc Biol.*, 77, pp.280-283.
- [16] McCreery, D.B., Agnew, W.F., Yuen, T.G.H. and Bullara, L.A. (1992). Damage in peripheral nerve from continuous electrical stimulation: comparison of two stimulus waveforms. *Medical and Biological Engineering and Computing*, 30(1), pp.109-114.
- [17] Yuen, T.G., Agnew, W.F., Bullara, L.A., Jacques, S. and McCreery, D.B. (1981). Histological evaluation of neural damage from electrical stimulation: considerations for the selection of parameters for clinical application. *Neurosurgery*, 9(3), pp.292-299.

- [18] Shannon, R.V. (1992). A model of safe levels for electrical stimulation. *IEEE Transactions on Biomedical Engineering*, 39(4), pp.424-426.
- [19] Offner, F. (1946). Stimulation with minimum power. *Journal of Neurophysiology*, 9(5), pp.387-390.
- [20] Jezernik, S. and Morari, M. (2005). Energy-optimal electrical excitation of nerve fibers. *IEEE Transactions on Biomedical Engineering*, 52(4), pp.740-743.
- [21] Wongsarnpigoon, A. and Grill, W.M. (2010). Energy-efficient waveform shapes for neural stimulation revealed with a genetic algorithm. *Journal of Neural Engineering*, 7(4), p.046009.
- [22] Howell, B., Medina, L.E. and Grill, W.M., 2015. Effects of frequency-dependent membrane capacitance on neural excitability. *Journal of neural engineering*, 12(5), p.056015.
- [23] Li, C.L. and Bak, A. (1976). Excitability characteristics of the A-and C-fibers in a peripheral nerve. *Experimental Neurology*, 50(1), pp.67-79.
- [24] Evans, E.F. (1972). The frequency response and other properties of single fibres in the guinea-pig cochlear nerve. *The Journal of Physiology*, 226(1), pp.263-287.
- [25] Kral, A., Hartmann, R., Mortazavi, D. and Klinke, R. (1998). Spatial resolution of cochlear implants: the electrical field and excitation of auditory afferents. *Hearing Research*, 121(1-2), pp.11-28.
- [26] Hartmann, R., Topp, G. and Klinke, R. (1984). Discharge patterns of cat primary auditory fibers with electrical stimulation of the cochlea. *Hearing Research*, 13(1), pp.47-62.
- [27] Aldrich, R.W. and Stevens, C.F. (1987). Voltage-dependent gating of single sodium channels from mammalian neuroblastoma cells. *Journal of Neuroscience*, 7(2), pp.418-431.
- [28] Bezanilla, F. (2000). The voltage sensor in voltage-dependent ion channels. *Physiological Reviews*, 80(2), pp.555-592.

- [29] Sanchez, J.A., Dani, J.A., Siemen, D. and Hille, B. (1986). Slow permeation of organic cations in acetylcholine receptor channels. *The Journal of General Physiology*, 87(6), pp.985-1001.
- [30] White, J.A., Rubinstein, J.T. and Kay, A.R. (2000). Channel noise in neurons. *Trends in Neurosciences*, 23(3), pp.131-137.
- [31] Mitra, S., Rutenbar, R.A., Carley, L.R. and Allstot, D.J. (1995). Substrate-aware mixed-signal macrocell placement in WRIGHT. *IEEE Journal of solid-state circuits*, 30(3), pp.269-278.

Unveiling Stimulation Secrets of Electrical Excitation of Neural Tissue Using a Circuit Probability Theory

Hao Wang^{*1,3,5}, Jiahui Wang^{1,2,3,5}, Xin Yuan Thow², Sanghoon Lee^{1,2,3,5}, Wendy Yen Xian Peh², Kian Ann Ng², Tianyi He^{1,3,5}, Nitish V. Thakor², Chengkuo Lee^{*1,2,3,4,5}

¹Department of Electrical and Computer Engineering, National University of Singapore, Singapore 117583

²Singapore Institute for Neurotechnology (SINAPSE), National University of Singapore, Singapore 117456

³Center For Intelligent Sensor and MEMS, National University of Singapore, Singapore 117581

⁴NUS Graduate School for Integrative Sciences and Engineering, National University of Singapore,
Singapore 117456

⁵Hybrid Integrated Flexible Electronic Systems, National University of Singapore, Singapore 117583

Table of Contents

S1 Circuit analysis.....	4
S1.1 Simple RLC circuit	4
S1.2 Revised RLC circuit	7
S2 Experiment preparation and testing setup	9
S2.1 Common Peroneal (CP) nerve test electrode configuration, experiment procedure and testing setup	9
S2.2 Cortical stimulation with sciatic nerve recording test electrode configuration, testing setup, detailed procedure and testing parameters	11
S2.3 Pelvic nerve test electrode configuration, testing setup, detailed procedure and testing parameters	12
S2.4 Tibialis Anterior (TA) muscle test electrode configuration, experiment procedure and testing setup	13
S3 Experiment data.....	14
S3.1 Detailed force mapping curve and voltage waveform of sinewave test on CP nerve.....	14
S3.2 Stimulus artifact data	15
S3.2.1 Stimulus artifact of cortical stimulation	15
S3.2.2 Stimulus artifact of pelvic stimulation	18
S3.3 Experiments of TA muscle stimulation.....	19
S3.3.1. Complete TA muscle modeling result with combination of two groups of muscles.....	19
S3.3.2 Four waveforms comparison of TA muscle stimulation.....	20
S3.3.3 Other experiments of four waveforms comparison of TA muscle stimulation	22
S3.4 Experiments of CP nerve stimulation	24
S3.4.1 CP nerve stimulation results by negative monophasic square wave current pulse	24
S3.4.2 Four waveforms comparison of CP nerve stimulation	25
S3.5 Experiments of cortical stimulation	27
S3.5.1 Cortical stimulation results by negative monophasic square wave current pulse	27
S3.5.2 Other force mapping data of cortical stimualtions	29
S3.5.3 Complete EMG data of cortical stimulation	30
S3.6 Experiments of pelvic nerve fibers stimulation.....	32
S3.6.1 Pelvic nerve fibers stimulation results by three different current waveforms	32
S3.6.2. Complete EMG data of pelvic stimulation	34
S4 Discussion	37
S4.1 About exponential distribution.....	37

S4.1.1 Exponential distribution for probability calculus	37
S4.1.2 Equation for probability calculus	40
S4.2 Inductor in neural tissue	42
S4.3 About the empirical models	44
S4.3.1 The stimulation efficiency of different current waveforms	44
S4.3.2 Strength–duration relationship	45
S4.4 The polarity of the voltage upon the capacitor	48
S4.5 About the sine waveform tests	49
S5 A thought experiment	50

S1 Circuit analysis

S1.1 Simple RLC circuit

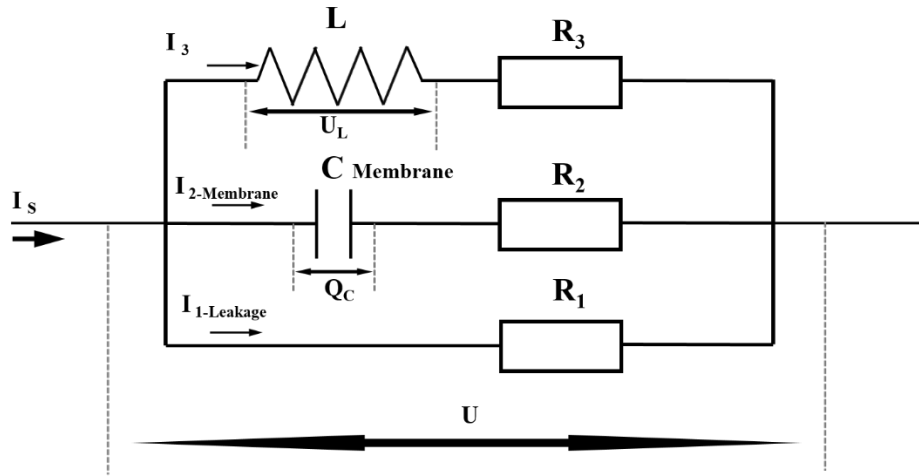


Figure S1.1. Simple parallel RLC circuit

In the equivalent parallel RLC circuit, there are 5 circuit parameters.

L : Inductance of the circuit;

C : Capacitance of the cell membrane;

R_1 : Leakage resistance of the circuit;

R_2 : Resistor connected in series with the membrane capacitor;

R_3 : Resistor connected in series with the inductor.

Here we use a set of differential equations to calculate the voltage waveform upon the membrane capacitor with the current of arbitrary waveforms.

All variables for circuit analysis are as follows:

Δt : The time interval between each step of calculation;

I_s : The input current. This current can be of arbitrary waveform;

ΔI_s : The change of I_s between each time step Δt ;

I_1 : The current through leakage resistor;

ΔI_1 : The change of I_1 between each time step Δt ;

I_2 : The current through membrane capacitor;

ΔI_2 : The change of I_2 between each time step Δt ;

I_3 : The current through inductor;

ΔI_3 : The change of I_3 between each time step Δt ;

U : The total voltage upon the whole circuit;

ΔU : The change of U between each time step Δt ;

Q_C : The charge upon the membrane capacitor;

ΔQ_C : The change of Q_C between each time step Δt ;

There are three branches of the whole circuit, all branches should share the same voltage U and can be expressed as three equations:

$$I_1 \times R_1 = U \text{ (Leakage branch voltage)}$$

$$\frac{Q_C}{C} + I_2 \times R_2 = U \text{ (Membrane capacitor branch voltage)}$$

$$L \times \frac{dI_3}{dt} + I_3 \times R_3 = U \text{ (Inductor branch voltage)}$$

The above equations can be re-written as difference equations:

$$(I_1 + \Delta I_1) \times R_1 = U + \Delta U \quad (1)$$

$$\frac{Q_C + \Delta Q_C}{C} + (I_2 + \Delta I_2) \times R_2 = U + \Delta U \quad (2)$$

$$L \times \frac{\Delta I_3}{\Delta t} + (I_3 + \Delta I_3) \times R_3 = U + \Delta U \quad (3)$$

The boundary condition is:

$$\Delta I_1 + \Delta I_2 + \Delta I_3 = \Delta I_s \quad (4)$$

The expression of ΔQ_C is:

$$\Delta Q_C = I_2 \Delta t + \frac{\Delta I_2 \Delta t}{2} \quad (5)$$

Based on the equation from (1) to (5), the ΔU can be solved as:

$$\Delta U = \frac{\Delta I_s + I_1 - \frac{U}{R_1} - \frac{1}{R_2 + \frac{\Delta t}{2C}} \times \left(U - \frac{Q_C}{C} - \frac{I_2 \times \Delta t}{C} - I_2 \times R_2 \right) - \frac{1}{\frac{L}{\Delta t} + R_3} \times (U - I_3 \times R_3)}{\frac{1}{R_1} + \frac{1}{R_2 + \frac{\Delta t}{2C}} + \frac{1}{\frac{L}{\Delta t} + R_3}} \quad (6)$$

In this equation, I_1 , I_2 , I_3 , Q_C and U are known variables of the current state. Δt is the time step we set. ΔI_s is the input to calculate the change of U , which is ΔU .

Then all other differential variables can be solved as:

$$\Delta I_1 = \frac{U + \Delta U}{R_1} - I_1$$

$$\Delta I_2 = \frac{U + \Delta U - \frac{Q_C}{C} - \frac{I_2 \times \Delta t}{C} - I_2 \times R_2}{R_2 + \frac{\Delta t}{2C}}$$

$$\Delta I_3 = \frac{U + \Delta U - I_3 \times R_3}{\frac{L}{\Delta t} + R_3}$$

$$\Delta Q_C = I_2 \Delta t + \frac{\Delta I_2 \Delta t}{2}$$

Now based on the previous state, which is represented by I_1, I_2, I_3, Q_C and U , we can calculate the next state, which is presented as:

$$I'_1 = I_1 + \Delta I_1$$

$$I'_2 = I_2 + \Delta I_2$$

$$I'_3 = I_3 + \Delta I_3$$

$$U' = U + \Delta U$$

$$Q'_C = Q_C + \Delta Q_C$$

Put the new state, I'_1, I'_2, I'_3, Q'_C and U' and the input ΔI_s into the equation (6) to calculate the next state. Repeat this procedure to calculate the waveform of each variable by the input of I_s with a time step of Δt , as shown in Figure S1.2.

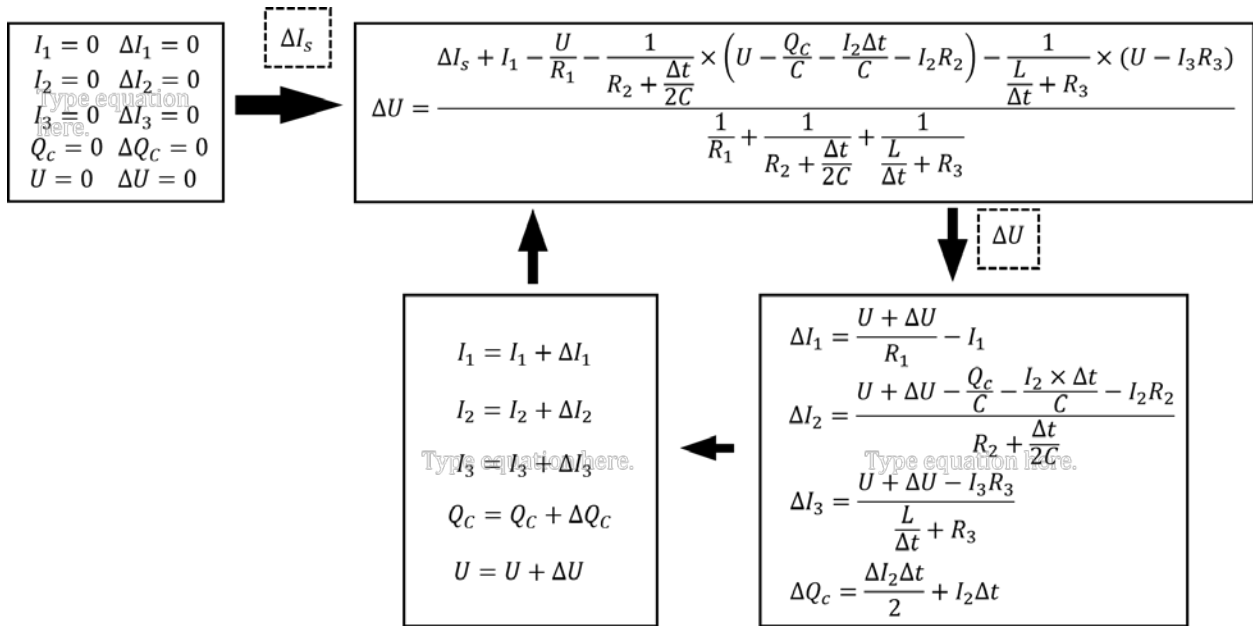


Figure S1.2. Calculation process for circuit analysis

Among all these variables, Q_C , which is the charge upon the membrane capacitor, is our target variable. With the waveform of Q_C , the voltage upon the membrane capacitor can be obtained by $V_C = \frac{Q_C}{C}$, here V_C is the voltage of the membrane capacitor.

S1.2 Revised RLC circuit

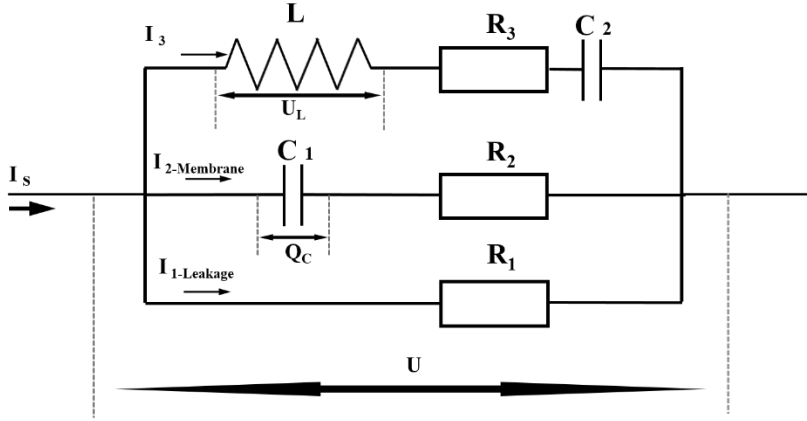


Figure S1.3. Revised RLC circuit with additional capacitor

To fit the force mapping curve in Figure S3.4.2, a revised parallel circuit is proposed. An additional capacitor is connected in series with the inductor branch, denoted as C_2 , then the C_{membrane} is denoted as C_1 . The same method can be applied to solve this circuit. Here we just give all the revised differential equations as follows:

$$L \times \frac{\Delta I_3}{\Delta t} + (I_3 + \Delta I_3) \times R_3 + \frac{Q_{C_2} + \Delta Q_{C_2}}{C_2} = U + \Delta U \text{ (Inductor branch voltage)}$$

$$\frac{Q_{C_1} + \Delta Q_{C_1}}{C_1} + (I_2 + \Delta I_2) \times R_2 = U + \Delta U \text{ (Membrane capacitor branch voltage)}$$

$$(I_1 + \Delta I_1) \times R_1 = U + \Delta U \text{ (Leakage branch voltage)}$$

$$\Delta I_1 + \Delta I_2 + \Delta I_3 = \Delta I_s \text{ (Boundary condition)}$$

Then ΔU can be solved as:

$$\Delta U = \frac{\Delta I_s + I_1 - \frac{U}{R_1} - \frac{U - \frac{Q_{C_1}}{C_1} - \frac{I_2 \Delta t}{C_1} - I_2 R_2}{R_2 + \frac{\Delta t}{2C_1}} - \frac{U - I_3 R_3 - \frac{Q_{C_2}}{C_2} - \frac{I_3 \Delta t}{C_2}}{R_3 + \frac{\Delta t}{2C_2} + \frac{L}{\Delta t}}}{\frac{1}{R_1} + \frac{1}{R_2 + \frac{\Delta t}{2C_1}} + \frac{1}{\frac{L}{\Delta t} + R_3 + \frac{\Delta t}{2C_2}}}$$

Then all other differential variables can be solved as:

$$\Delta I_3 = \frac{U + \Delta U - I_3 R_3 - \frac{Q_{C_2}}{C_2} - \frac{I_3 \Delta t}{C_2}}{\frac{L}{\Delta t} + R_3 + \frac{\Delta t}{2C_2}}$$

$$\Delta I_2 = \frac{U + \Delta U - I_2 R_2 - \frac{Q_{C_1}}{C_1} - \frac{I_2 \Delta t}{C_1}}{R_2 + \frac{\Delta t}{2C_1}}$$

$$\Delta I_1 = \frac{U + \Delta U}{R_1} - I_1$$

$$\Delta Q_{C_1} = I_2 \Delta t + \frac{\Delta I_2 \Delta t}{2}$$

$$\Delta Q_{C_2} = I_3 \Delta t + \frac{\Delta I_3 \Delta t}{2}$$

S2 Experiment preparation and testing setup

S2.1 Common Peroneal (CP) nerve test electrode configuration, experiment procedure and testing setup

Flexible Neural Clip (FNC)

To demonstrate reliable and repetitive *in vivo* experiments, we used flexible neural clip (FNC) interface. This interface allows easy and conformal implantation on a variety of peripheral nerves in a manner analogous to clipping a paper clip. The FNC can be implanted onto a peripheral nerve easily by inserting the nerve between the clip-strip and clip-springs after slightly bending the clip-springs (Figure S2.1(a i-iii)). This interface provides not only conformal contact with the nerve, but also gentle pressure on the nerve to keep the clip interface in place. Figure S2.1(b) shows the clip dimensions (length, width, and thickness of the clip-springs, clip-strip, and clip-cavities). The size of the clip-cavity was $700\ \mu\text{m} \times 500\ \mu\text{m}$, and the clip strip was $650\ \mu\text{m} \times 900\ \mu\text{m}$. The width of clip-spring was the same as the length of cavity ($700\ \mu\text{m}$) to maintain the spring elasticity of the polyimide. Two active electrodes (each $17672\ \mu\text{m}^2$) were located on the center of the clip-strip with the distance of $350\ \mu\text{m}$ for reliable position and stimulation of the implanted nerve. This FNC can cover bigger (diameter: $\sim 600\ \mu\text{m}$) or smaller sizes (diameter: $\sim 300\ \mu\text{m}$) of nerves owing to the functionality of the clip design during acute *in vivo* test.

The flexible neural clip (FNC) consisted of a polyimide-Au-polyimide sandwiched structure fabricated by micro-electro-mechanical system (MEMS) technology. The detailed fabrication process is described in previous paper ^[1]. To enhance electrochemical characteristics of stimulation, the released electrodes were coated with electrodeposited iridium oxide film (EIROF), which show shows the largest CSC and lowest impedance ^[2]. The coated IrO_2 on Au sensing electrodes showed a good impedance value ($1.9 \pm 0.09\ \text{k}\Omega$ at $1\ \text{kHz}$, $n=10$), and a cathodic charge storage capacity ($56.4 \pm 2.42\ \text{mC/cm}^2$, $n=10$) for the stimulation. These values are comparable or even better to materials used previously in the literature for neural stimulation ^[2-4]. This result demonstrates that the IrO_2 coated electrodes can be used for *in vivo* stimulation experiments.

Rat preparation for In vivo test

Adult female Sprague-Dawley rats (200-300g) were used for acute *in vivo* experiments in this study. All procedures were performed in accordance with protocols approved by the Institutional Animal Care and Use Committee of the National University of Singapore. The methods were carried out in accordance with the 143/12 protocol. For each experiment, the rat was anesthetized with a mixture (0.2 ml/100 g) of ketamine (37.5 mg/ml) and xylazine (5 mg/ml) intraperitoneally (I.P.), and supplementary doses of 0.1 ml/100 g were injected for maintenance. For the sciatic nerve branch experiments, after an adequate depth of anesthesia was attained, the right sciatic nerves were exposed through a gluteal splitting incision for FNC interface. The FNCs were then implanted on common peroneal (CP) nerve (Figure S2.1(d)) and tibial nerve (Figure S2.1(e)), respectively for each experiment. Stimulations through the FNC were conducted for CP nerve and tibial nerve, respectively (Figure S2.1(c)). Force was measured with a dual-range force sensor (Hand dynamometer, Vernier, USA with NI-DAQ USB-6008, National instruments, USA) tied to the ankle of the animal.

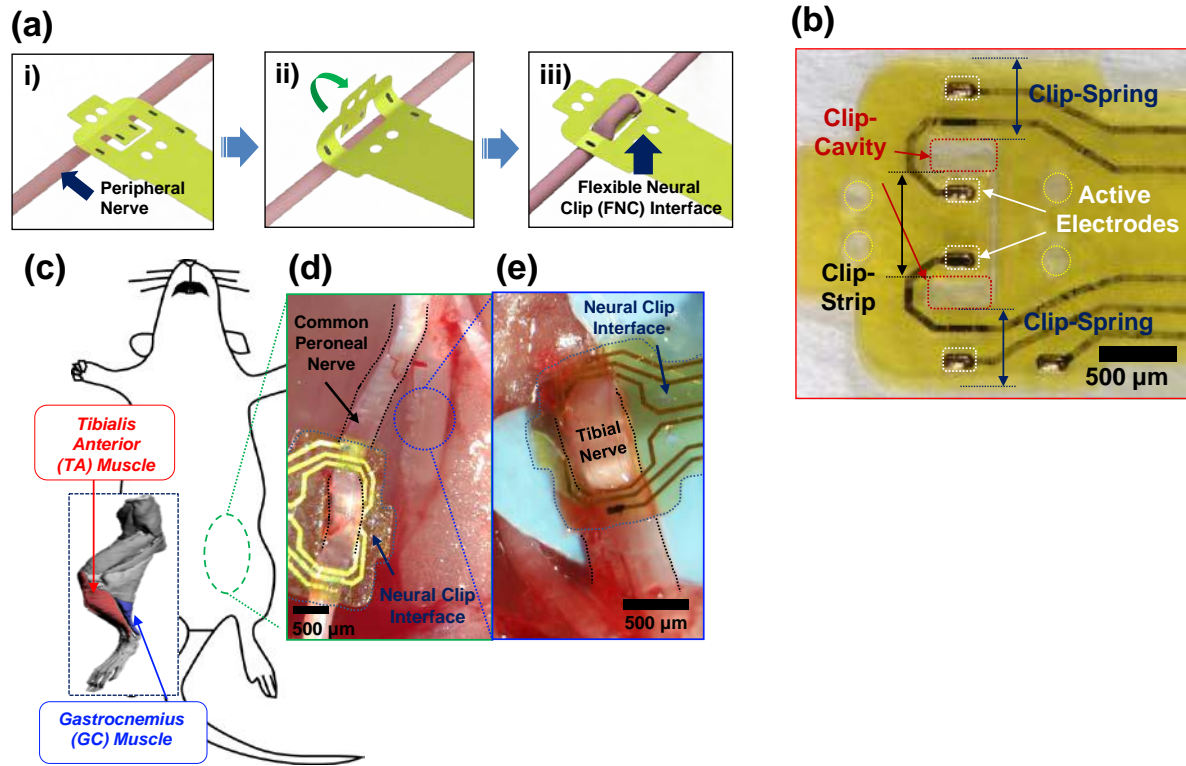


Figure S2.1. (a) Schematic diagram of the steps involved in implanting the FNC on a peripheral nerve (i-iii). (b) Photomicrographs of the fabricated FNC and (inset) clip-head. (c) Schematic diagram and photomicrographs of sciatic nerve branches; (d) common peroneal nerve and (e) tibial nerve.

S2.2 Cortical stimulation with sciatic nerve recording test electrode configuration, testing setup, detailed procedure and testing parameters

Animals

Female Sprague-Dawley rats (200-300g) were used in the acute experiments. Rats were housed and cared for in compliance with the guidelines of the National Advisory Committee for Laboratory Animal Research (NACLAR) and were humanely euthanized after the experiment. During the experiment, isoflurane was used to induce general anesthesia (Aerrane®, Baxter Healthcare Corp., USA) prior to injection of ketamine/xylazine (37.5% ketamine, 5% xylazine, 0.2 ml / 100 g Comparative Medicine, NUS). Paw retraction reflex and breathing rate was used to assess the depth of anesthesia, and the core body temperature at 37°C was maintained using a heating pad (Stryker T/pump, Kent Scientific Corp., USA). Rats were then placed in a stereotaxic frame (Kopf instruments, USA). Microsurgical techniques were used to expose the left sciatic nerve, the tibialis anterior and the skull, which was then subjected to a craniotomy to access the right motor cortex.

Stimulation and Recording

A tungsten single shank electrode (0.5MΩ, Microprobe Inc, USA) was implanted into the motor cortex in several locations at a depth of 2.0mm (near the layer V motor cortex pyramidal neurons) until the tibialis anterior was observed to move with a stimulation (100 μA). Once a movement was observed, the location was used for the subsequent experiment.

A thin-filament longitudinal intrafascicular electrode was used in the sciatic nerve to record stimulation artifacts and nerve activity during stimulation. Furthermore, using a string tied to the hind paw of the rat attached to a dynamometer (Hand dynamometer, Vernier, USA with NI-DAQ USB-6008, National instruments, USA), force was recorded simultaneously.

S2.3 Pelvic nerve test electrode configuration, testing setup, detailed procedure and testing parameters

Animal subject and surgery

Female Sprague-Dawley rats (200-300 g) were used in the acute experiments. The animals were housed in pairs in individually ventilated cages, maintained in a 22-24°C room with a 12 h light–dark cycle, and given ad libitum access to food and water. All procedures were performed in accordance with protocols approved by the Institutional Animal Care and Use Committee of the National University of Singapore. For each experiment, the animal was anesthetized with a mixture (0.2 ml/100 g) of ketamine (37.5 mg/ml) and xylazine (5 mg/ml) intraperitoneally (I.P.) for induction, and a supplementary dose of 0.1 ml/100 g was injected I.P. for maintenance as required. The animal was placed in the supine position, and kept warm with a water-circulating heating pad. Laparotomy was performed, and underlying muscles were cut and adipose and connective tissues were gently teased apart to expose the pelvic nerve branches for electrical stimulation. To record muscle activity from the external urethral sphincter (EUS), the pubic bone overlying the urethra was cut and fat tissues were teased apart.

Pelvic Nerve stimulation and EUS EMG recording

Hook electrodes made from platinum iridium wires (A-M systems, 0.005” bare, 0.008” coated) were implanted onto the pelvic nerve branches unilaterally and silicone elastomer (Kwik-Sil, World Precision Instruments, FL, USA) was used to encase the electrode-nerve interface. A commercial isolated stimulator (A-M systems model 2100, WA, USA) was used to deliver either cathodic, anodic or biphasic rectangular pulse for pelvic nerve stimulation at a repetition frequency of 2 Hz and current amplitude of 70 μ A and different pulse widths (20, 60, 100, 150, 200, 300, 400, 500 μ s) used for each set of stimulation. A pair of fine stainless steel wires (304, California Fine Wire, CA, USA) with exposed tips was sutured to the top of the exposed urethra beneath the dissected pubic bone to record EUS EMG signals. EMG signals were amplified by using an Intan preamplifier 2216, and acquired at 20 kHz with the Intan RHD2000 data acquisition board (Intan Technologies), with a 50 Hz notch filter. Stimulation pulse markers were sent from the stimulator to the data acquisition board (DAQ) collecting EMG data simultaneously for data synchronization.

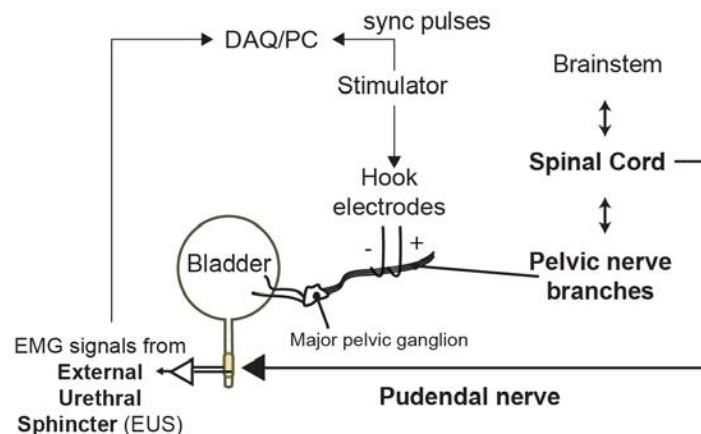


Figure S2.3 Pelvic Nerve stimulation and EUS EMG recording

S2.4 Tibialis Anterior (TA) muscle test electrode configuration, experiment procedure and testing setup

Sprague-Dawley rats (around 450g) were used in the acute experiments. Rats were housed and cared for in compliance with the guidelines of the National Advisory Committee for Laboratory Animal Research (NACLAR) and were humanely euthanized after the experiment. During the experiment, isoflurane was used to induce and maintain general anesthesia (Aerrane®, Baxter Healthcare Corp., USA). The Tibialis Anterior (TA) muscle was exposed for electrode implantation. Our home-made double-side polyimide electrode (Figure S2.4) was sutured into the muscle belly, transversal to muscle fibers in TA muscle. Current stimulation was delivered from A-M SYSTEMS model 4100 isolated high-power stimulator. Every one second, a train of pulses of 60 Hz was applied. In the experiment of comparing four waveforms, positive-negative biphasic pulses, negative-positive biphasic pulses, positive monophasic pulses, and negative monophasic pulses were applied. Force was measured with a dual-range force sensor (Hand dynamometer, Vernier, USA with NI-DAQ USB-6008, National instruments, USA) tied to the ankle of the animal.

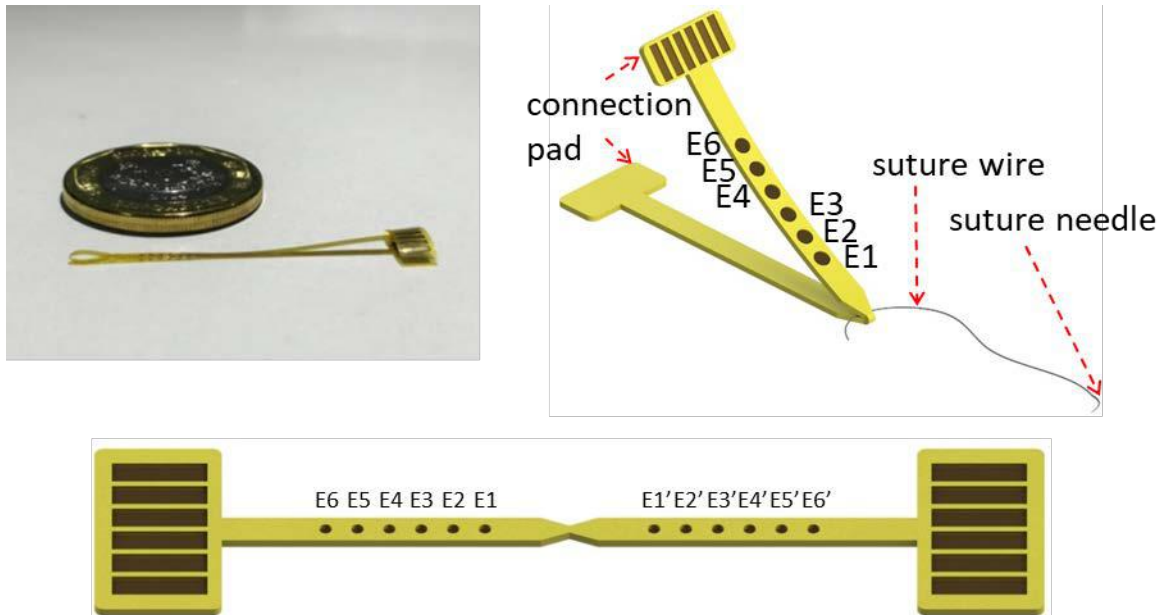


Figure S2.4 Detailed configuration of the home-made electrode for TA muscle stimulation

S3 Experiment data

S3.1 Detailed force mapping curve and voltage waveform of sinewave test on CP nerve

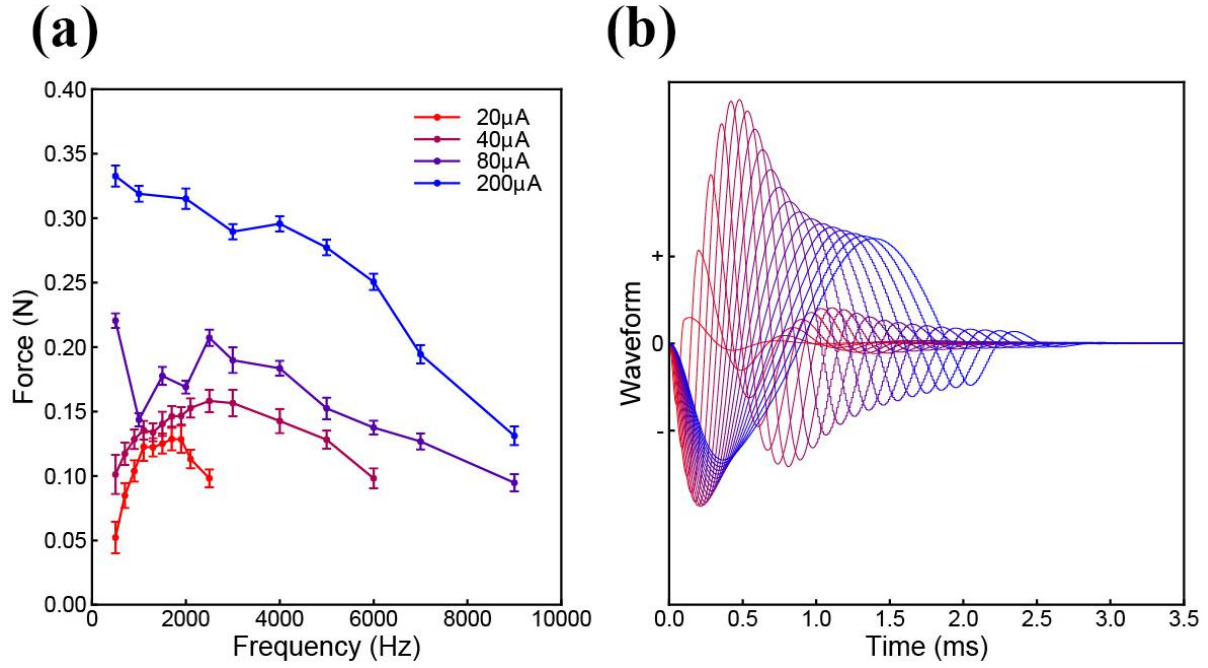


Figure S3. (a) Force mapping result of sinewave test on CP nerve with error bar; (b) The corresponding voltage waveform of sinewave current with same amplitude but different pulse width.

S3.2 Stimulus artifact data

S3.2.1 Stimulus artifact of cortical stimulation

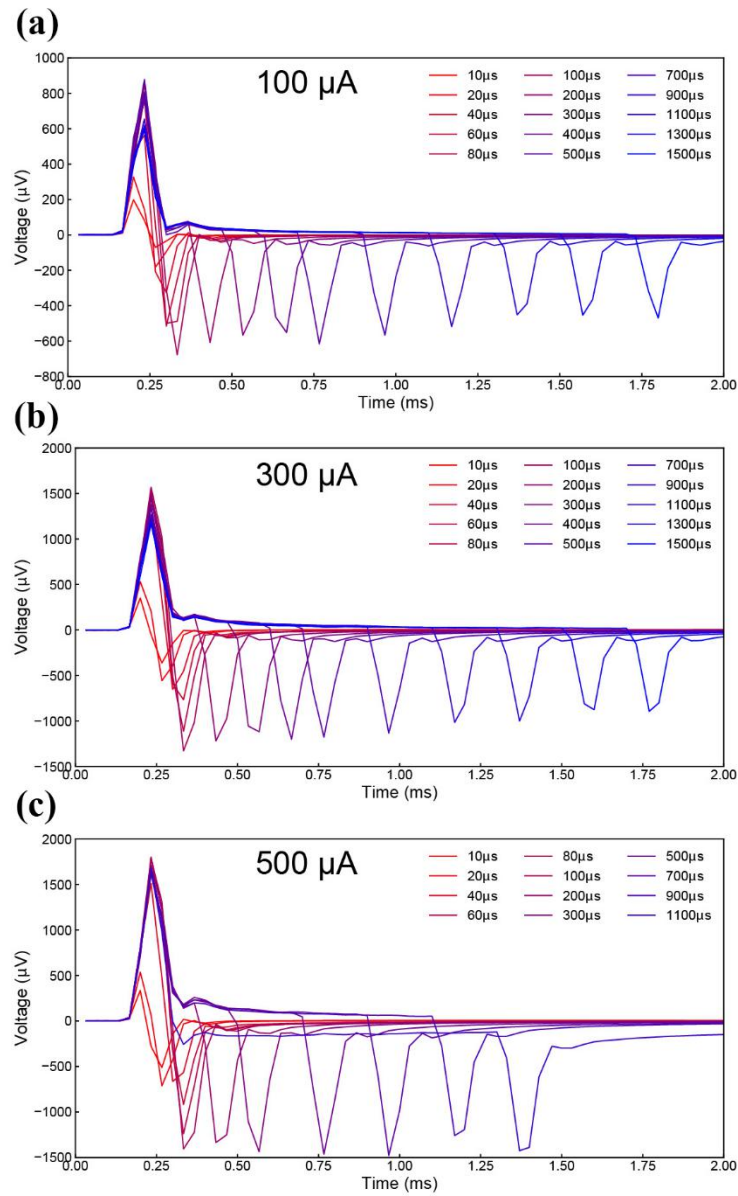


Figure S3.2.1.1. Stimulus artifact of cortical stimulation with different current amplitude of negative monophasic square waveform. The SPPW range is from 10 μs to 1500 μs .

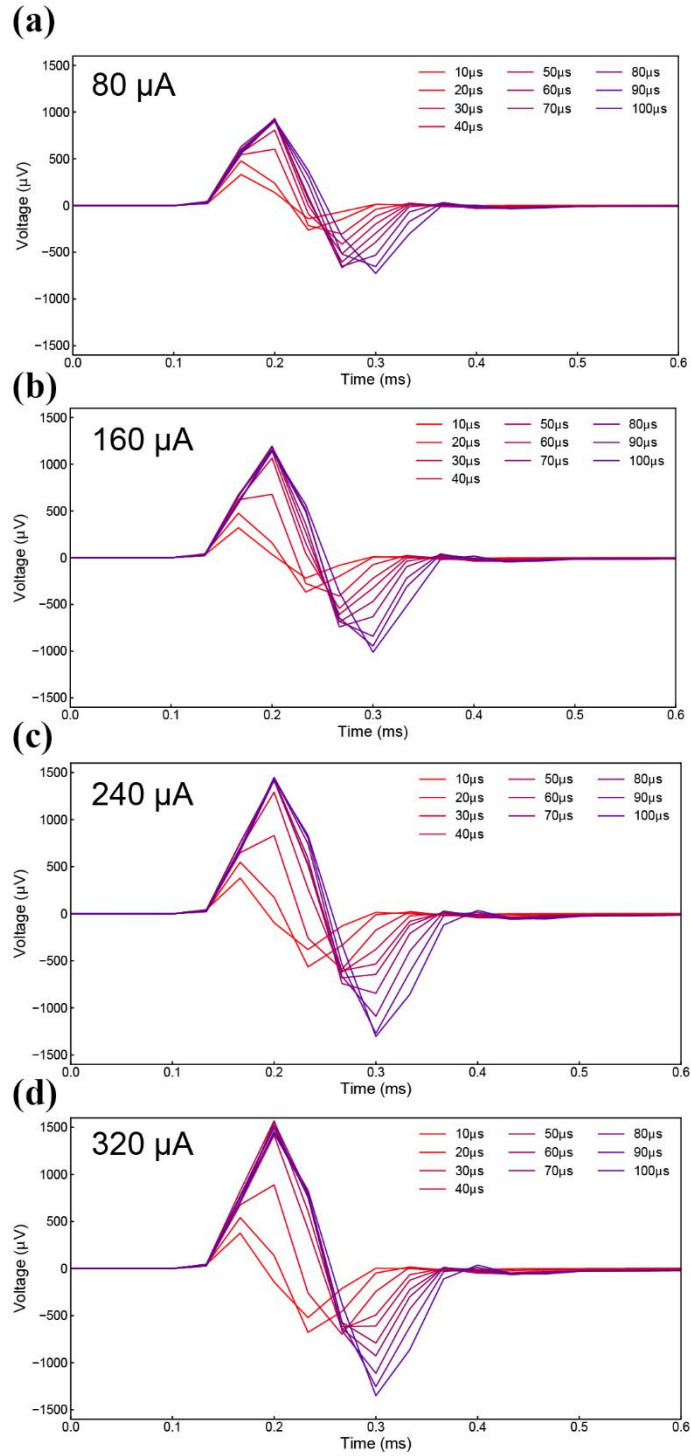


Figure S3.2.1.2. Stimulus artifact of cortical stimulation with different current amplitude of negative monophasic waveform. The SPPW range is from 10 μs to 100 μs .

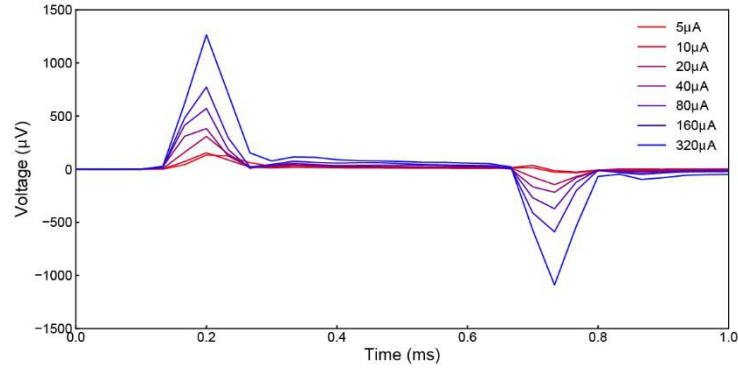


Figure S3.2.1.3. Stimulus artifact of cortical stimulation with negative monophasic waveform current of 500 μ s SPPW. The current is from 5 μ A to 320 μ A.

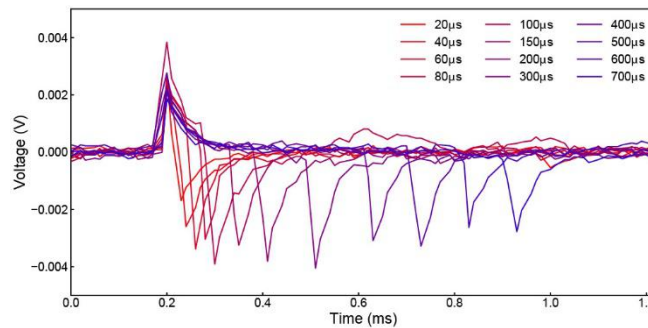


Figure S3.2.1.4. High sampling rate system (70 kHz) recording of stimulus artifact of cortical stimulation with negative monophasic waveform current of 100 μ A. The SPPW is from 20 μ s to 700 μ s.

Figure S3.2.1.1 to Figure 3.2.1.4 show other testing data of stimulus artifacts for cortical stimulation.

In Figure S3.2.1.1, different amplitudes of negative monophasic square waveform current were applied. The shape and the changing trend of the artifacts follow the same pattern as shown in Figure 3(e). The current amplitude has no effect upon the waveform of the stimulus artifact. The similar test with a lower SPPW range, from 10 μ s to 100 μ s, is shown in Figure S3.2.1.2. A more detailed test with different amplitudes but constant SPPW is shown in Figure S3.2.1.3. The current amplitude has no effect upon the shape of the stimulus artifacts.

Since the sampling rate of our recording system is 30 kHz, which may cause large distortion of the recording of high frequency signal. Thus the same stimulus artifact is recorded with another recording system with higher sampling rate, which is 70 kHz, as shown in Figure S3.2.1.4. The recording result shows the same pattern as the data of 30 kHz sampling rate system, only with more noise.

These results affirm the repeatability of the stimulus artifact recording in our tests.

S3.2.2 Stimulus artifact of pelvic stimulation

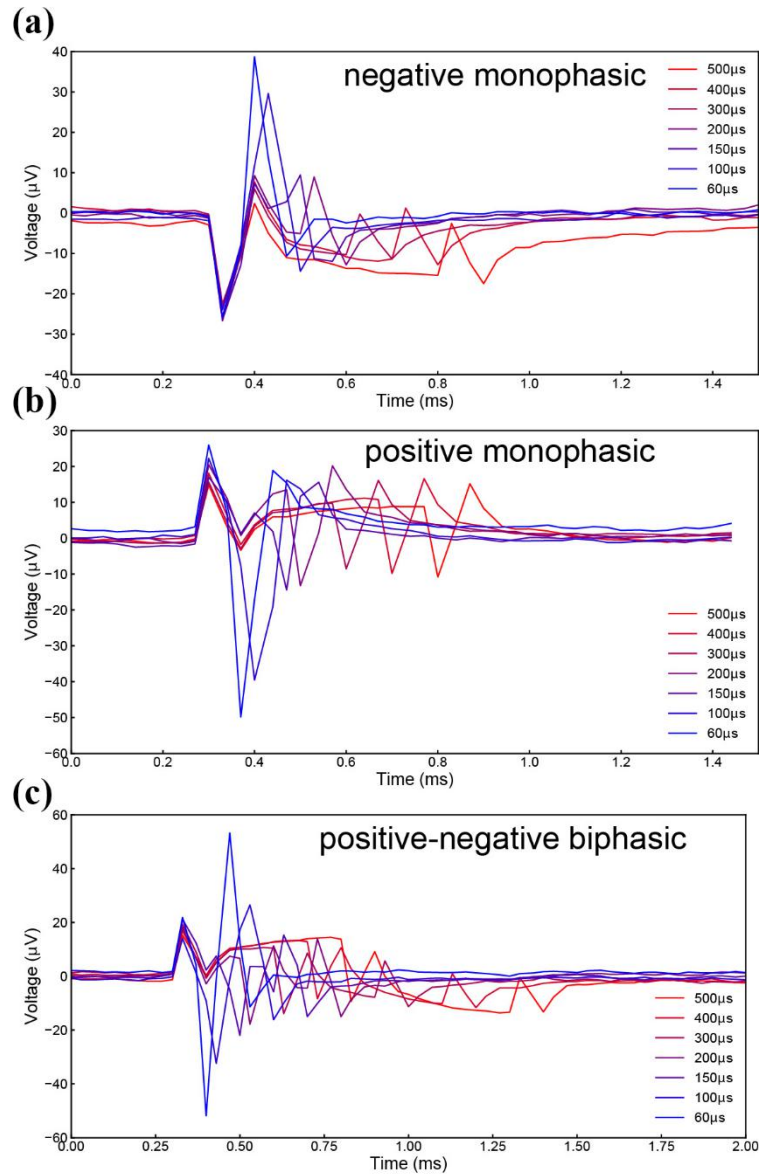


Figure S3.2.2. Stimulus artifact of pelvic stimulation with different current waveform of $70\text{ }\mu\text{A}$; (a) Positive monophasic square waveform; (b) Negative monophasic square waveform; (c) Positive-first biphasic square waveform.

Another set of stimulus artifact recording data of pelvic nerve stimulation is shown in Figure S3.2.2. This set of data shows a very high resonance frequency, indicating that the recording system may not be able to capturing the waveform of the signal well. So we do not try fitting it by modeling. But it still shows a clear voltage response of the RLC circuit. The voltage amplitude reaches maximum at a certain pulse width, which is $60\text{ }\mu\text{s}$ in this case.

S3.3 Experiments of TA muscle stimulation

S3.3.1. Complete TA muscle modeling result with combination of two groups of muscles

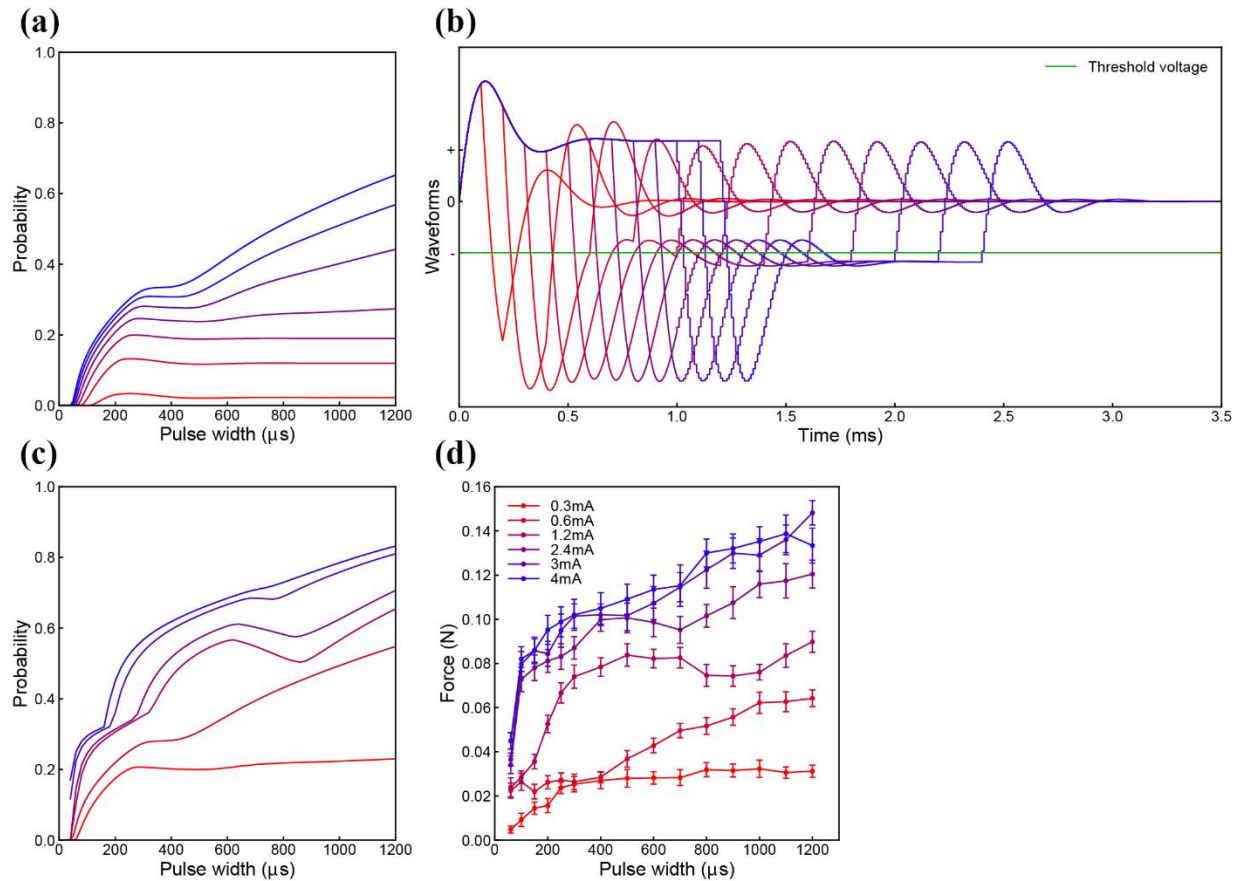


Figure S3.3.1. Combined modeling result of TA muscle stimulation. (a) the probability mapping of the second group of muscle; (b) The corresponding voltage waveform of (a); (c) The combined probability mapping of two group of muscles; (d) The force mapping result of TA muscle stimulation.

Since the two lowest curves in Figure 5(b) has a relatively large mismatch with the counterparts in the force mapping data, another set of the parameters is required to fit these two curves. It means that with different current amplitude, different number of muscle group can be stimulated, which is already reported by previous study ^[5]. Based on the pattern shown by these two curves, a detailed probability mapping result with the same pattern is shown in Figure S3.3.1(a). The corresponding voltage waveform is shown in Figure S3.3.1(b). The detailed modeling parameters can be found in Table 1-S3.3.1(a). A combined probability mapping result is shown in Figure S3.3.1(c). The lowest two curves are from the second muscle group in Figure S3.3.1(a) and other curves are from Figure 5(b). The force mapping data is shown in Figure S3.3.1(d) for comparison with the probability mapping result. The whole changing trend of the force mapping curves can be well reproduced by the modeled probability mapping.

S3.3.2 Four waveforms comparison of TA muscle stimulation

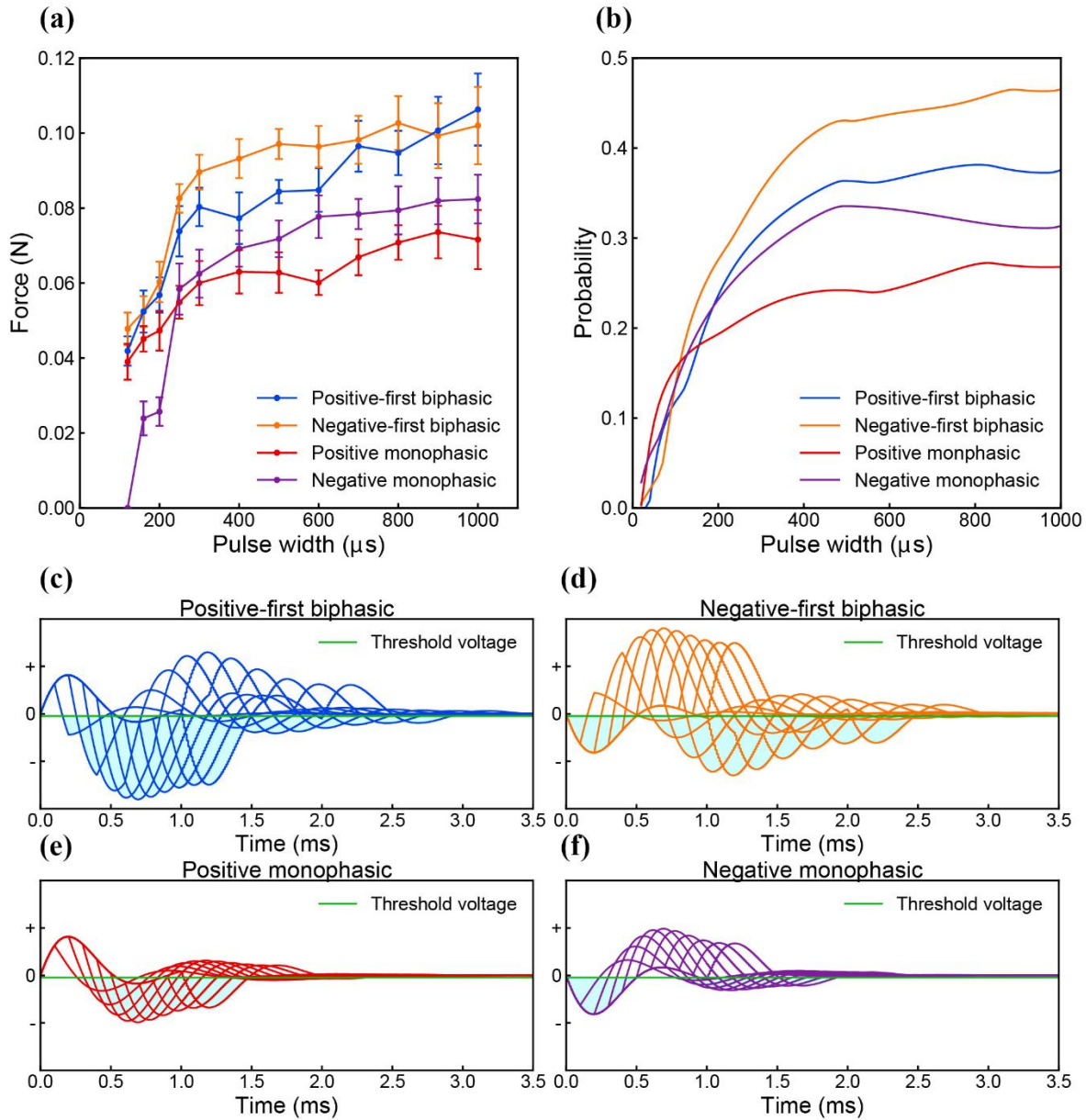


Figure S3.3.2. Four waveforms comparison of TA muscle stimulation with the same current amplitude. (a) Force mapping results; (b) Probability mapping results; (c)-(f) Voltage waveforms of four different current waveforms: (c) Positive-first biphasic square waveform; (d) Negative-first biphasic square waveform; (e) Positive monophasic square waveform; (f) Negative monophasic square waveform.

It is widely reported that negative current will be more effective for nerve stimulation because the depolarization of the ion channel is gated by negative voltage. However, the difference of the stimulation result between biphasic and monophasic square waveform cannot be well explained. Since in the C-P theory the probability mapping curve is directly determined by the voltage waveform, current of different square waveforms will generate different probability mapping curves. With the correct circuit and probability calculus parameters, the probability mapping curves of different current waveforms of the same amplitude can be modeled.

To validate this prediction, a force mapping comparison of different current waveforms upon TA muscle were conducted. Four typical current waveforms of the same amplitude, which is 180 μA , were used. The force mapping results are shown in Figure S3.3.2 (a). These four current waveforms show completely different efficiency for muscle stimulation even though they share the same current amplitude. Since the shape of these four curves do not reveal very clear circuit parameters such as resonance frequency and damping factor, just as the pattern as shown in Figure 6(b-i), exhaustive method was applied to capture the modeling parameters (Table 1-S3.3.2 (b)). The modeling results are shown in Figure S3.3.2 (b). The corresponding voltage waveforms of these four types of square wave current are shown in Figure S3.3.2 (c) to (f). It should be noted that the voltage waveforms of Figure S3.3.2 (c) and (d) are just of opposite polarity since they share the same current waveform with opposite polarity. Figure S3.3.2 (e) and (f) are of the same situation. However, the positive and negative phase of the whole voltage waveform are asymmetrical, making the effective voltage area for probability calculus form different shapes, amplitudes and changing trends. Apparently, these different effective voltage areas will result in different probability mapping curves as shown in Figure S3.3.2 (b). The same test was conducted for three times. The testing and modeling results of another two tests are shown in **Supplementary S3.3.3**. All these three tests reveal that these four types of square wave current generate force mapping curves with different shape and stimulation efficiency.

S3.3.3 Other experiments of four waveforms comparison of TA muscle stimulation

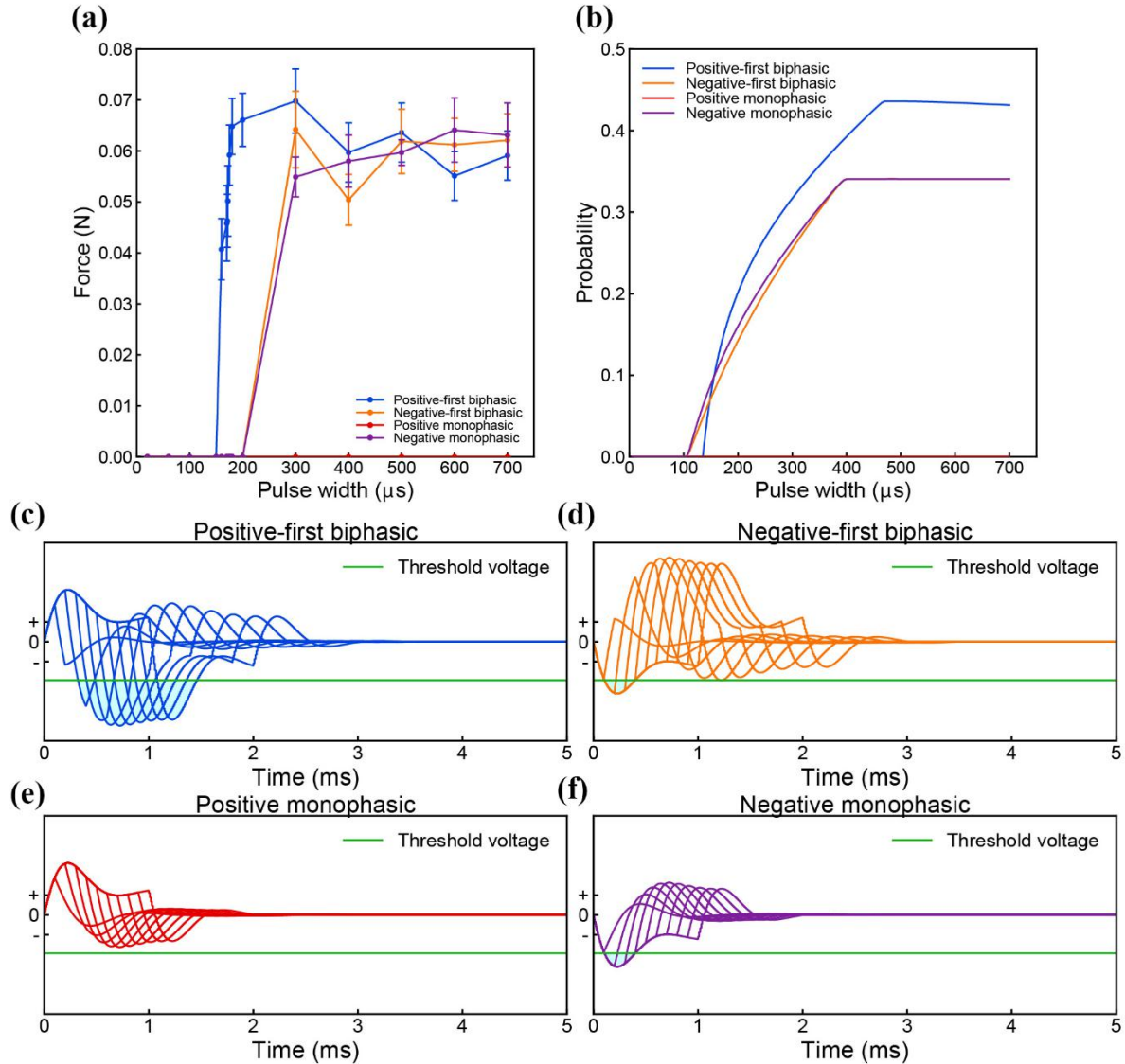


Figure S3.3.3.1. Four waveform comparison test of TA muscle stimulation with 520 μA current amplitude. (a) Force mapping data; (b) Probability mapping result; (c) Voltage waveform of positive-first biphasic square waveform current; (d) Voltage waveform of negative-first biphasic square waveform current; (e) Voltage waveform of positive monophasic square waveform current; (f) Voltage waveform of negative monophasic square waveform current;

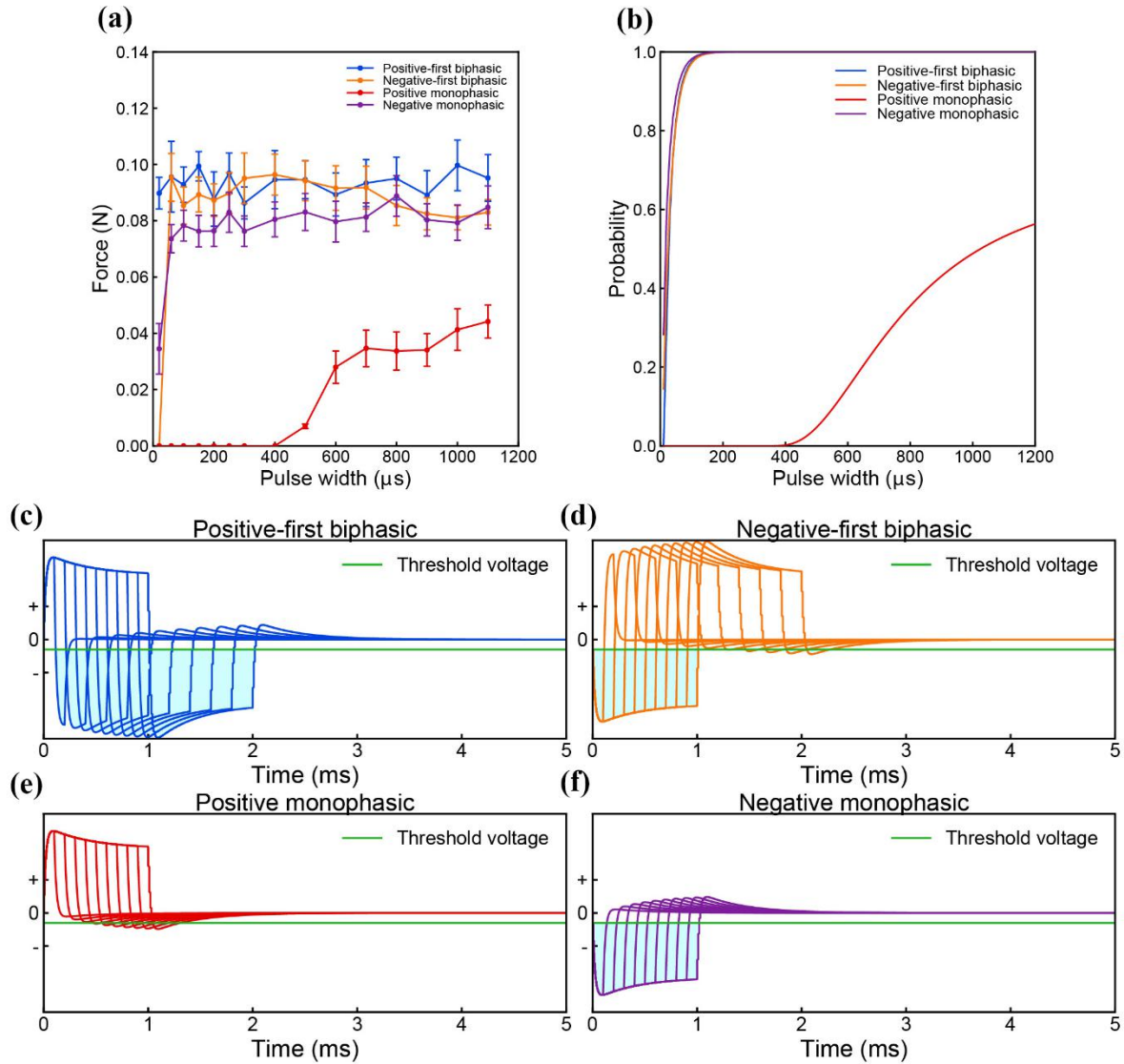


Figure S3.3.3.2. Four waveform comparison test of TA muscle stimulation with 500 μA current amplitude. (a) Force mapping data; (b) Probability mapping result; (c) Voltage waveform of positive-first biphasic square waveform current; (d) Voltage waveform of negative-first biphasic square waveform current; (e) Voltage waveform of positive monophasic square waveform current; (f) Voltage waveform of negative monophasic square waveform current;

Figure S3.3.3.1 and S3.3.3.2 show the four waveform comparison tests with 520 μA and 500 μA current amplitude in another two experiments, respectively. In Figure S3.3.3.2, apart from the positive square wave, other three waveforms show almost the same force mapping curve, so in the probability mapping result, these three curves are overlapped with each other.

S3.4 Experiments of CP nerve stimulation

S3.4.1 CP nerve stimulation results by negative monophasic square wave current pulse

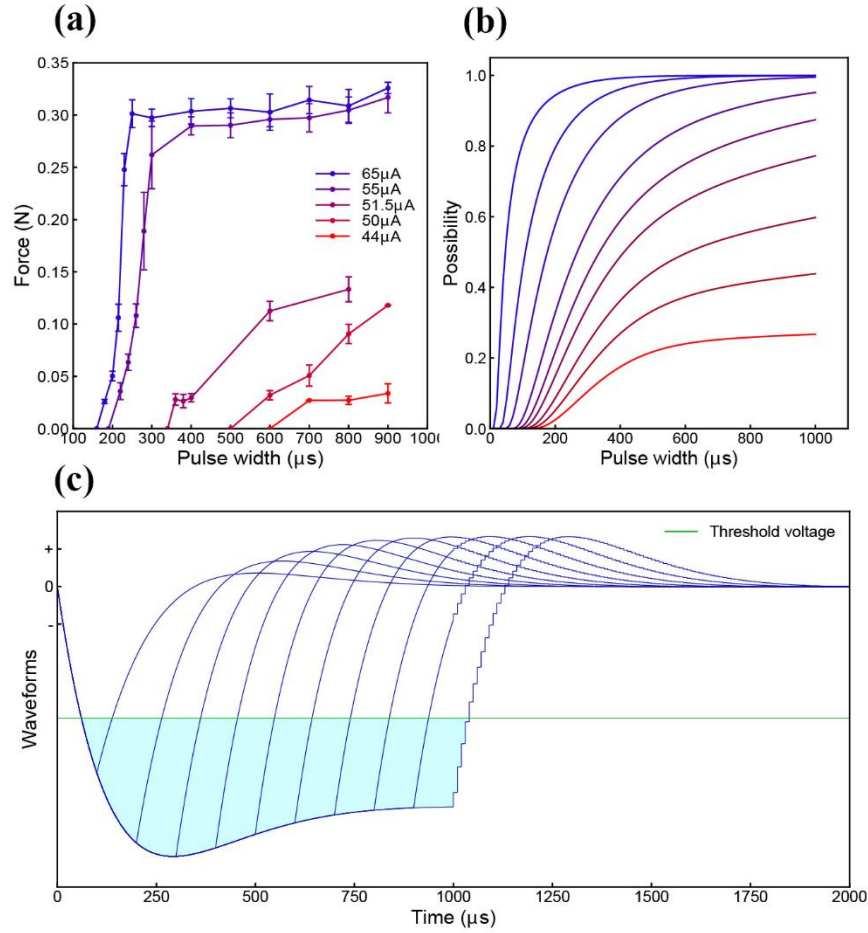


Figure S3.4.1. Measurement and modeling results of the CP nerve stimulation by negative monophasic square waveform current. (a) Force mapping results; (b) Probability mapping results; (c) Corresponding voltage waveforms.

Since we consider C-P theory as a general theory for describing the electrical activation of different neural and non-neural tissues, we also did similar tests on the CP nerve, the cortex and the pelvic nerve.

The force mapping curve of CP nerve stimulation with negative monophasic square wave current is shown in Figure S3.4.1(a). The current is varied from 44 μA to 65 μA and the SPPW mapping range is from 100 μs to 900 μs . The force mapping pattern is quite similar as the one shown in Figure 6(a). A set of parameters (Table 1-S3.4.1(b)) is captured for the modeling result as shown in Figure S3.4.1(b). The resonance frequency used in this modeling is 714 Hz. All the curves show a monotonically increasing trend with SPPW, just as the force mapping curve. The corresponding voltage waveform is plotted in Figure S3.4.1(c). In this case, V_{DC} is much higher than $V_{Threshold}$, making the effective voltage area increase monotonically with SPPW.

S3.4.2 Four waveforms comparison of CP nerve stimulation

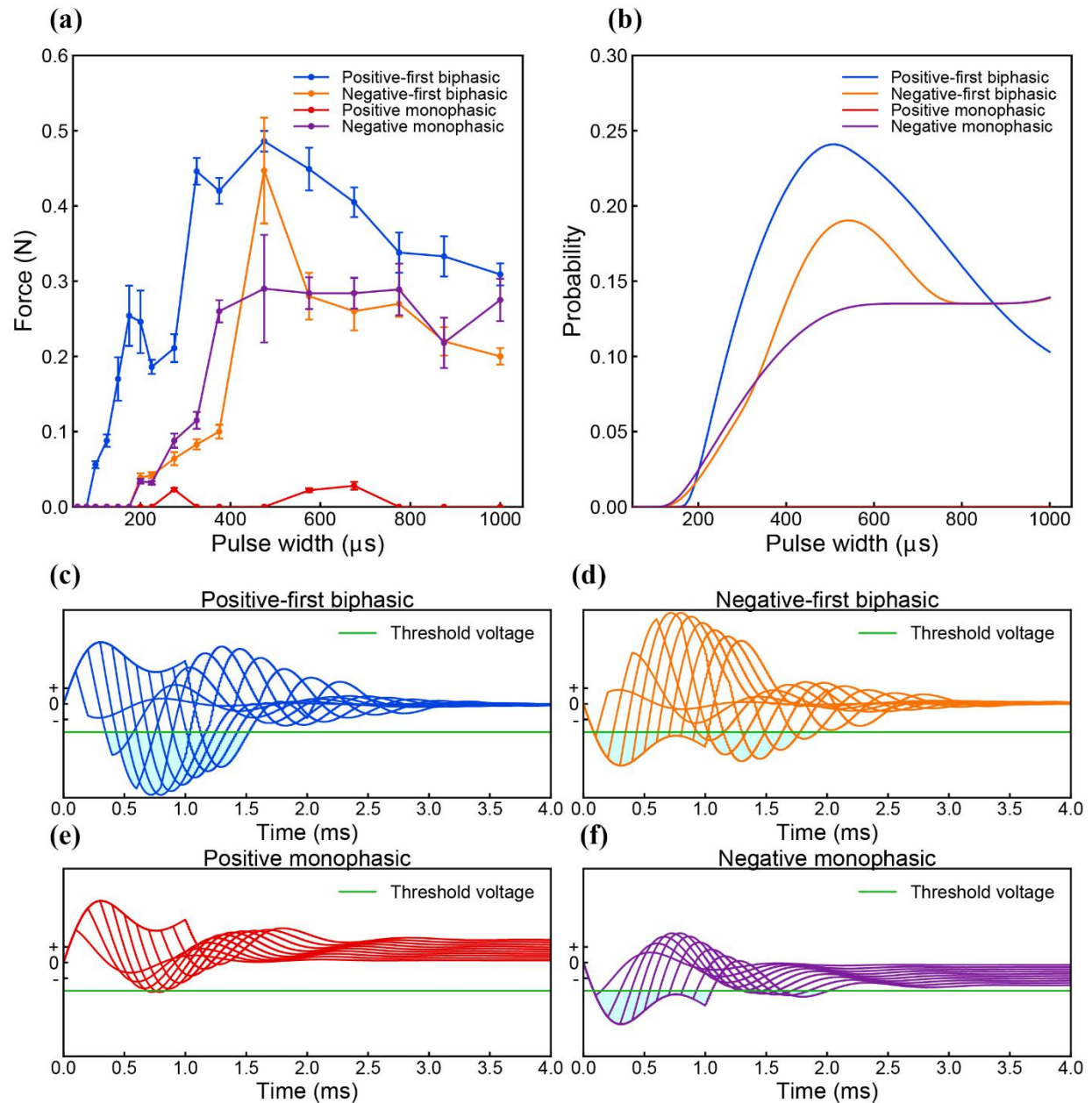


Figure S3.4.2. Four waveforms comparison of CP nerve stimulation of the same current amplitude. (a) Force mapping results; (b) Probability mapping results; (c)-(f) Voltage waveforms of four different current waveforms: (c) Positive-first biphasic square waveform; (d) Negative-first biphasic square waveform; (e) Positive monophasic square waveform; (f) Negative monophasic square waveform.

The force mapping comparison of four different square waveforms of CP nerve stimulation is shown in Figure S3.4.2(a). The curves of positive-first biphasic and negative-first biphasic waveform all show a distinctive resonance effect at SPPW of 475 μs, indicating that the resonance frequency is 1052 Hz. Compared with the resonance frequency used in Figure S3.4.1(b), which is 714 Hz, the frequency in this test is higher. This also indicates that this resonance frequency will vary with different individuals.

The curve of monophasic negative waveform does not show a clear resonance peak and get close to or even higher than the curve of negative-first biphasic waveform at high SPPW range. This trend is very weird because normally the biphasic waveforms should have a higher stimulation efficiency than monophasic waveforms. In Figure S3.3.2(c)-(f), it is very clear that the voltage curve of biphasic waveforms should give a larger effective voltage area than that of monophasic waveforms. Even by exhaustive method, we are not able to capture a set of proper parameters to fit these curves in Figure S3.4.2(b). So the circuit used for modeling in this test is revised based on the circuit shown in Figure 2(c). An additional capacitor is connected in series with the inductor. The detailed circuit structure and analysis method can be found in the **Supplementary S1.2**. The corresponding modeling result is shown in Figure S3.4.2(b) and the detailed parameters can be found in Table 1-S3.4.2(b). The voltage waveforms of these four waveforms are shown in Figure S3.4.2(c)-(f).

S3.5 Experiments of cortical stimulation

S3.5.1 Cortical stimulation results by negative monophasic square wave current pulse

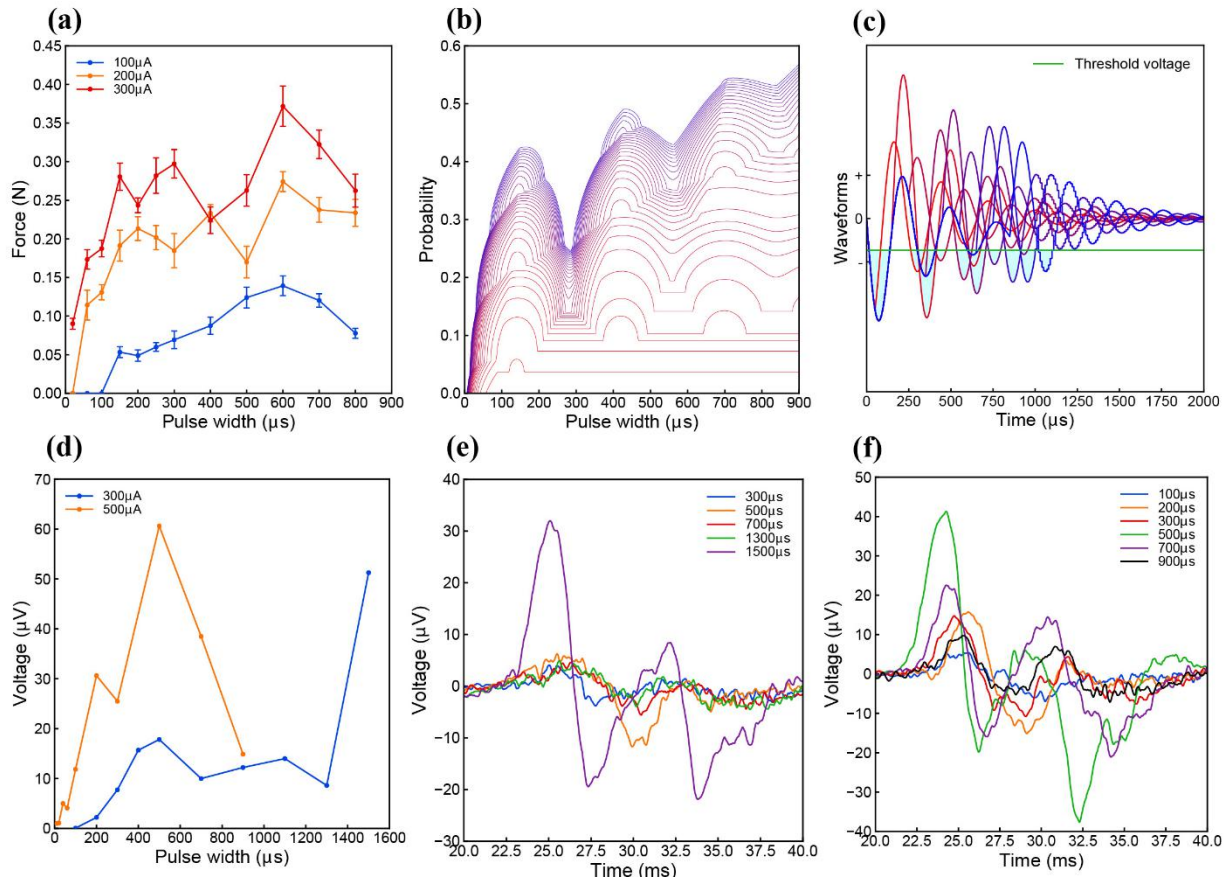


Figure S3.5.1 Measurement and modeling results of the cortical stimulation by negative monophasic square waveform current. (a) Force mapping results; (b) Probability mapping results; (c) Corresponding voltage waveforms; (d) Amplitude of EMG signal with two different current amplitudes; (e) Selected EMG waveforms of 300 μA stimulation; (f) Selected EMG waveforms of 500 μA stimulation;

This C-P theory can also be applied on cortical stimulations. The detailed testing setup and procedure can be found in the **Supplementary S2.2**. In the cortical stimulation, only negative monophasic square wave current was used for the force mapping test as shown in Figure S3.5.1(a). The force mapping curves show three resonance peaks, which is quite similar to the situation to be discussed in Figure 6(c-i). The multiple resonance peaks indicate that the resonance frequency is higher than that of the TA muscle and the CP nerve, and the damping factor is very low. The probability modeling result is shown in Figure S3.5.1(b) and the detailed modeling parameters can be found in Table 1-S3.5.1(b). The resonance frequency captured is 3600 Hz. The corresponding voltage waveform is shown in Figure S3.5.1(c). Due to the low damping factor, the voltage waveform have a strong oscillation, showing a very complex changing trend. Other similar testing data can be found in the **Supplementary S3.5.2**. All these data will follow the similar probability mapping pattern shown in Figure S3.5.1(b).

To correlate the force mapping results, we also measured the EMG signal from the sciatic nerve by cortical stimulation with negative monophasic square wave current of 300 μA and 500 μA . Some selected EMG waveforms are shown in Figure S3.5.1(e) and (f). The complete testing data including the stimulus artifacts can be found in the **Supplementary S3.5.3**. The peak-to-peak amplitude of the EMG signal is measured

and shown in Figure S3.5.1(d). The EMG signal also shows multi-peak resonance, which is similar as the force mapping results in Figure S3.5.1(a). It seems that the second resonance peak of the force mapping data is between the SPPW from 300 μ s to 400 μ s. However, the second resonance peak of the EMG recoding is at around 500 μ s. This resonance peak shift should be induced by the individual difference.

One point to be emphasized here is that the amplitude of the EMG signal cannot fully represent the number of action potentials generated. Since in our theory the action potential is evoked based on probability, all the action potentials are not generated at the same time but with a time distribution. Especially when there are more than one effective voltage areas, there will be more than one group of action potentials. The actual measured EMG signal is the result of all individually action potentials with a complex phase combination. Even with the same quantity of action potentials generated, meaning the same force generated, the different phase combination will still affect both the amplitude and the pulse duration of the EMG signal measured in the real tests. In both Figure S3.5.1(e) and (f), the EMG waveforms of different SPPW not only differ in amplitude but also in pulse width and shape. So currently the EMG results shown in Figure S3.5.1(d) cannot be fitted with the probability mapping. But we still can get some important information from EMG results such as the resonance frequency.

S3.5.2 Other force mapping data of cortical stimualtions

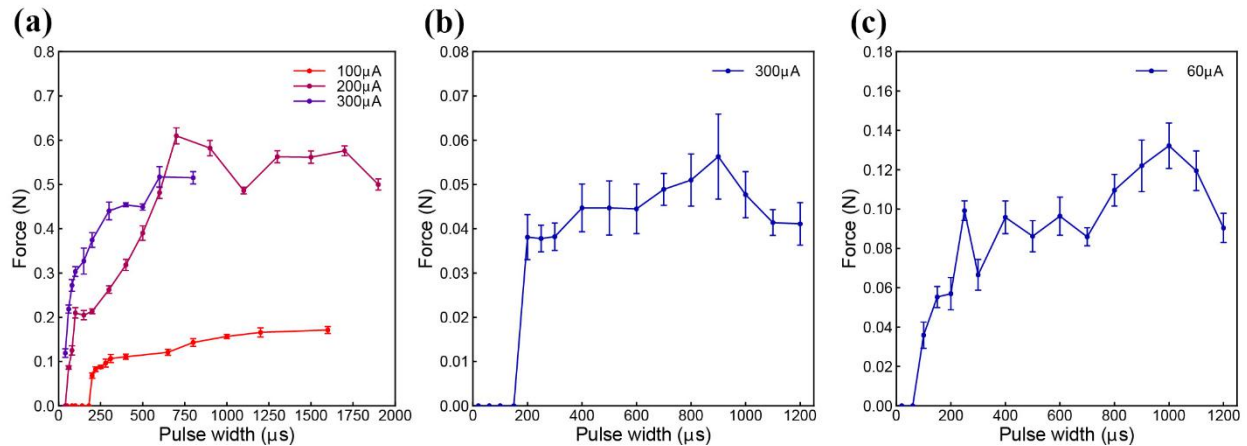


Figure S3.5.2. Cortical stimualtions in three experiments using negative monophasic square waveform current.

Figure S3.5.2 shows the force mapping data cortical stimualtions in another three experiments. The current waveforms are all negative monophasic square waveform. Because the cortex is too fragile, not all the tests can achieve perfect force mapping curve with several current amplitudes. A current amplitude that is too high or a SPPW that is too long will cause brain damage and further affect the testing result. In Figure S3.5.2(a), the curve of 300 μA is even lower than that of 200 μA when the SPPW is higher than 500 μs . The curve of 300 μA is not completed because the brain is damaged afterward and no further stimulation can be detected. The similar situation happened for Figure S3.5.2(b) and (c). In these two tests, only one force mapping curve can be completed. The brain was damaged afterward.

Nervertheless, the shape of the force mapping curves of all these three tests show an obvious multiple resonance peak effect, which agrees with the probability mapping shown in Figure 3.5.2(b). Since all these three tests are either with incompleted data or only with one curve, we did not try fitting these curves by modeling. However, all these curves resemble some probability mapping curves in Figure 3.5.2(b).

S3.5.3 Complete EMG data of cortical stimulation

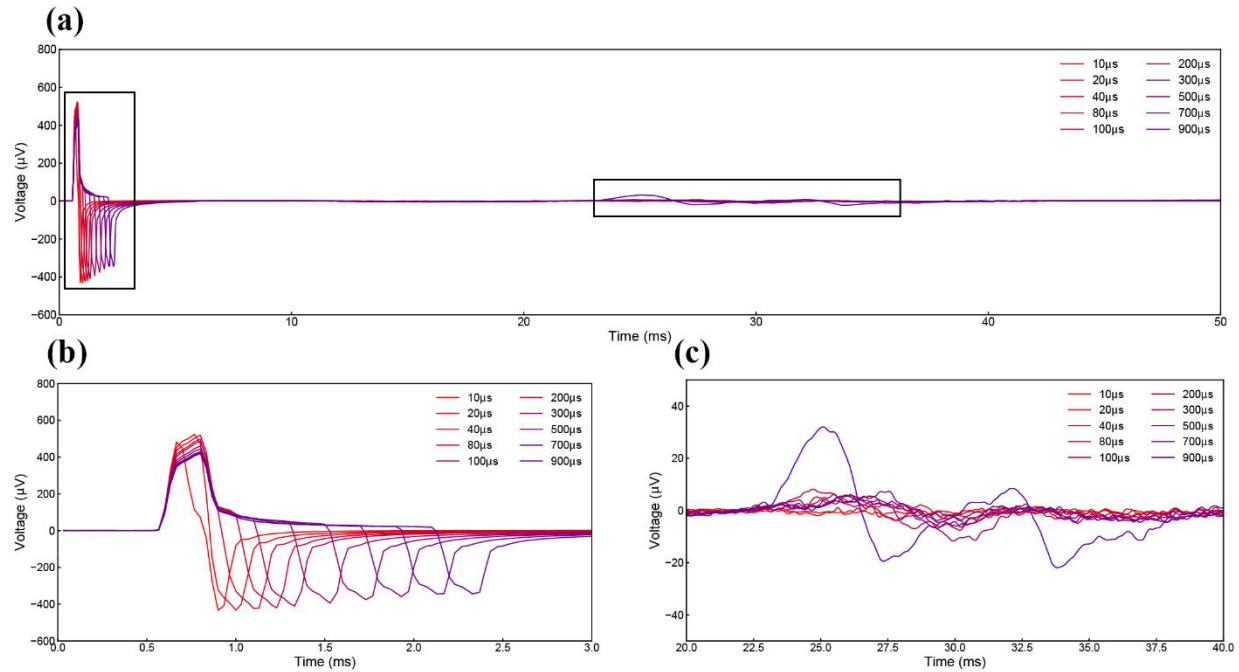


Figure S3.5.3.1 Complete EMG data of cortical stimulations with negative monophasic current waveform of 300 μA ; (a) The complete raw EMG data; (b) The stimulus artifacts; (c) the EMG signal.

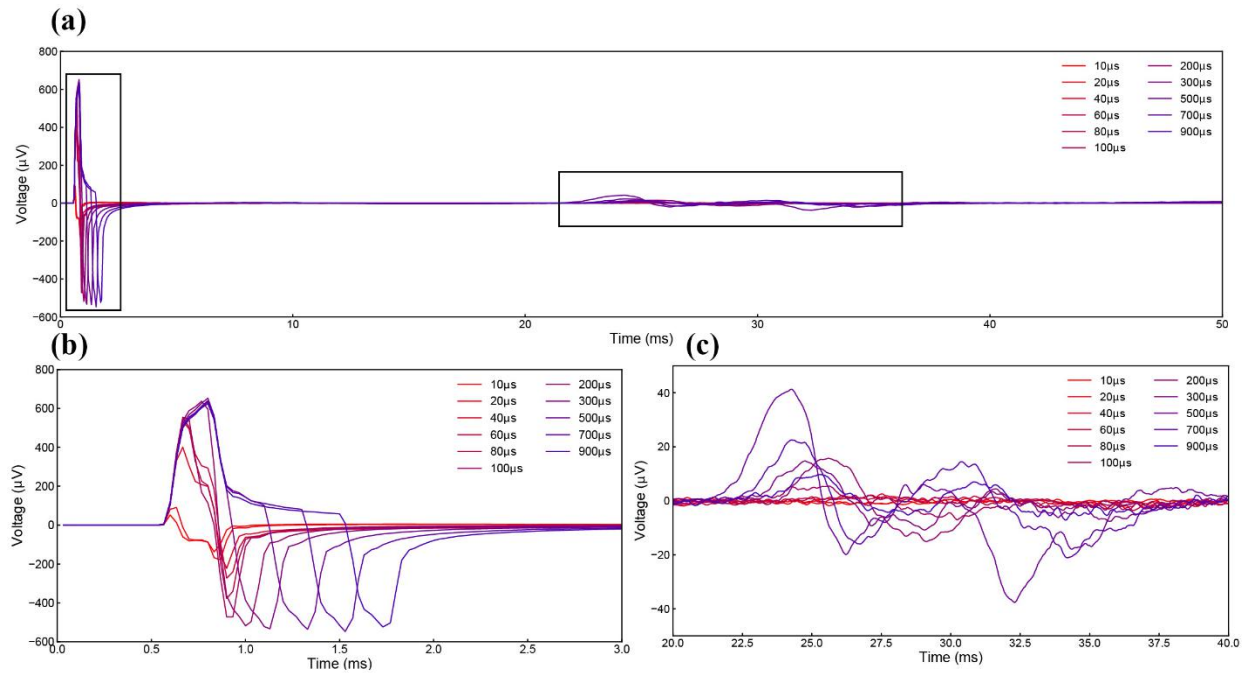


Figure S3.5.3.2 Complete EMG data of cortical stimulations with negative monophasic current waveform of 500 μA ; (a) The complete raw EMG data; (b) The stimulus artifacts; (c) the EMG signal.

The detailed and complete EMG recording results of cortical stimulations with 300 μA and 500 μA are shown in Figure S3.5.3.1 and S3.5.3.2, respectively. Each curve is an average result of 60 trials and no filter

is further applied for signal processing. The artifact follows the same pattern as shown in Figure 3(e). In Figure S3.5.3.2, the EMG signal peaks at SPPW of 500 μ s and then significantly decreases with increasing SPPW, showing a distinctive resonance effect.

S3.6 Experiments of pelvic nerve fibers stimulation

S3.6.1 Pelvic nerve fibers stimulation results by three different current waveforms

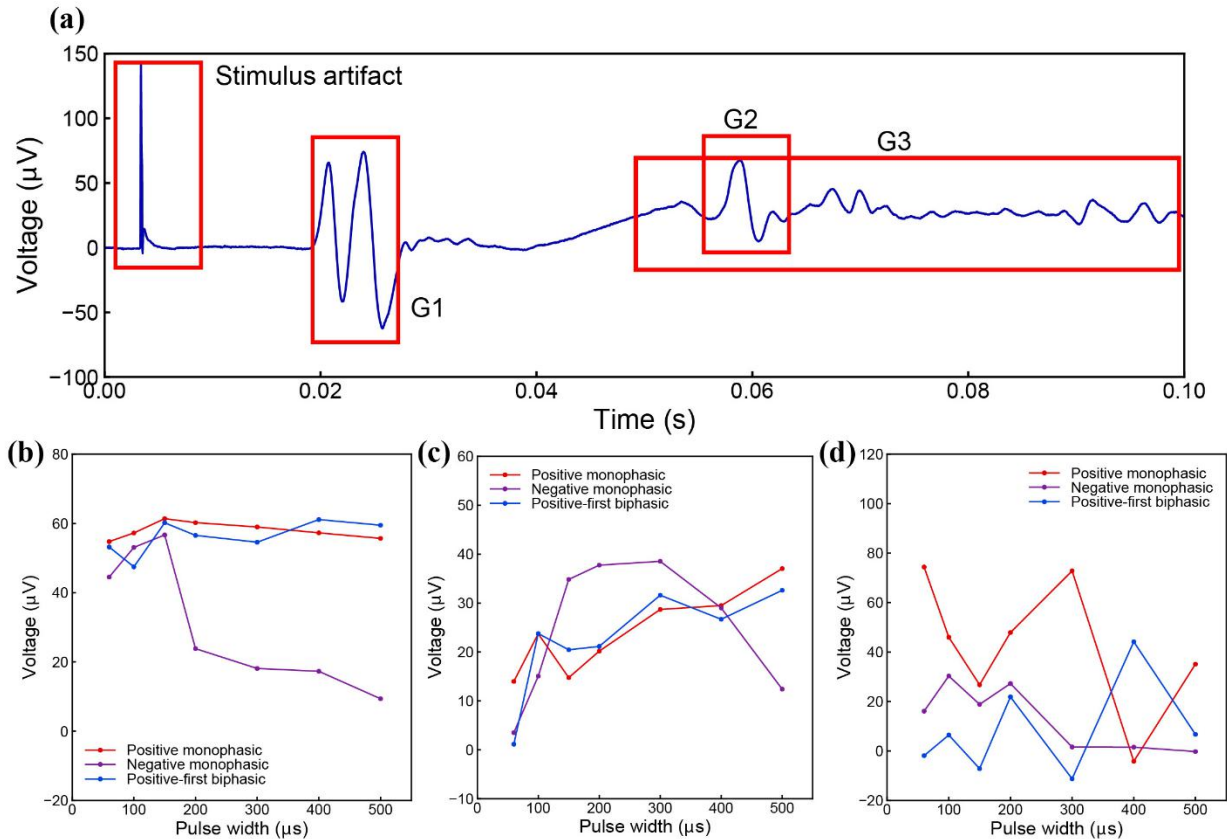


Figure S3.6.1 EMG measurement of the pelvic nerve stimulation by using three different current waveforms. (a) EMG sample of the pelvic nerve stimulation; (b) Amplitude of G1 with three different current waveforms; (c) Amplitude of G2 with three different current waveforms; (d) Amplitude of G3 with three different current waveforms.

The force mapping is a quite reliable method to represent the quantity of action potential because the force is proportional to the motor units recruited by the stimulation. However, this method is not always applicable. For some neural tissues, only ENG (Electroneurography) or EMG measurement is available. But as explained in the previous section, the amplitude of the EMG cannot fully represent the quantity of action potential due to the complex phase combination. The ENG signal will also have the same issue.

However, based on our theory, we still have chance to measure the resonance frequency if the resonance frequency really exists in this neural tissue. Figure S3.5.1(d) shows one successful case on cortical stimulation. As explained in Figure 6, a distinctive curve with clear resonance peak can only be achieved with a proper current amplitude. Meanwhile, as shown in Figure S3.4.2, not every kind of current waveform can show a clear resonance peak. It means the resonance peak can be obtained only with a proper current waveform of a proper amplitude.

Here we used the pelvic nerve as an example to show how to find the resonance frequency from the EMG signal. The detailed experiment setup, procedure and parameter can be found in the **Supplementary S2.3**. Figure S3.6.1(a) shows an EMG signal sample recorded by square wave current stimulation. Normally there will be four groups of signal in the raw data including the stimulus artifact. The real EMG signal can be generally classified as three groups of different time latency, labelled as G1, G2 and G3 as shown in Figure

S3.6.1(a). The different time latency indicates that these three groups of the signal should transmit through different pathways. Three different types of current waveforms, positive monophasic square wave and negative monophasic square wave and positive-first biphasic square wave, with the same amplitude of 70 μA , are used for stimulation. All the detailed EMG data can be found in the **Supplementary S3.6.2**. Here only the amplitude of peak-to-peak voltage of each group is shown from Figure S3.6.1(b) to (d).

For group G1 in Figure S3.6.1(b), all three curves peak at SPPW of 150 μs . For the case of negative monophasic square wave, the curve has a significant drop when the SPPW is higher than 150 μs . This phenomenon cannot be explained by empirical models based on the calculation of charge or energy since more charge and energy induces a lower stimulation. However, in our new theory, this resonance effect is a direct prediction. The peak point at SPPW of 150 μs indicates that the resonance frequency of G1 is around 3333 Hz. The result of G2 also shows a similar situation (Figure S3.6.1(c)). The curve of negative monophasic square wave shows a resonance peak between SPPW of 200 μs and 300 μs , indicating a resonance frequency between 1600 Hz and 2500 Hz. And the result of G3 in Figure S3.6.1(d) shows a random behavior. Considering the long signal duration, this G3 should be movement artifact which is a side effect induced by electrical stimulation. The movement artifacts should have no strong correlation with the SPPW of the input current pulses. It also explains the random behavior of the signal amplitude shown in Figure S3.6.1(d). The different resonance frequencies of G1 and G2 indicate that nerve branches with different circuit parameters are involved in the pelvic nerve stimulation. Even without knowing more detailed circuit parameters, this EMG signal analysis still provide quite a lot of valuable information of the pelvic nerve. But as explained before, such resonance frequency can only be measured with some specific current amplitude and waveform.

S3.6.2. Complete EMG data of pelvic stimulation

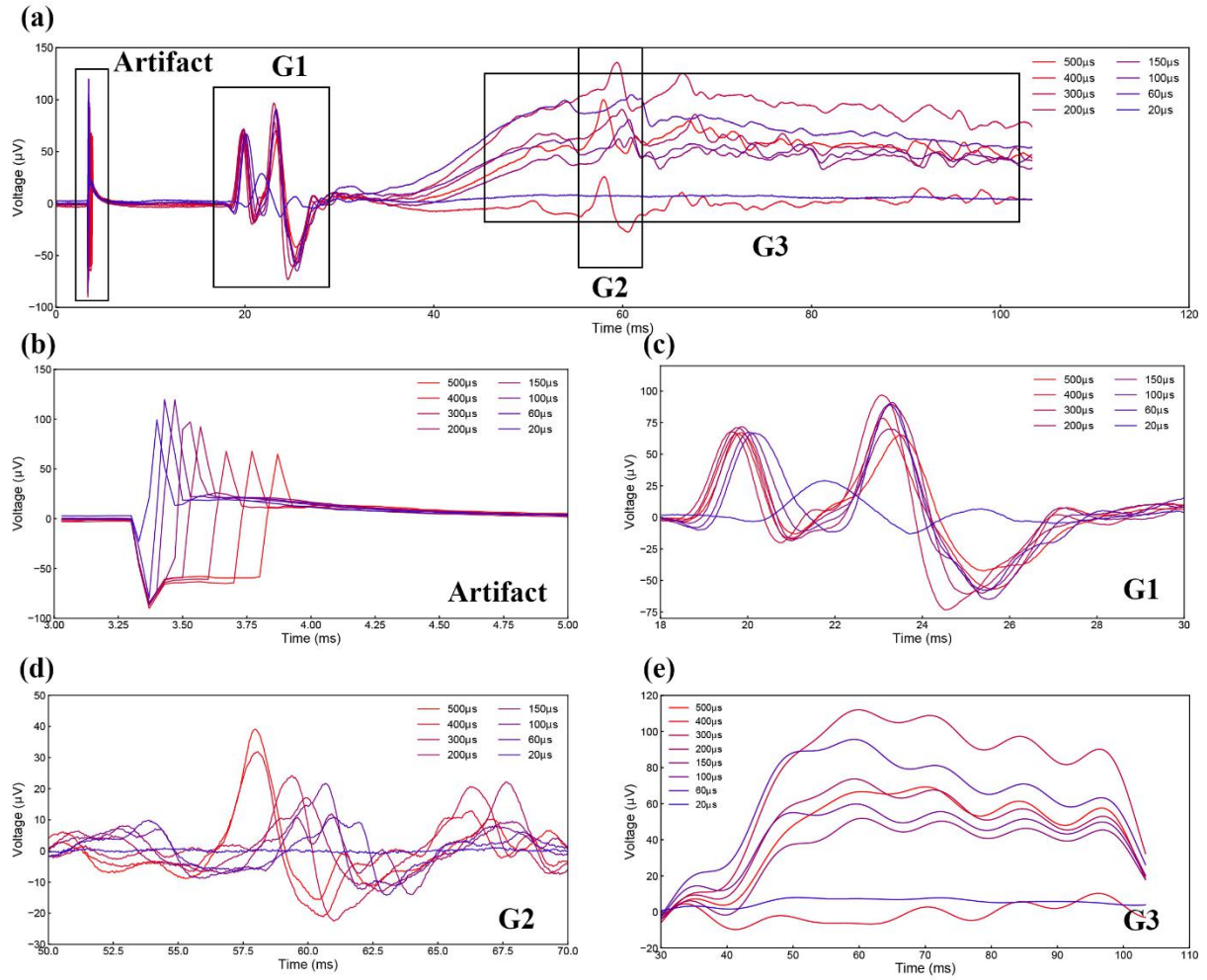


Figure S3.6.2.1 (a) Complete EMG recording result of pelvic nerve stimulation by using positive monophasic square waveform current. The current amplitude is 70 μ A; (b) Stimulus artifact; (c) EMG signal of group G1; (d) EMG signal of group G2 by applying 80 Hz high pass filter; (e) EMG signal of group G3 by applying 80 Hz low pass filter.

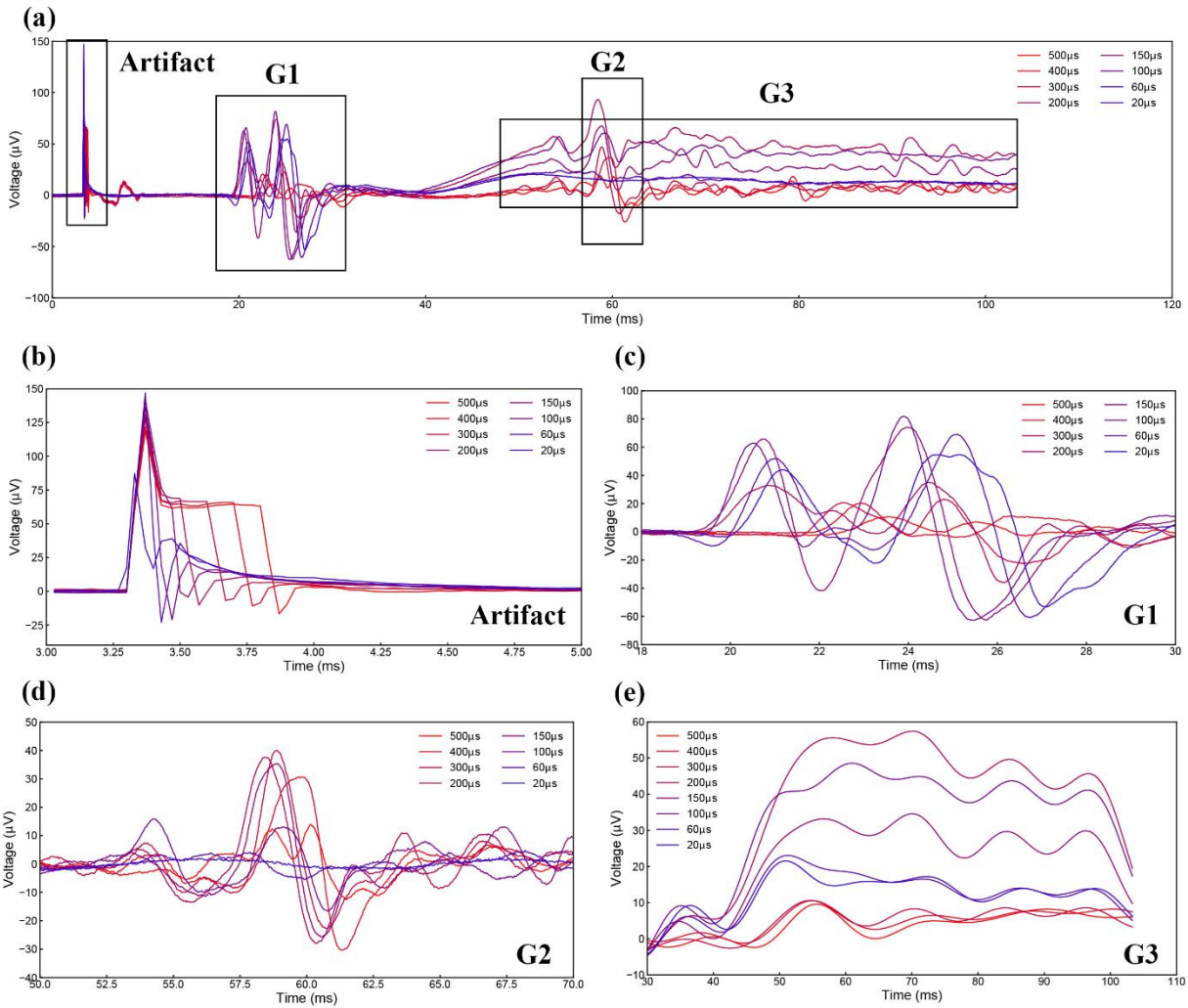


Figure S3.6.2.2 (a) Complete EMG recording result of pelvic nerve stimulation by negative monophasic square waveform current. The Current amplitude is 70 μA ; (b) Stimulus artifact; (c) EMG signal of group G1; (d) EMG signal of group G2 by applying 80 Hz high pass filter; (e) EMG signal of group G3 by applying 80 Hz low pass filter.

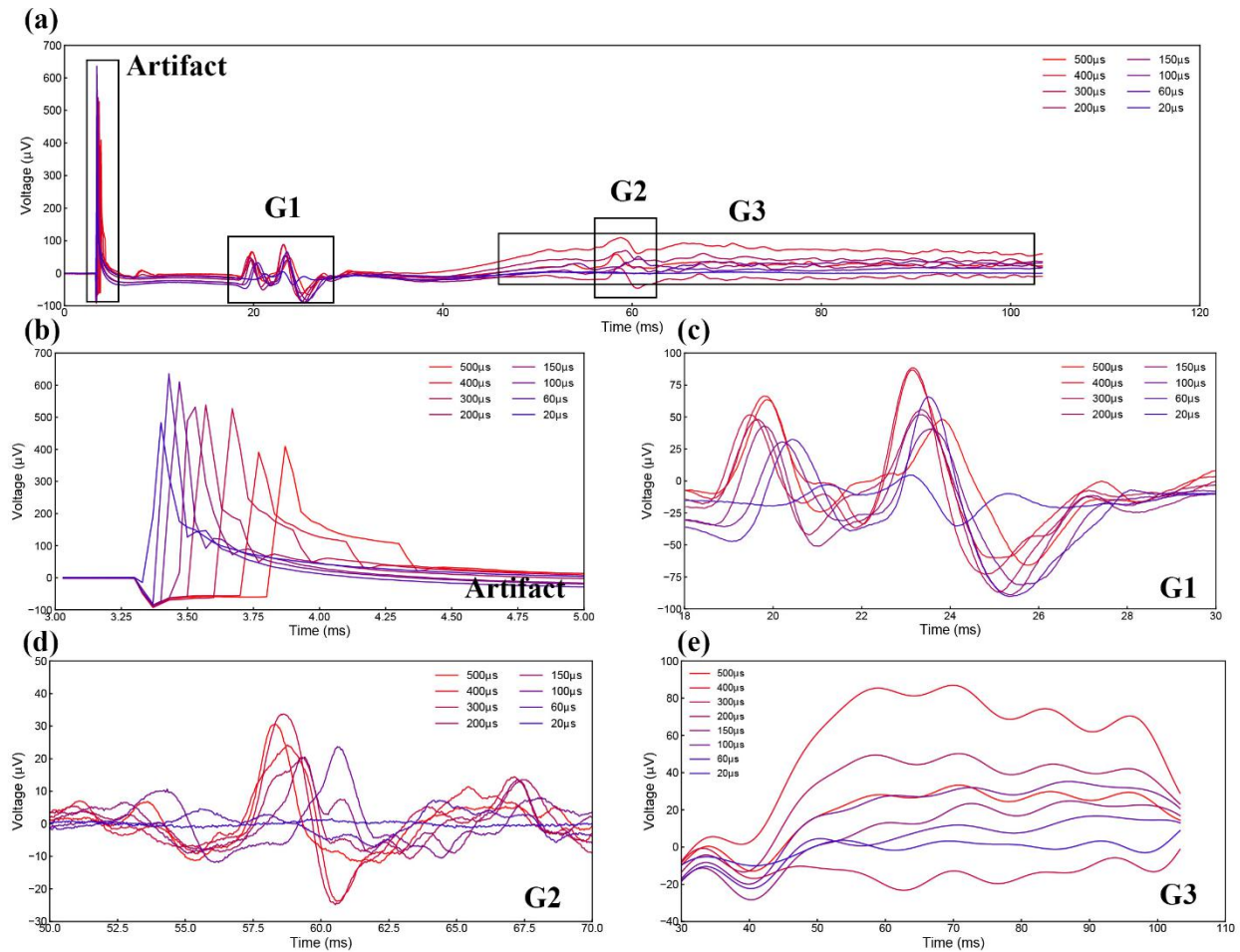


Figure S3.6.2.3 (a) Complete EMG recording result of pelvic nerve stimulation by positive-first biphasic square waveform current. The Current amplitude is 70 μA ; (b) Stimulus artifact; (c) EMG signal of group G1; (d) EMG signal of group G2 by applying 80 Hz high pass filter; (e) EMG signal of group G3 by applying 80 Hz low pass filter.

Figure S3.6.2.1 to Figure S3.6.2.3 show the detailed EMG recording results by applying current with different waveforms. The summary of the peak-to-peak voltage of each EMG group, G1, G2 and G3, is shown in Figure S3.6.1(b)-(d). G2 and G3 are superpositioned with each other. To check the amplitude of these two EMG group independently, a 80 Hz high pass filter and 80 Hz low pass filter are applied for acquiring G2 and G3, respectively. In Figure S3.6.2.2, groups of G1 and G2 show distinctive resonance effect. Instead of the highest SPPW, G1 and G2 achieve maximum peak-to-peak voltage at SPPW of 150 μs and 300 μs , respectively. This phenomenon can be well explained by C-P theory although we did not fit the curve with modeling.

S4 Discussion

S4.1 About exponential distribution

S4.1.1 Exponential distribution for probability calculus

In the reasoning process of the equation for probability calculus, the exponential distribution is a basic hypothesis. It indicates some relationship with quantum mechanics since most of the quantum effects can be described by exponential distribution. Although without any substantial evidences, we still can find some circumstantial evidences in one previous research, which is called Linear-Nonlinear-Poisson (LNP) cascade model, to support this hypothesis.

The LNP cascade model is a simplified functional model of neural spike responses ^[6]. It has been successfully used to describe the response characteristics of neurons in early sensory pathways, especially the visual system. The LNP model is generally implicit when using reverse correlation or the spike-triggered average to characterize neural responses with white-noise stimuli. The number of action potential generated can be described by the Poisson distribution in LNP model.

Actually the Poisson distribution and exponential distribution describe the same stochastic process. If the Poisson distribution provides an appropriate description of the number of the occurrences per interval of time, then the exponential distribution will provide a description of the time interval between occurrences.

The Poisson distribution is as follow:

$$P(x = k; \lambda) = \frac{\lambda^k}{k!} e^{-\lambda}$$

$P(x = k; \lambda)$ is the probability of the k times occurrences of the event in a unit time interval, λ is the expected times of occurrence.

The exponential distribution is as follow:

$$P(t; \lambda) = 1 - e^{-\lambda t}$$

$P(t; \lambda)$ is the probability of the occurrences of the event with the time interval t , $\frac{1}{\lambda}$ is the expected time interval.

These two distributions share the same λ . Apparently, in the C-P theory, if the generation of action potential can be described by exponential distribution, it surely can be described by Poisson distribution.

Here we will give an example showing how we derive the LNP model from the C-P theory. Meanwhile, it will be very intuitive to see how the linear-to-nonlinear process, which is involved in the LNP model, happen and how the C-P theory is compatible with the LNP model.

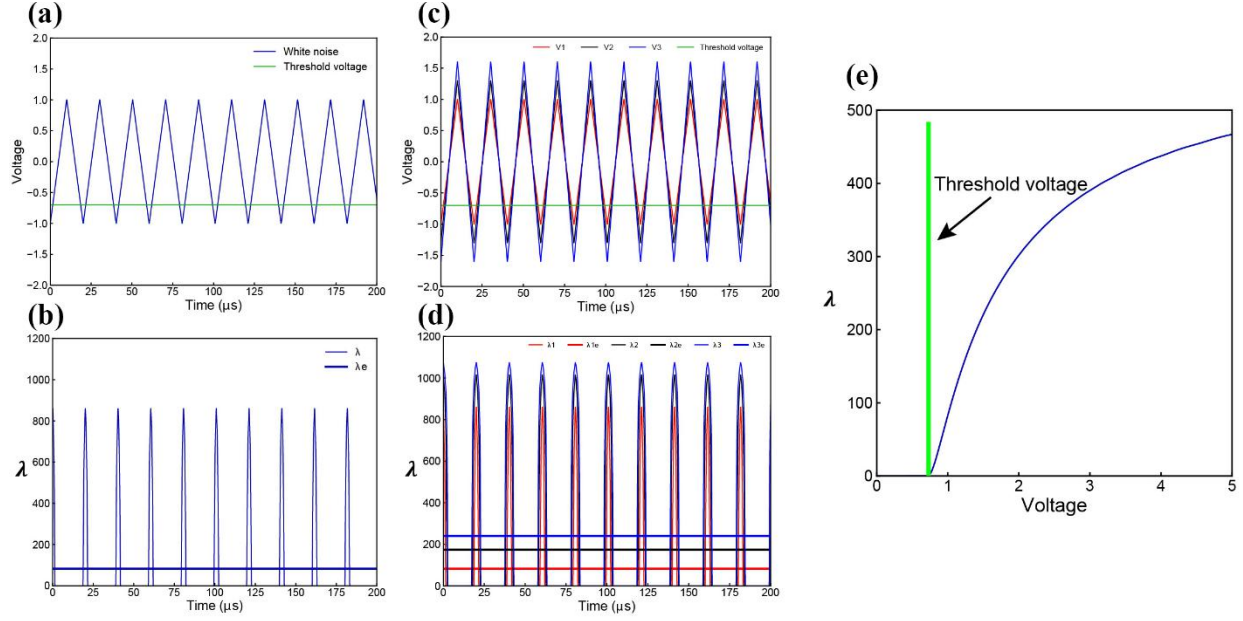


Figure S4.1 Derivation of LNP model from C-P theory. (a) A simplified white noise voltage waveform; (b) The corresponding λ curve of the voltage waveform in (a), this λ curve can be averaged to a λ_e curve; (c) Noise with increasing amplitude; (d) The corresponding λ and λ_e curves of the noise waveforms in (c); (e) The nonlinear curve of λ_e versus the noise amplitude V_w .

The white noise involved in LNP model can be simplified as a triangle wave series of frequency f and amplitude V_w as shown in Figure S4.1(a). Here the shape of the white noise waveform will not affect the derivation process. Any kind of periodical voltage waveform can be used. The triangle wave is used as an example of simple waveform.

Only part of the voltage can exceed the $V_{Threshold}$. As explained in Figure 4(e), the voltage curve can be converted to a λ curve as shown in Figure S4.1(b). The area S_λ of the λ curve within a period $T = 1/f$ can be calculated. Since the λ implemented in the C-P theory is not a constant value while λ in Poisson distribution can only be a constant value, an equivalent λ_e for Poisson distribution can be calculated based on the S_λ :

$$\lambda_e = \frac{S_\lambda}{T} = S_\lambda \times f$$

which is the blue straight line in Figure S4.1(b). Apparently, the λ curve and the λ_e curve are of the same area, so they will induce the same statistical results.

So the probability calculus equation can be rewritten as:

$$P = 1 - e^{-S_\lambda} = 1 - e^{-\lambda_e t}$$

The corresponding Poisson distribution is:

$$P(x = k; \lambda_e) = \frac{\lambda_e^k}{k!} e^{-\lambda_e}$$

By increasing the noise amplitude V_w , S_λ will also increase, result in an increasing λ_e as shown in Figure S4.1(c) and (d). Since S_λ is a function of V_w , and λ_e is a function of S_λ , λ_e is also a function of V_w as shown in Figure S4.1(e). Because the expression of S_λ is a piecewise function of V_w , the exact function

$\lambda_e(V_w)$ can only be calculated numerically with a fixed $\alpha, \beta, V_{Threshold}$ and f . The analytical expression of $\lambda_e(V_w)$ is not available.

Meanwhile, this λ_e versus V_w curve is a non-linear curve, which explains how a linear increment of V_w induces a non-linear increment of λ_e happened in LNP model.

Thus, LNP model can be directly derived from C-P theory and the non-linear effect is an intrinsic property rather than an additional hypothesis in this theory.

S4.1.2 Equation for probability calculus

As explained in the theoretical part, the function of λ is based on three empirical hypotheses. The general form of the function of λ is

$$\lambda = \alpha \times \frac{1}{\frac{\beta}{e^{(|V-V_{Threshold}|)^n} - c}}$$

In this study, we directly set $n = 1$ and $c = 0$ to make the equation simpler. However, when $n \neq 1$ and $0 \leq c \leq 1$, other sets of parameters could still be captured to fit the force mapping curves. Although we derive the expression of λ from three empirical considerations, the exact expression of λ is only determined by its physical meaning. Before knowing the real physical meaning, which is out of the scope of this study, we are not able to determine the exact form of the function of λ . But we still have a conjecture which may help us find the correct form of the function of λ .

In the previous discussion section about LNP model, it is proved that the exponential distribution can be rewritten as Poisson distribution with the same λ . In Poisson distribution, there is a very clear physical meaning of the λ , which is the number of occurrences per interval of time. So the λ can be considered as some kind of frequency, representing some sort of energy density. Since the implementation of the exponential distribution is from the hypothesis of quantum effect as explained in the theoretical part, we may also get some clues from quantum mechanics. The physical meaning of the λ in Poisson distribution can let us associate with the Planck's law, which is given by

$$B_\nu(\nu, T) = \frac{2h\nu^3}{c^2} \frac{1}{e^{\frac{h\nu}{k_B T}} - 1}$$

Where ν is the frequency in the spectrum, T is the absolute temperature, k_B is the Boltzmann constant, h is the Planck constant, c is the speed of light in the medium and $B_\nu(\nu, T)$ is the spectral radiance of a body. Here B_ν can also be considered as a kind of energy density, which is the same as the λ . Meanwhile, B_ν is of the same form of λ when $n = 1$ and $c = 1$, as shown below:

$$\begin{aligned} \alpha &= \frac{2h\nu^3}{c^2} \\ \beta &= \frac{h\nu}{k_B} \\ B_\nu(\nu, T) &= \frac{2h\nu^3}{c^2} \frac{1}{e^{\frac{h\nu}{k_B T}} - 1} = \alpha \times \frac{1}{\frac{\beta}{e^T} - 1} \\ \lambda &= \alpha \times \frac{1}{\frac{\beta}{e^{|V-V_{Threshold}|}} - 1} = \alpha \times \frac{1}{\frac{\beta}{e^{\Delta V}} - 1} \end{aligned}$$

The resemblance between the Planck's law and the function of λ may not be just a coincidence. It may reveal a deeper connection between the ion channel gating and quantum mechanics. In other words, the ion channel gating is induced by electron transition. In optogenetics, it is well known that photon can open the ion channel. One possible physical explanation is photoelectric effect. It is highly possible that electrical nerve stimulation, and even the propagation of neural signals, follows the similar mechanism.

The function of λ with the same form of Planck's law can be called as Plank form λ . The function of λ used in the modeling of this study, in which $n = 1$ and $c = 0$, can be called as the C-P form λ . Currently we

have no substantial evidence to confirm which form is correct. The difference between these two forms are not very distinctive in modeling results. To simplify the parameter capturing, we still use the C-P form λ in the modeling of this study. In the future, we may be able to prove this conjecture with a more detailed study of the ion channel.

S4.2 Inductor in neural tissue

The inductor involved in the C-P theory may be the most controversial part. Not only in this C-P theory but also in some other studies, the similar inductance effect of the neurons has been reported ^[7-8]. The myelinated neurons have much higher inductance than the unmyelinated neurons ^[8]. Nevertheless, in all previous neural models such as H-H model and the cable model, there is no such an inductor involved. Thus, the inductor may seem to be an unnecessary hypothesis for previous neural models.

However, in the C-P theory, the inductor is an inevitable component to make the whole theory established. C-P theory is a basic physical description instead of merely a computational model, and the existence of the inductor has already been confirmed in our testing results. Thus, the physical form of this inductor is a critical issue. Although there is no decisive evidence, quite a lot of clues imply that the myelin should be the component to provide the inductance in the neural tissue.

Firstly, the myelin wrapped around the nerve like a coil, which is a common and effective structure to generate inductance. Then the cell membrane and the myelin can form a RLC circuit and the whole axon can be considered a RLC cascade. However, in the cable theory, the myelin is just modeled as a resistor and the whole axon is treated as a RC cascade. As well known, failure to consider the inductance associated with any alternating electric signal passing along a coaxial cable, such as the first RC based undersea cable in human history, will lead to a disaster in practice. Only with a more sophisticated RLC design based on Maxwell's Equations for a coaxial structure, the new undersea cable was laid with great success. It is difficult to believe that as a result of long evolutionary process, the neuron is still working with a design which is already proved to be a failure in human engineering.

Moreover, modelling the myelin as an inductor can explain why magnetic field can also induce nerve stimulation. As been reported ^[9-10], the magnetic field can stimulate the nerve only when the magnetic field lines is along the axon, in other word, is exactly perpendicular to the sectional area of the myelin. It is a common sense that a changing magnetic field across the sectional area of a coil can generate an inductive voltage. This inductive voltage upon the myelin can be further coupled by the cell membrane, which is a capacitor, to induce the action potential.

Thirdly, if the myelin can be modeled as an inductor, the inductance value can be controlled by the profile of the myelin, either the length or the thickness. Let's just consider the length here. The length of the myelin will not only change the inductance of itself, but also affect the length of the Ranvier node, which will further determine the value of the capacitance induced by the cell membrane. A changing length of the myelin will change both the L and C in the RLC circuit, resulting in a frequency modulation. Such distinct myelin profile distribution is already discovered in pyramidal neurons in the neocortex ^[11]. Such phenomenon definitely cannot be explained if the myelin is still modeled as merely a resistor. However, it is quite easy to understand this phenomenon when the myelin is an inductor. Different axons in the brain will have different intrinsic resonance frequency, which is modulated by the myelin sheath, and this is also how the brain is differentiated into groups with different functions.

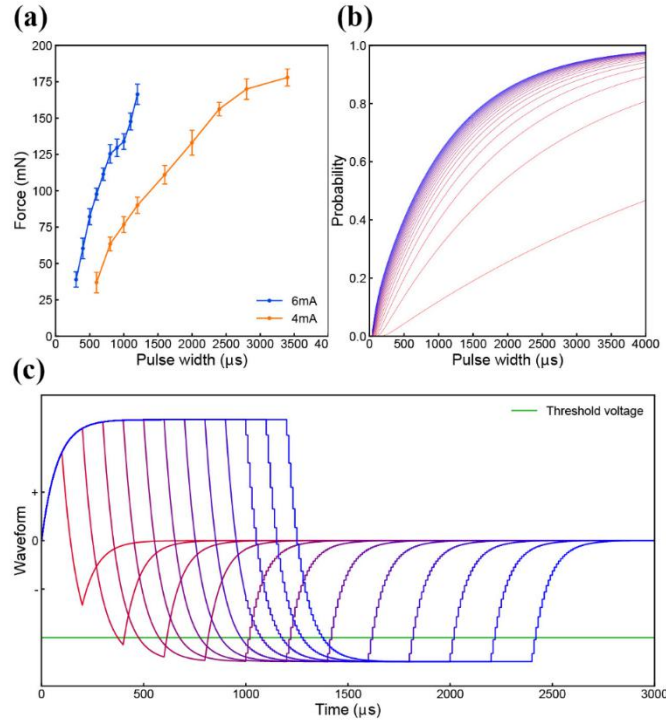


Figure S4.2 Measurement and modeling results of the atrophy TA muscle stimulation by positive-first biphasic square waveform current. (a) Force mapping results; (b) Probability mapping results; (c) Corresponding voltage waveforms.

Finally, as a direct prediction, the unmyelinated nerves should have no inductance or a very low inductance, hence no resonance effect can be detected. To confirm this, we also did a force mapping test on an atrophy muscle, in which the sciatic nerves were transected. Since the muscle fiber is unmyelinated, the force mapping curve should follow the pattern of a RC circuit as shown in Figure S4.2(b). The corresponding voltage waveform is shown in Figure S4.2(c). The two force mapping curves shown in Figure S4.2(a) show monotonically increasing trend as the probability mapping curves in Figure S4.2(b). Since the atrophy muscle is not as healthy as the normal muscle, it cannot stand a long term stimulation to obtain many force mapping curves. But we still consider this RC pattern from atrophy muscle as a circumstantial evidence implying that myelin is an inductor.

S4.3 About the empirical models

S4.3.1 The stimulation efficiency of different current waveforms

In previous empirical models for electrical nerve stimulation, the efficiency of different waveforms is also a key point to be discussed. Some ambiguous conclusions, such as negative pulse will be more effective for stimulation, will be drawn from these empirical models. And there is even an argument about whether exponential wave is the most energy-efficient waveform for nerve stimulation^[12-13]. Two research groups got the opposite conclusion about nerve stimulation by exponential current wave.

Apparently, based on our C-P theory, it is unscientific to say one current waveform is more effective than another. The comparison result of different current waveforms is not only affected by their own waveforms, but also affected by the current amplitude, circuitry parameters and probability calculus parameters. The probability mapping curves with the same current amplitude but different waveform can even have a cross point, which can be seen in both testing and modeling results shown in Figure S3.3.2(a)&(b) and Figure S3.4.2(a)&(b). In the four waveforms comparison measured in three experiments (one is shown in Figure S3.3.2 and another two are shown in the **Supplementary S3.3.3**), the negative-first biphasic is more effective than positive-first biphasic in one test (Figure S3.3.2) and less effective in another two tests (In the **Supplementary S3.3.3**).

In the C-P theory, any situations can happen, such as the cross point of probability mapping curves of different waveforms and the efficiency switch between positive-first biphasic and negative-first biphasic (happen in three times of muscle tests of four waveforms comparison), and can be validated by testing results. Such phenomenon definitely cannot be explained by any previous theories or models that calculate either charge, current, voltage or energy.

Meanwhile, in the C-P theory, it is meaningless to investigate which current waveform is the most effective one for nerve stimulation. Other than the waveform, frequency will be a more important parameter to be considered. Normally the input current with the resonance frequency of the neural tissue will be more effective. And the stimulation result is also affected by the testing condition, such as R_1 , which is affected by the humidity on the nerve surface. However, despite these complex situations, some general conclusions still can still be drawn from the C-P theory. For example, normally biphasic current waveform will be more effective than monophasic waveform because of a larger effective voltage area, and negative monophasic current pulses will be more effective than positive monophasic current pulses.

S4.3.2 Strength–duration relationship

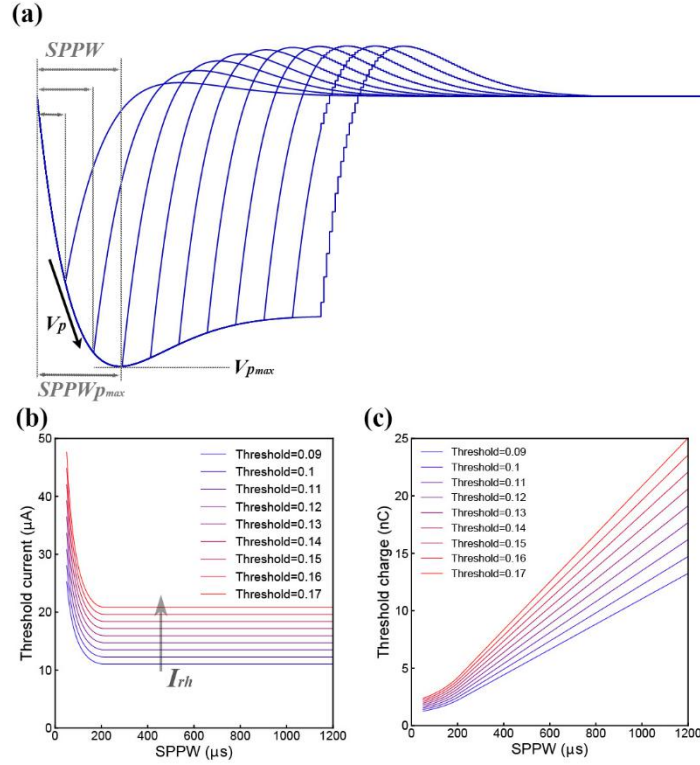


Figure S4.3.2.1 Derivation of the Strength–duration relationship. (a) Illustrative voltage waveforms generated by negative monophasic square waveform current; (b) The threshold current amplitude (I_{th}) decreases as the **SPPW** increases in a nonlinear fashion; (c) The relationship between threshold charge (Q_{th}) and **SPPW** is linear.

It is widely believed that charge is the factor to induce nerve stimulation. In such charge based theory, there is an empirical linear relationship between the threshold charge level and pulse duration, which is called Weiss's strength–duration equation ^[14] for negative monophasic square current pulses. This equation describes the threshold charge as a function of pulse width as follows:

$$Q_{th}(PW) = I_{rh} \times PW + T_{ch} \times I_{rh}$$

where I_{rh} is the rheobase current, T_{ch} is the chronaxie, and PW is the pulse width. The rheobase current is defined as the threshold current for infinitely long pulses. The chronaxie is defined as the pulse duration required for excitation when the current amplitude is equal to twice the rheobase current.

And Lapicque reiterated Weiss's equation for the strength–duration relationship ^[15], but in terms of the threshold current, and introduced the rheobase current and chronaxie as the constants:

$$I_{th}(PW) = I_{rh} \left(1 + \frac{T_{ch}}{PW} \right)$$

Apparently, these two equations are just mathematical description without explaining how I_{rh} happen and why the curve follows a specific trend.

However, in C-P theory, such strength–duration relationship can be directly obtained. Meanwhile, the existence of I_{rh} can be directly derived from C-P theory with a clear physical definition.

Figure S4.3.2.1(a) shows a typical voltage waveform by applying negative monophasic square current with difference SPPW. For the voltage waveform of each SPPW, there will be a peak voltage, denoted as V_P . Since this V_P varies with current amplitude I and pulse width $SPPW$, the V_P can be written as a function as $V_P(I, SPPW)$. Based on C-P theory, when the amplitude of $V_P(I, SPPW)$ reaches the amplitude of $V_{Threshold}$, nerve excitation will be induced. Then both the threshold current I_{th} and the threshold charge, which is $Q_{th} = I_{th} \times SPPW$, are defined as the current and charge required to make the peak voltage, V_P , reaches the threshold voltage, $V_{Threshold}$.

Then the boundary condition is:

$$V_P(I_{th}, SPPW) = V_{Threshold}$$

here are the two equations:

$$I_{th} = f(SPPW, V_{Threshold})$$

$$Q_{th} = g(SPPW, V_{Threshold}) = I_{th} \times SPPW = f(SPPW, V_{Threshold}) \times SPPW$$

Since the function of $V_P(I_{th}, SPPW)$ is too complicated, here only numerical solutions of $I_{th} = f(SPPW, V_{Threshold})$ and $Q_{th} = g(SPPW, V_{Threshold})$, which are calculated with a set of modeling parameter (Table 1-S4.3.2.1) are provided as shown in Figure S4.3.2.1(b) and (c). In Figure S4.3.2.1(b), all curves will decrease to a constant value, which is the I_{rh} in Weiss's strength-duration equation.

And the reason of I_{rh} is also very simple. In Figure S4.3.2.1(a), the V_P will reach a maximum value, denoted as $V_{P_{max}}$, at a certain $SPPW$, denoted as $SPPW_{P_{max}}$. So when $SPPW \geq SPPW_{P_{max}}$, $SPPW$ will not affect V_P and V_P is only a function of I_{th} , rewritten as follow:

$$V_P(I_{th}, SPPW) = V_{P_{max}}(I_{th}) \quad \text{when } SPPW \geq SPPW_{P_{max}}$$

Then the boundary condition is:

$$V_{P_{max}}(I_{th}) = V_{Threshold} \quad \text{when } SPPW \geq SPPW_{P_{max}}$$

Then the target function to be solved for threshold current is rewritten as:

$$I_{th} = f(SPPW, V_{Threshold}) = f(V_{Threshold}) \quad \text{when } SPPW \geq SPPW_{P_{max}}$$

Since $V_{Threshold}$ is a constant value, then I_{th} is also a constant value, which is so called rheobase current I_{rh} , when $SPPW \geq SPPW_{P_{max}}$. This rheobase current I_{rh} is to make $V_{P_{max}}$ reach $V_{Threshold}$. If the current I is lower than I_{rh} , meaning the amplitude of $V_{P_{max}}$ is always lower than the amplitude of $V_{Threshold}$, then no nerve excitation can be induced no matter how large $SPPW$ is. When $I_{th} = I_{rh}$, $V_{P_{max}}$ will always be equal to the $V_{Threshold}$ as long as $SPPW \geq SPPW_{P_{max}}$. That is why the curve in Figure S4.3.2.1(b) will keep a constant value of I_{rh} when $SPPW \gg SPPW_{P_{max}}$.

Meanwhile,

$$Q_{th} = I_{th} \times SPPW = I_{rh} \times SPPW \quad \text{when } SPPW \geq SPPW_{P_{max}}$$

Since I_{rh} is a constant, Q_{th} will be a linear curve with respect to $SPPW$, when $SPPW \geq SPPW_{P_{max}}$, as can be seen in Figure S4.3.2.1(c).

Then in the C-P theory, the physical definition of I_{rh} is very clear. It is the threshold current to make the peak value of the voltage waveform, $V_{P_{max}}$, higher than the threshold voltage $V_{Threshold}$ of nerve stimulation. Meanwhile, in the C-P theory, the nonlinear curve of I_{th} versus $SPPW$, existence of I_{rh} and linear curve of Q_{th} versus $SPPW$, can be directly obtained without any extra hypotheses.

The curves in Figure S4.3.2.1(b) and (c) are exactly the curves which are well known as the strength–duration relationship. In the C-P theory, such relationship is an intrinsic property with only numerical solution. The exact analytical equation for this relationship is not available.

Meanwhile, there are two major differences between the strength–duration relationship derived from Weiss's equation and C-P theory. Firstly, rather than infinitely approaching to the I_{rh} as the case in Weiss's strength–duration equation, the threshold current curve will be equal to the I_{rh} when $SPPW \geq SPPW_{p_{max}}$. Secondly, rather than being a completely straight line, the threshold charge curve is linear only when $SPPW$ is large. When the $SPPW$ is approaching zero, the slope of threshold charge curve will also approach zero, meaning that the threshold charge will converge in a constant value at low $SPPW$. These two major special differences with the Weiss's equation have already been confirmed by previous research^[16-17] and now can be well explained in the C-P theory.

Moreover, such relationship between the threshold current and pulse width differs with the current waveforms. For other waveforms such as positive monophasic, positive-first biphasic and negative-first biphasic, the strength–duration relationship may show a more complicated trend without a stable I_{rh} . It is also observed that other types of current waveform can generate different strength–duration curves^[17].

In Figure S.4.3.2.2, representative strength–duration curves of other waveforms including different types of square waves and sine waves are shown. But these curves actually also vary with different circuit parameters. It also explains why only negative monophasic square wave can achieve such a stable strength–duration relationship.

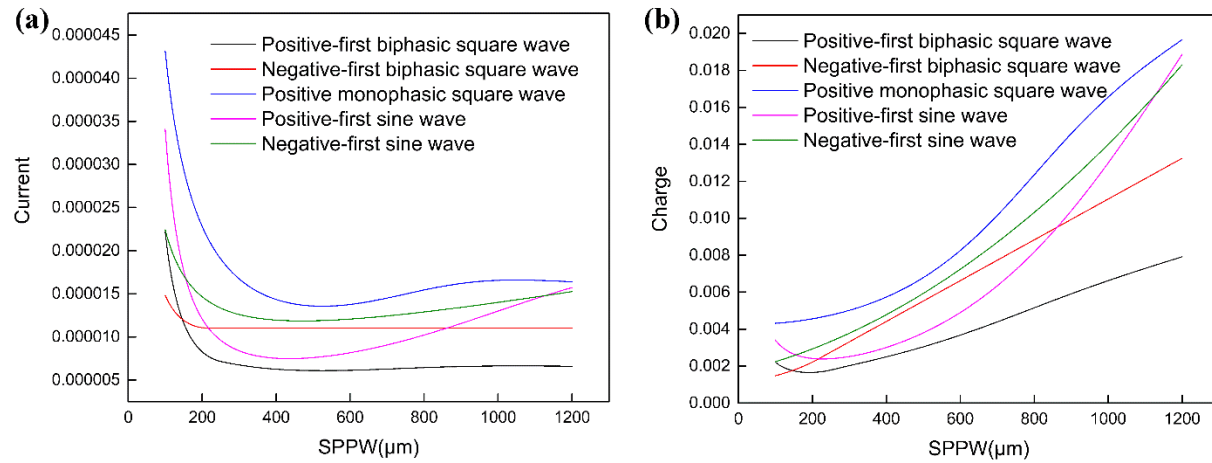


Figure S.4.3.2.2 (a) The relationship between the threshold current amplitude (I_{th}) and the $SPPW$ for different current waveforms; (b) The relationship between threshold charge (Q_{th}) and $SPPW$ for different current waveforms.

The Strength–duration relationship of different current waveforms are shown in Figure S.4.3.2.2. Only the negative-first biphasic square waveform shows a stable I_{rh} , which is the same pattern as the one in Figure S.4.3.2.1. All other type of current waveforms don't have stable I_{rh} , and their charge curves (Figure S.4.3.2.2(b)) are non-linear. For the curve of sinewave current, the threshold current curve increases at high $SPPW$ range, this phenomenon has been observed in previous research with triangle current waveform^[18]. Considering that triangle waveform is quite similar as the sinewave, this is why they share the similar pattern of strength–duration relationship.

S4.4 The polarity of the voltage upon the capacitor

In this C-P theory, the voltage waveform upon the capacitor is the most critical factor affecting the stimulation results. The negative voltage, which should be the potential outside of the membrane versus the potential inside the membrane, is effective for stimulation since the sodium ion channel is gated by negative voltage. However, in the lumped parameter circuit used in this study, we are not able to define which terminal refers to either the outside part or inside part of the membrane. This is because this is a simplified circuit, the physical meaning of each terminal of the capacitor, which can be defined in a complete distributed parameter circuit, disappears. All capacitors referring to each membrane segment are simplified as one capacitor. So here we have to manually introduce a method to determine which terminal of the capacitor should be defined as positive. Currently, in all the stimulation tests, the downstream electrode, which is more close to the recording side, was defined as positive. The voltage in the modeling adopted the same polarity as the current waveform from the downstream electrode. For example, if the downstream electrode is connected with the positive terminal of the stimulator and the current is the positive first biphasic square waveform, the corresponding voltage waveform upon the capacitor also has a positive first phase. The validity of this method is proved in all modeling results.

S4.5 About the sine waveform tests

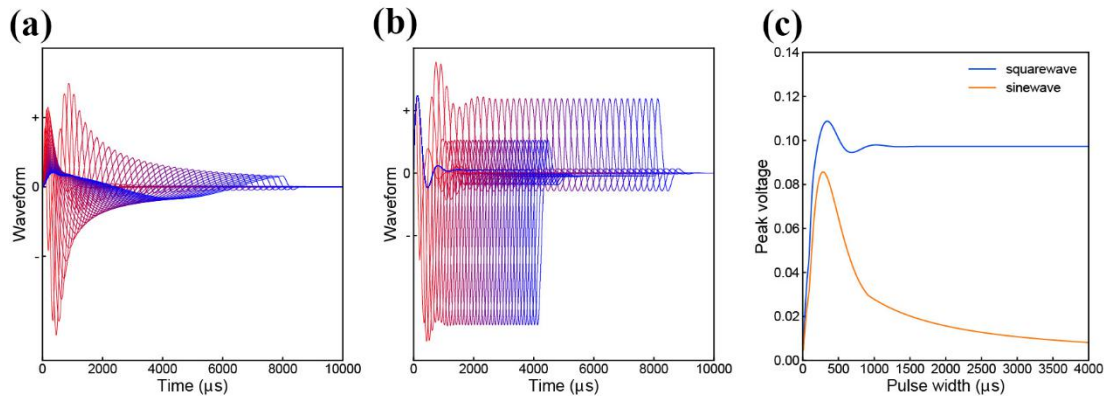


Figure S4.5 Waveform comparison of sinewave and square wave current. (a) An illustrative sinewave current with different SPPW; (b) An illustrative positive-first square waveform current with different SPPW; (c) Peak value comparison of the voltage waveform of sinewave and positive-first square wave with different SPPW.

Because of the parallel RLC circuit, theoretically sine wave should be the best waveform to capture the resonance frequency of a neural tissue. However, in actual test, the sinewave test was only successful on the CP nerve. In both muscle and cortical test, the sinewave can easily damage the tissue by only a few stimulation trials. Afterwards, no neural response can be further detected no matter what current waveform was applied.

One possible reason for this phenomenon is that the voltage response of the sinewave is with a too high Q factor while the voltage response of the square wave has a very low Q factor. An illustrative voltage waveform by sinewave and positive-first square wave current is as shown in Figure S4.5(a) and (b). And the Figure S4.5(c) shows how the peak value of the voltage waveform changes with SPPW. For the square waveform, the peak value will keep almost constant at high SPPW while the peak value of sinewave can drop to a very low value. So the voltage difference of square wave at different SPPW will not change a lot, meaning a low Q. Therefore, a gradual change of the force generated by different SPPW can be well recorded. However, the situation of sinewave is quite different. If a proper current amplitude at a very high or a very low SPPW is selected to generate a medium level force, the amplitude of the voltage waveform will increase significantly when the SPPW is tuned to be close to the resonance frequency, and then exceeds the threshold voltage to induce tissue damage. This phenomenon repeatedly happened in the sinewave test. Initially some data points can be recorded but suddenly from one data point, no further stimulation, either the force or the EMG signal, can be detected. Even if the current waveform was switched back to square waveform, there was still no response at any current amplitude. Apparently the neuron has been damaged. This result also indicate that sinewave may be very dangerous for stimulation of skeletal muscle and cortex.

S5 A thought experiment

To help readers comprehend the C-P theory, a thought experiment is proposed. Three basic questions are asked and each question has an exclusive answer. The C-P theory is the direct reasoning result of this experiment.

To facilitate understanding of the C-P theory, several key points are emphasized. Firstly, this thought experiment is not based on any previous theories or models, such as H-H model, cable theory and other empirical models. Secondly, the answers of these three questions are based on pure logic and some basic physical knowledge. Not much biological knowledge is involved. Thus, as a reasoning result of this thought experiment, the C-P theory is a physical theory other than a biological theory. As a physical theory, it is a priori rather than a posteriori which is the case for most of the previous biological theories and models. Thirdly, we derived the C-P theory from this thought experiment because we believe that the answer for each question is exclusive. Only when alternative answers exist, the correctness of this priori theory can be jeopardized.

The thought experiment is as follows:

For the electrical nerve stimulation, an electric input is applied and action potentials can be generated. This action potential is not the direct conduction of the electric input. It is the response of the ion channel to electric input.

Q1: What is the real factor inducing the ion channel gating?

We know that the ion channel response is induced by the electric input. However, an electric input can generate changes in many different physical quantities such as current, voltage, charge, energy and electric field. In the H-H model, electric field and voltage is used to interpret the ion channel response. In other empirical models, people also try developing the relationship between the ion channel response and current, voltage, charge and energy. To find out the real factor to induce the ion channel, let's imagine two situations.

Firstly, imagine a nerve connected with a pair of electrodes. When we apply a current pulse, how will the current flow through the nerve? Some current will just flow through the outer surface of the nerve, some will flow through the tissue and some will flow through the ion channel. Apparently, not all the current can truly interact with the ion channel. If there is some liquid, such as blood, on the outer surface of the nerve, most of the current will just flow through the liquid instead of flowing through the tissue due to the short circuit between two electrodes induced by liquid. Thus the current truly interacting with ion channels only takes a small ratio of the injected current and this ratio can be significantly affected by external environment. The situation is the same with voltage, charge and energy. Although we still can summarize some vague relationship between the stimulation result and electric input, such as the strength-duration relationship, a precise and accurate mathematical relation between the stimulation result and electric input from the stimulating electrode is unavailable.

Secondly, imagine an individual ion channel embedded upon the cell membrane and surrounded by different molecules and all kinds of ions. In such a microscopic world, all interactions are actually induced by field. Normally the cell membrane can be considered as a capacitor, which means no ion can directly go through the membrane unless the ion channel is open. So all the positive and negative ions are now accumulated at the inside and outside surfaces of the cell membrane. However, since all these ions have no physical contact with the ion channel, the ion channel can only sense the electric field emitted by all these ions. So apparently, electric field is the key factor to interact with the ion channel.

Q2: How to obtain this electric field?

Before answering this question, we need to think of another question first: **What kind of features should this electric field have?**

As well known, the cell membrane is impermeable to ions. All the ions are accumulated at both sides of the cell membrane. So the direction of major component of the electric field emitted by these ions should be perpendicular to the cell membrane surface, in other words, along the longitudinal dimension of the ion channel. Meanwhile, the strength of the electric field is proportional to the quantity of the ions. Since ions can only move with a certain speed, the accumulation of ions induced by external applied electric input requires a certain duration. This is also why a capacitor requires some time to get charged and discharged. It means no matter what kind of electric input is applied, for example, a certain current, a certain voltage or a certain quantity of charge, the electric field is always a time-varying field with gradual change. We need to know how this electric field changes with time. In summary, the two key features of the electric field, direction and how it change with time, are inevitable.

Now we can consider how to obtain this electric field.

One easy answer is that we can get the electric field distribution within a tissue by finite element modeling. In this method, the tissue can be simplified as a kind of medium with a set of parameters such as conductivity, permittivity and permeability. In fact, many research groups have adopted this method for decades. However, in this method, the direction of the electric field is only determined by the position of the electrodes, the boundary conditions and the medium parameters, but not the orientation of the cell membrane and the ion channels. Moreover, the information of how the electric field and the tissue condition changes with time is also lost, because the electric field distribution obtained from the modeling only reveals how the electric field spread from the electrodes, not how the ions moves within the tissue. The localized electric field around the ion channel is mainly determined by the movement of ions on both sides of the cell membrane. But the movement of ions is not only determined by the external applied electric field, but also constrained by the physical boundary of the cell membrane, the conditional permeability of ion channels and channel refractory periods. Electric field modeling can tell us how the electric field emitted from the electrode spreads in the tissue, but never tell us how this electric field drives the ions. In summary, the electric field obtained from previous modeling method does not meet the requirement mentioned above: with a correct direction and provide the information of how the electric field changes with time.

Let's think about the direction issue first. As explained, the electric field we need is perpendicular to the cell membrane. If we model the cell membrane as a capacitor, based on the ion quantity upon the surface of the cell membrane, we can directly calculate the voltage with the equation $V = Q/C$, where Q is the charge quantity and C is the equivalent capacitance. Meanwhile, the electric field across the capacitor can be calculated as $E = V/d$, where d is the thickness of the cell membrane. It should be noted that the electric field calculated here is perpendicular to the cell membrane, which is exactly what we desire. It means that if we model the cell membrane as a capacitor, then the voltage calculated upon this capacitor will be proportional to the magnitude of the electric field we need and with the correct direction. Although the voltage V is a scalar, we still can use it to characterize the electric field we need, which is a vector, because the information of the direction has already been included.

Then let's think about the time issue. Since the cell membrane is now modelled as a capacitor, we need to know how the voltage changes with time, in other words, the voltage waveform induced by an electric input. Apparently, this voltage waveform upon the capacitor is not only determined by the capacitor itself, but also by the peripheral circuit and the waveform of the electric input. Here we can take the parallel RC circuit as a simple case. The charging and discharging rate of the capacitor is determined by the time constant $\tau = RC$. The resistor R connected in parallel with the capacitor C can also change the charging and discharging rate then affect the voltage waveform. On the other hand, the voltage waveforms generated by a square wave current pulse and a sine wave current pulse are definitely different. It also can be expected that voltage waveform difference, induced by either different peripheral circuits or different current waveforms, should result in different nerve stimulation results. In summary, to obtain the exact voltage waveform, we need to construct a complete circuit which is equivalent to the neural tissue, including the cell membrane and all

other peripheral circuit components. Meanwhile, we need to specify the detailed waveform of the electric input.

In summary, we need to know the correct equivalent circuit. With this correct circuit, the correct voltage waveform upon the cell membrane can be calculated from the electric input.

Up to now, we know the circuit is important. Let's pretend that we already know the exact circuit equivalent to a specific neural tissue. Then a current pulse is applied and an exact voltage waveform is generated upon the cell membrane.

Q3: How an exact voltage waveform determines the gating state of a specific ion channel?

Firstly, let's imagine an individual ion channel. If no voltage is applied, no action potential will be generated no matter how long time it takes. It means a 0V voltage cannot introduce any effect upon the ion channel. If a negative voltage with a certain amplitude and duration is applied, definitely action potential can be generated. So an obvious conclusion can be drawn here: the threshold voltage exists. At least, the voltage required to induce an action potential should exceed 0V.

Then let's pretend that we already know the threshold voltage, denoted as V_T . Now we can guess how the ion channel is affected by the voltage.

One simple guess is that the ion channel is open when the voltage, V , exceeds V_T . It means at the time point, t_T , when the $V \geq V_T$, the ion channel will open and an action potential will be generated. (Notice that voltage V is a negative value) Then we can measure this V_T . No matter what kind of voltage waveform is applied, such as a sine wave or a square wave, the action potential is always generated at the time point t_T when $V \geq V_T$. However, all the previous researches show that the working mechanism of ion channel is not so simple.

Then another guess is that V should be kept for some duration, denoted as T , after exceeding V_T to open the ion channel. Then we can apply a DC voltage V_{DC} upon the ion channel and measure this T . When $V_{DC} < V_T$, no action potential can be generated. When $V_{DC} \geq V_T$, after a duration T , action potential can be generated. If we kept V_{DC} as the same value, a constant T can be measured. This T may be a function of V_{DC} ($T = f(V_{DC})$). A higher V_{DC} can induce a shorter T . However, this DC voltage test has already been done before and the results show that ion channel does not work like this. Such a function $T = f(V_{DC})$ cannot be achieved.

We know there is a threshold voltage. We also know ion channel does not open at the time point when $V \geq V_T$. So what happens in this duration T . It looks like that something is accumulated within this T to open the ion channel. And the result of ion channel opening is discrete. It suddenly switched from close state to open state. Although the state change of an individual ion channel is discrete, the number of excited nerve fibers in a nerve branch can have a continuous change by changing either the current amplitude or the pulse duration. There definitely is something that can build the bridge between the microscopic discrete and macroscopic continuity.

To solve the issue above, let's treat the ion channel as a black box first and see whether we can find some clues. From the above discussion, we find that even we give the same input each time, the output from this black box is different. Is the thing hidden in the black box deterministic? If it is, then the same input should result in the same output. If the output is different, it means the input is definitely different. Surely we are not able to control everything identical in reality. There is always something not identical for each test. But as long as the system is deterministic, we can always know the system better with a more precisely controlled experiment condition. Unfortunately, previous researches don't show such an optimistic perspective. So what if the thing hidden in the black box is not deterministic? What if the ion channel is probabilistic? Just like the situation happened in quantum mechanism, everything about elementary

particles is discrete and can only be described by probability, but everything built by these elementary particles in macroscopic is still continuous.

So if the ion channel is non deterministic, probability is the exclusive option to describe its working mechanism. Then the above question can also be answered: within the duration T , the thing getting accumulated is probability.

Probability is the exclusive option to describe the gating of the ion channel.

Up to here, we get a basic framework, which is called C-P (Circuit-Probability), for the analysis of electrical nerve stimulation.

References

- [1] Lee, S. et al. Toward Bioelectronic Medicine-Neuromodulation of Small Peripheral Nerves Using Flexible Neural Clip. *Adv Sci (Weinh)* 4, 1700149, doi:10.1002/advs.201700149 (2017).
- [2] Kang, X. Y. et al. Fabrication and electrochemical comparison of SIROF, AIROF EIROF microelectrodes for neural interfaces. *IEEE Eng Med Biol Soc*, 478-481 (2014).
- [3] Meyer, R. D., Cogan, S. F., Nguyen, T. H. & Rauh, R. D. Electrodeposited iridium oxide for neural stimulation and recording electrodes. *IEEE T Neur Sys Reh* 9, 2-11 (2001).
- [4] Slavcheva, E., Vitushinsky, R., Mokwa, W. & Schnakenberg, U. Sputtered Iridium Oxide Films as Charge Injection Material for Functional Electrostimulation. *Journal of The Electrochemical Society* 151, E226, doi:10.1149/1.1747881 (2004).
- [5] Popovic, D., Baker, L.L. and Loeb, G.E., 2007. Recruitment and comfort of BION implanted electrical stimulation: implications for FES applications. *IEEE Transactions on neural systems and rehabilitation engineering*, 15(4), pp.577-586.
- [9] Schwartz O., Pillow J. W., Rust N. C., & Simoncelli E. P. (2006). Spike-triggered neural characterization. *Journal of Vision* 6:484–507
- [7] HEARING: A 21ST CENTURY PARADIGM, ISBN 978-1-4251-6065-4
- [8] Cole, K.S. and Baker, R.F., 1941. Longitudinal impedance of the squid giant axon. *The Journal of general physiology*, 24(6), pp.771-788.
- [9] Maccabee, P.J., Amassian, V.E., Eberle, L.P. and Cracco, R.Q., 1993. Magnetic coil stimulation of straight and bent amphibian and mammalian peripheral nerve in vitro: locus of excitation. *The Journal of Physiology*, 460(1), pp.201-219.
- [10] Basser, P.J. and Roth, B.J., 1991. Stimulation of a myelinated nerve axon by electromagnetic induction. *Medical and Biological Engineering and Computing*, 29(3), pp.261-268.
- [11] Tomassy, G.S., Berger, D.R., Chen, H.H., Kasthuri, N., Hayworth, K.J., Vercelli, A., Seung, H.S., Lichtman, J.W. and Arlotta, P., 2014. Distinct profiles of myelin distribution along single axons of pyramidal neurons in the neocortex. *Science*, 344(6181), pp.319-324.
- [12] Jezernik, S. and Morari, M., 2005. Energy-optimal electrical excitation of nerve fibers. *IEEE Transactions on Biomedical Engineering*, 52(4), pp.740-743.
- [13] Wongsarnpigoon, A., Woock, J.P. and Grill, W.M., 2010. Efficiency analysis of waveform shape for electrical excitation of nerve fibers. *IEEE Transactions on Neural Systems and Rehabilitation Engineering*, 18(3), pp.319-328.
- [14] Weiss, G., 1990. Sur la possibilite de rendre comparables entre eux les appareils servant a l'excitation electrique. *Archives Italiennes de Biologie*, 35(1), pp.413-445.
- [15] Lapique, L., 1909. Definition experimentale de l'excitabilite. *Soc Biol.*, 77, pp.280-283.
- [16] Su, X., Simenson, H.A., Dinsmoor, D.A. and Orser, H.D., 2017. Evaluation of Pulse-Width of Spinal Nerve Stimulation in a Rat Model of Bladder Micturition Reflex. *Neuromodulation: Technology at the Neural Interface*, 20(8), pp.793-798.
- [17] Rodríguez-Fernández, Á.L., Rebollo-Roldán, J., Jiménez-Rejano, J.J. and Güeita-Rodríguez, J., 2016. Strength-duration curves of the common fibular nerve show hypoexcitability in people with functional ankle instability. *PM&R*, 8(6), pp.536-544.

[18] Rodríguez-Fernández, Á.L., Rebollo-Roldán, J., Jiménez-Rejano, J.J. and Güeita-Rodríguez, J., 2016. Strength-duration curves of the common fibular nerve show hypoexcitability in people with functional ankle instability. *PM&R*, 8(6), pp.536-544.